Massachusetts Institute of Technology
Woods Hole Oceanographic Institution

Joint Program in Oceanography/ Applied Ocean Science and Engineering

DOCTORAL DISSERTATION

Shelf Currents, Ice and Wind:
A Numerical Modeling Study

by

Sarah L. Russell

February 2003

20030604 075

MIT/WHOI
2003-07

Shelf Currents, Ice and Wind:
A Numerical Modeling Study

by

Sarah L. Russell

Massachusetts Institute of Technology
Cambridge, Massachusetts 02139

and

Woods Hole Oceanographic Institution
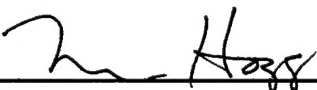Woods Hole, Massachusetts 02543

February 2003

DOCTORAL DISSERTATION
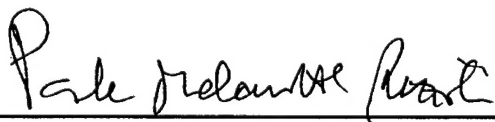
Approved for Distribution:

Nelson Hogg, Chair
Department of Physical Oceanography

Paola Malanotte-Rizzoli
MIT Director of Joint Program

John W. Farrington
WHOI Dean of Graduate Studies

AQM03-08-2108

Shelf currents, ice and wind: A numerical modeling study

by

Sarah L. Russell

B.A., Pomona College (1994)

Submitted in partial fulfillment of the requirements for the degree of

Doctor of Philosophy

at the

MASSACHUSETTS INSTITUTE OF TECHNOLOGY

and the

WOODS HOLE OCEANOGRAPHIC INSTITUTION

February 2003

Author . . . .
Joint Program in Physical Oceanography
Massachusetts Institute of Technology
Woods Hole Oceanographic Institute
December 3, 2002

Certified by . . . .
Paola Malanotte-Rizzoli
Professor, Massachussetts Institute of Technology
Thesis Supervisor

Certified by . . . .
Breckner Owens
Senior Scientist, Woods Hole Oceanographic Institute
Thesis Supervisor

Accepted by . . . .
Carl Wunsch
Chairman, Joint Committee for Physical Oceanography
Massachussetts Institute of Technology
Woods Hole Oceanographic Institute

Shelf currents, ice and wind: A numerical modeling study

by

Sarah L. Russell

Abstract

In this thesis, the effects of sea ice, downwelling favorable winds and barotropic background currents on shelf fronts are examined using numerical models. The models are configured with the characteristics of the East Greenland Current, north of the Denmark Strait, in mind. While the models are heavily idealized, basic physical parameters match the observed ocean.

The first part of the thesis uses a three dimensional, primitive equation model to examine the behavior of a shelf front under steady, along shelf winds and barotropic currents. The wind stress generates shoreward surface Ekman transport and the barotropic current generates an offshore bottom Ekman transport. In both cases, the Ekman transport causes the creation of mixed layers and a relationship describing the mixed layer thickness is derived relating the cross shelf flux of density to the along shelf flux of density. When there is a barotropic inflow, the cross shelf Ekman mass transport is balanced by a return flow of mass in the interior. When there is a wind stress, in the present model configuration, the influence of the offshore boundary obscures the effect of the Ekman layers.

The second part of the thesis focuses on the ice-ocean interaction using a simple, two layer, one dimensional toy model. The interaction of sea-ice, geostrophic currents, and wind are examined. In the presence of a current and the absence of wind, the ice is transported downstream with the current. In the presence of wind and the absence of a current, the net ice-ocean transport is perpendicular to the wind, as is expected for Ekman layer theory. The two layer system acts like a poorly resolved Ekman spiral: the ice has down wind and shoreward transport while the ocean has up wind and shoreward transport.

Thesis Supervisor: Paola Malanotte-Rizzoli
Title: Professor, Massachussetts Institute of Technology

Thesis Supervisor: Breckner Owens
Title: Senior Scientist, Woods Hole Oceanographic Institute

Acknowledgments

I would like to thank my advisors, Paola Rizzoli and Breck Owens, for their support, advise and aid over the years, particularly during the last two, very difficult years. Their understanding, encouragement and willingness to make accommodations made the completion of this thesis possible. Committee members Dave Chapman and Glen Gawarkiewicz both suffered through a ridiculous number of committee meetings and provided a great deal of useful feedback. Thank you! The SPEM code, with many invaluable diagnostic tools, was provided by Dave Chapman. Also, thanks to Steve Lentz who agreed to chair my defense.

Discussions with Tom Rossby, Bill Large, Matthew Hecht, Scott Doney, Jochem Marotzche, Rebecca Woodgate, Knut Aagaard and Jason Goodman greatly influenced this work at varying stages of its development, from proposal to completion.

Year mates who struggled through classes with me, cruise mates who hung over the rail watching charismatic macrofauna with me, officemates who tolerated my rants and other grad students who hunted free food with me, thank you. You made grad school interesting, fun and tolerable. Special thanks to Judith Wells, Juan Botella, Caixia Wang, Galen McKinley, Brian Arbic and Jason Goodman. Also, a special thanks to the department administrators who have been so kind and helpful over the years. In particular, Helen Dietrich, Lisa McFarren, Ronnie Schwartz, Stacey Frangos, Linda Meinke and Julia Westwater.

My colleagues at the Middlesex School have been particularly kind while I completed this thesis. John Bean, Julia Crockett, Natalie Soule, Alan Proctor, and Deirdre Ling have all been especially helpful.

Thanks to the friends who helped me keep my sanity. Story tellers, poets and dreamers, you re-energize me when my spirit is down. Rob, Storm, Vaughn, Will, Mary, Denis, Marc, Rebecca, Sean, Skaven, Chad, Elie, Jason, Megan, Shane and my beloved wife Leslie: without your support, I would have quit years ago.

Thanks to the teachers who encouraged me to pursue my interest in science and

math: Ms. Kaplan, Ms. Moore, Mr. Burke, Ms. Fiotakis, Mr. Walnezik, Dr. Zook and Dr. Hazlett. I hope I will be able to follow in your footsteps.

Finally, the support of my family has never wavered. Leslie, you lift my soul and give me courage to face each day. I may have started this adventure on my own, but you gave me the strength to finish it. Uncle Rick, Tee, and David, thank you for making me laugh and helping me keep perspective. There is more to life than graduate school and sometimes it is hard to remember that. Mom and Dad, you taught me how to dream, gave me the skills to chase after those dreams and encouraged me to reach for the unreachable star. Thank you.

Contents

List of Figures

11

12

13

16

18

19

21

Chapter 1

Introduction

1.1 Overview

The Greenland-Iceland-Norwegian Sea (GIN Sea) is a transition region between the Arctic and Atlantic oceans. It is bounded on the west by Greenland and on the east by Norway (figure 1-1). To the south, the GIN Sea is bounded by the Atlantic Ocean. Between the Atlantic Ocean and the GIN Sea is the Greenland-Scotland ridge which runs from the Shetland islands, past the Faroe Islands, to Iceland and then on to Greenland. The region between the Shetlands and the Faroes is called the Faroe-Shetland channel and it has a maximum depth of about 850 m. Between the Faroes and Iceland is the Iceland-Faroe ridge and it has a maximum sill depth of about 500 m. Between Iceland and Greenland is the Denmark Straits, with a maximum sill depth of 600 m. To the north, the GIN Sea is bounded by the Arctic Ocean. The deepest passage between the GIN sea and the Arctic ocean is between Greenland and Spitzbergen in the Fram Strait. The Fram Strait has a depth of 2600 m. Between Spitzbergen and Norway is a shallow entrance to the Barents Sea, with a sill depth of 350 m.

Many water masses have been identified in the Greenland-Iceland-Norwegian Sea. Mauritzen (1996a) discusses many of them. This discussion will focus on two water
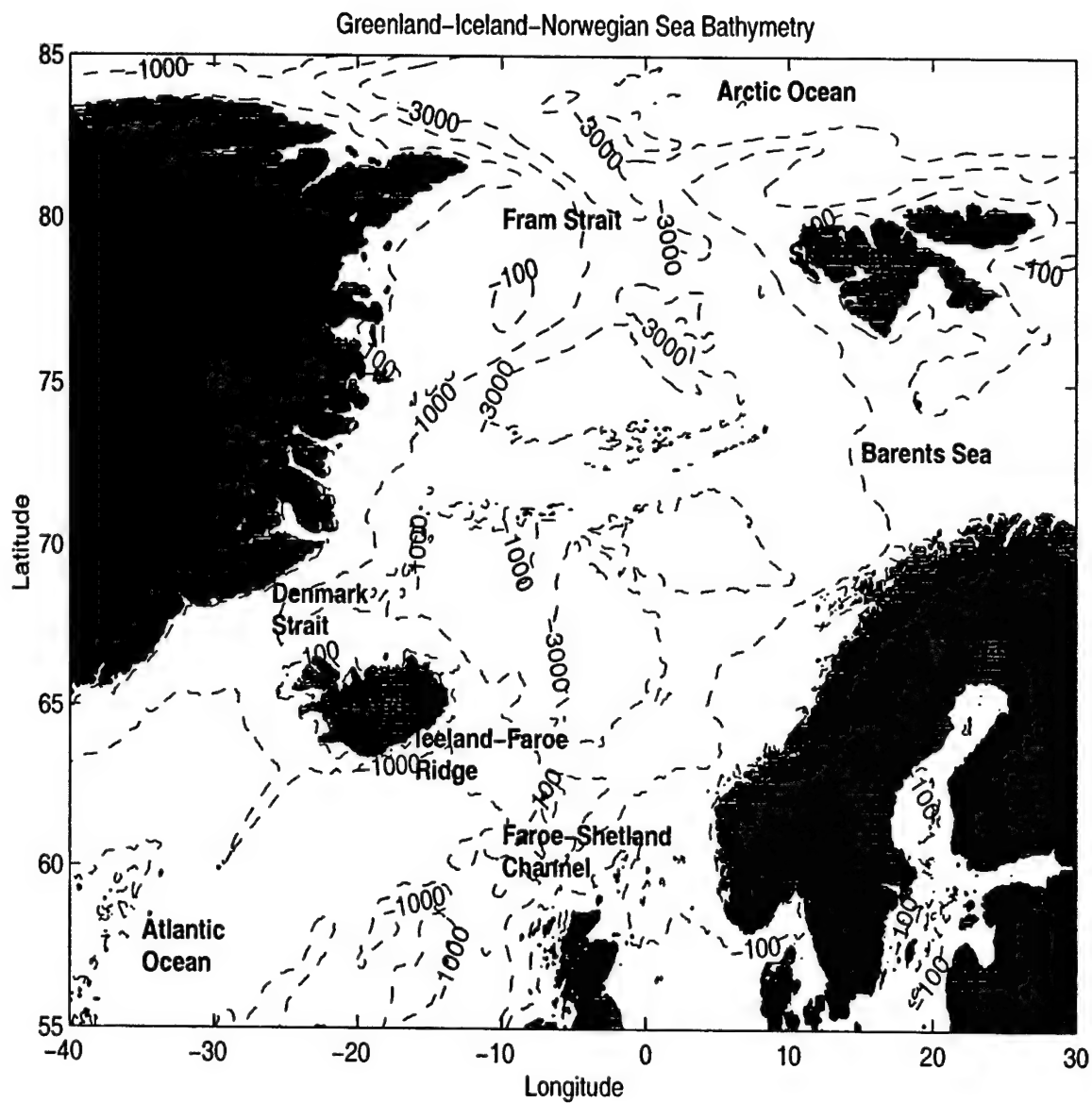
Figure 1-1: The bathymetry of the GIN Sea region. The 100, 1000 and 3000 m isobaths are shown.
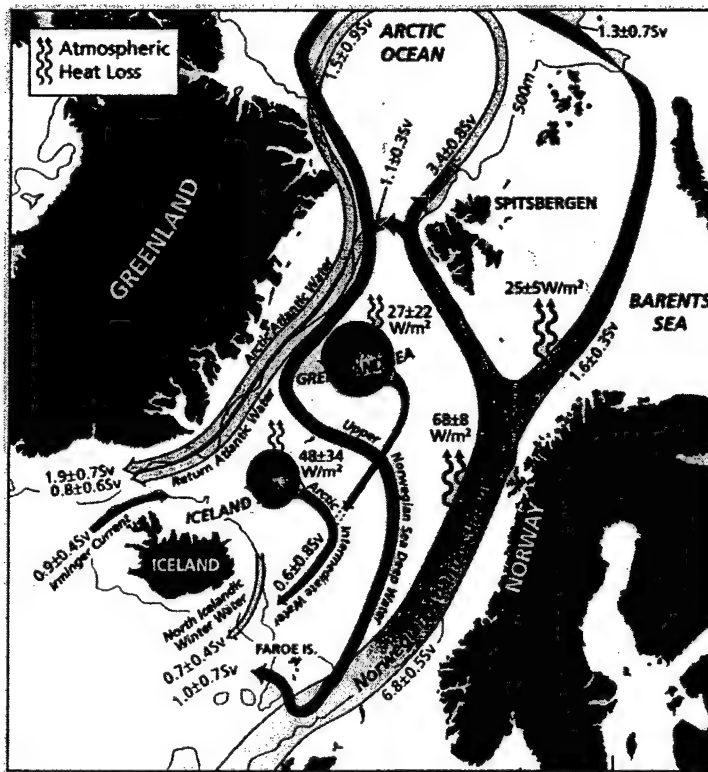
Figure 1-2: The results of an inverse model which estimates the mass and heat fluxes throughout the GIN Sea basin. From Mauritzen (1996b).

masses, defined as in Mauritzen (1996a). Atlantic Water originates from the North Atlantic and it is defined as water with a maximum in both temperature and salinity. Its temperature in the basin ranges from about 10° C near the inflow along the Faroe ridge to about 3° C on the western side of the basin. Its salinity is generally greater than 35 PSU. Polar Water originates from the Arctic Ocean surface water and it is defined as water with a minimum in salinity. Its temperature is typically below 0° C and its salinity is typically less than 35 PSU.

The circulation of the Greenland-Iceland-Norwegian Sea is summarized below, based on the picture presented in Mauritzen (1996a,b) (figure 1-2). Warm, salty Atlantic Water flows northward into the basin through the Faroe-Shetland channel and divides into several components. One branch enters the Arctic Ocean through the Barents Sea (Gawarkiewicz and Plueddeman, 1995). Another branch enters the Arctic

25

Ocean through Fram Strait, along the west coast of Spitzbergen. The remainder of the Atlantic Water is either modified in the basin and returned to the Atlantic as surface water or becomes sufficiently dense it sinks to depth, becoming the northern-most branch of the meridonal overturning cell. Cold, fresh Polar Water and sea-ice flows southward out of the Arctic Ocean through Fram Strait and into the Atlantic Ocean (Aagaard and Carmack, 1989).

Much of the meridonal circulation in the Greenland-Iceland-Norwegian Sea is carried by currents along the margins of the basin (Mauritzen 1996a,b). On the eastern boundary, the Norwegian-Atlantic current brings warm Atlantic Water northward (Poulain et al., 1996). The warm water loses heat to the atmosphere and gives northern Europe a relatively mild climate compared with other regions at similar latitudes. The Norwegian-Atlantic current is responsible for the year-round ice free conditions along the coast of Norway. The cooled Atlantic Water, still relatively warm, enters the Arctic Ocean through the Barents Sea and Fram Strait, forming a mid-level temperature and salinity maximum.

On the western margin of the basin is the cold, southward flowing East Greenland Current (Manley et al., 1987 and Bourke et al., 1987). The East Greenland current north of Denmark Strait has a surface component of Polar Water. At depth, there is a southward transport of warmer, saltier, modified Atlantic and Arctic water which forms the Denmark Strait overflow water when it passes over the sill between Iceland and Greenland (Mauritzen 1996a,b). Additional references discussing the East Greenland Current are discussed in section 1.3.

The wind over the Greenland-Iceland-Norwegian Sea drives a seasonal barotropic gyre with a large winter transport and a small summer transport (Woodgate et al., 1999). Along the western margin of the basin, a barotropic western boundary current develops with a variation in seasonal transport of about 20 Sv. The barotropic western boundary current closes the gyre's circulation. It does not extend northward of Fram Strait or southward of Denmark Strait. It is superimposed on

the through-flow, making it difficult to distinguish between the two systems midway between Denmark and Fram Straits.

The East Greenland Current is ice covered throughout the year, due to advection of ice out of the Arctic Ocean. In the winter, the ice edge extends much further into the basin of the Greenland Sea than the East Greenland Current, which hugs the shelf and slope. It is likely that the sea ice offshore of the East Greenland Current is primarily locally formed and not advected out of the Arctic Ocean (Pawlowicz, 1995 and Pawlowicz et al., 1995).

Blindheim et al. 2000, using repeated sections and long term weather stations, observe a long term upper layer decrease in temperature and salinity throughout the Nordic Seas. Their data spans nearly forty years. They attribute this change to an increase in the North Atlantic Oscillation (NAO) index and the shift in large scale wind forcing that is associated with variation in the NAO. They argue that during high NAO years, there is an increased transport of Polar Water from the Arctic Ocean in the East Greenland current and a decreased inflow of Atlantic Water across the Iceland-Scotland ridge. As the boundary current water mixes into the interior, the interior water decreases its density and salinity.

This thesis seeks to develop an understanding of the interactions between density driven shelfbreak currents such as the East Greenland Current, ambient barotropic currents and surface stress forcing. Two sources of surface stress are considered in this work: wind and sea ice. Wind is a spatially homogeneous stress when it is forcing small scale features such as shelfbreak currents. Sea ice may create a surface stress curl because cold currents, such as the East Greenland Current, are often partially covered in ice.

1.2 Motivation

The NCAR Climate Systems Model (Boville and Gent, 1998) is a coupled ocean, atmosphere, land and sea-ice model which attempts to model the global climate and understand teleconnections between many areas of the planet. One of the problem regions of the model is the behavior of the Greenland-Iceland-Norwegian Sea (Bryan (1998), Capotondi and Holland (1998) and Boville and Gent (1998)). When the ice and ocean components of the model are coupled together, the edge of the Arctic Ocean ice pack extends further southward than is observed. The Barents Sea and much of the Greenland-Iceland-Norwegian Sea becomes ice covered. Transport between Spitzbergen and Norway reverses from delivering warm Atlantic Water to the Arctic Ocean to delivering cold Polar Water to the GIN Sea. Within a few years, the GIN Sea is capped by a layer of fresh water.

The northward heat and mass flux across the Faroe-Shetland ridge in the NCAR model agrees well with the transports in the inverse model of Mauritzen (1996a,b). The North Atlantic Drift Stream in the NCAR model delivers heat and mass into the GIN Sea at a rate consistent with observations of the real world. However, the NCAR model disagrees with the inverse model heat and mass fluxes both at the passage between Norway and Spitzbergen and at Fram Strait. A possible explanation for this discrepancy is discussed below.

The northward flux of heat and mass in the model across the Faroe-Shetland ridge agrees with observations. The North Atlantic delivers the correct amount of heat into the Norwegian Sea. However, because it is a coarse resolution model, it fails to resolve the narrow, fast Norwegian-Atlantic Current. The Norwegian-Atlantic current in the model is about an order of magnitude wider than is observed in the real ocean. If the transport is the same with a larger area, the water speed must be slower.

Poulain et al. (1996) observe the Norwegian-Atlantic current with drifters and find speeds of in excess of 40 cm/s in two cores of the current. Orvik et al. (2000), through repeated sections and a four year current meter array, observe that the Norwegian

Atlantic Current has two strong branches, superimposed on a broader, slower background flow. The shoreward jet is narrow (30-50 km), topographically trapped, and has maximum speeds of about 120 cm/s. The offshore branch is an unstable frontal jet with maximum speeds of about 90 cm/s. The high speed jets are superimposed on a broad, slower current but it is the water in the jets which is focused on, below. The NCAR model has speeds of less than 10 cm/s in a fairly uniform slow current. As a result, the residency time of water off the Norwegian coast in the core of the jet, as it travels from the Faroe-Shetland ridge to the north coast of Norway, increases from the observed few months to over a year. Other global ice-ocean coupled GCMs have similar difficulties in the GIN sea (M. Holland, personal communication, 1996).

In an effort to understand this discrepancy, the Norwegian-Atlantic current is modeled as a jet in the form

$$v(y) = Cye^{-\frac{y^2}{\lambda^2}} \tag{1.1}$$

where y is the cross-stream coordinate, λ is the stream width and C is a constant such that

$$T = \int_{-H}^{0} \int_{0}^{L} v \, dy \, dz \tag{1.2}$$

T is the transport across the Faroe-Shetland ridge, H is the thickness of the current and $L = 2.5\lambda$, or the cross stream distance where the current carries a significant transport. Two different profiles of $v(y)$ are shown in figure 1-3 for choices of λ corresponding to the observed stream width for the Norwegian Atlantic current and the width of the Norwegian Atlantic current in the NCAR model. In this simple model, there is no mixing and

$$T_{fs} = T(x) \tag{1.3}$$

where T_{fs} is the transport over the Faroe-Shetland Ridge and $T(x)$ is the transport at any point, x, between the Iceland-Faroe Ridge and Spitzbergen. From Mauritzen (1996b), $T_{fs} = 6.8 \pm 0.5$ Sv. The direct observations of Orvik et al. (2000) estimate the transport is about 5 Sv.
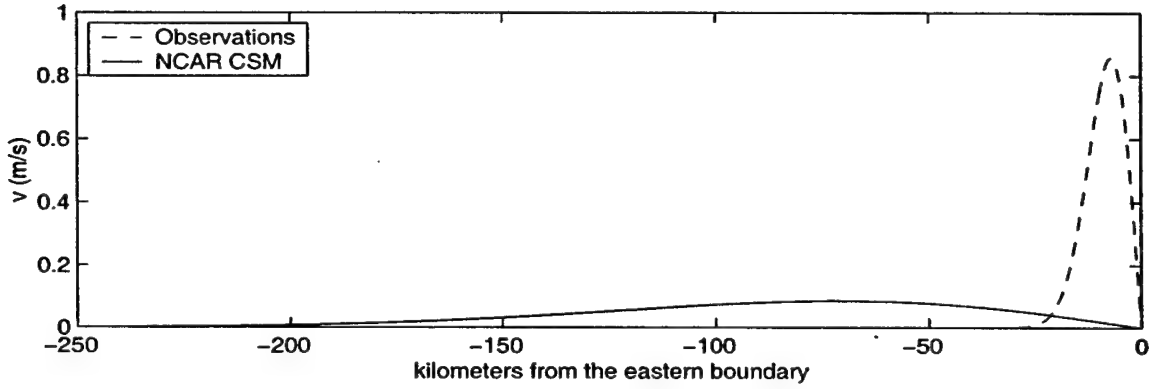
Figure 1-3: The velocity profiles for the two streams. Velocities of both streams are normalized to a transport of 5 Sv.

The northward heat flux across the Faroe-Shetland Ridge is

$$H_{fs} = c\rho_o T_{fs} t_{fs} \qquad (1.4)$$

where t_{fs} is the temperature of the water entering from the Atlantic Ocean, c is the specific heat of water and ρ_o is the average density of the water. The core of the current has water with a temperature greater than $10°$ C with an average temperature of about $7°$ C (Mauritzen, 1996b). The northward heat flux at any point, x, from the Iceland Faroe Ridge to Spitzbergen is

$$H(x) = H_{fs} - QLx \qquad (1.5)$$

where Q is the constant cooling the current experiences along the coast of Norway. According to Mauritzen (1996b), $Q = 68 \pm 8$ W/m^2. The temperature at x is

$$t(x) = \frac{H(x)}{c\rho_o T_{fs}} \qquad (1.6)$$

The along channel temperatures for the two current profiles, assuming an initial temperature of $10°$ C, are shown in figure 1-4. The fast, narrow profile only cools about $0.5°$ C while the slower profile cools almost $4°$ C. Harris et al. (1998) observe

30
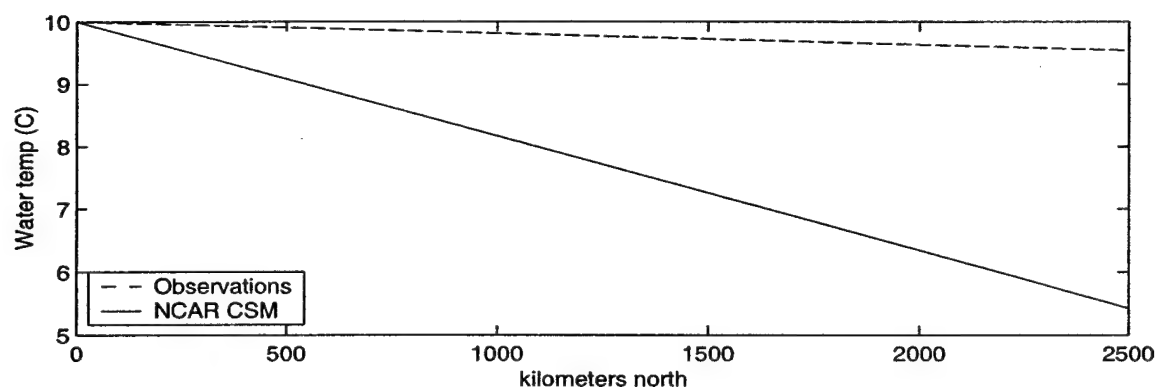
Figure 1-4: The temperature of the water as a function of distance north of the Iceland-Shetland Ridge. The temperature decreases linearly with time.

the Atlantic Water north of Norway, in the Barents sea, and find water temperatures greater than 9° C, a temperature which is consistent with the cooling of the fast, narrow jet in the simple model. The temperature of the NCAR model is about 5° C in the same region in the ocean, consistent with the cooling of a broad, slow jet.

This is a very simple model. It neglects both vertical and horizontal mixing. The dispersion of drifers in Poulain et al. (1996) suggest there is substantial horizontal mixing in and out of core of the jets. Furthermore, Mauritzen (1996b) suggests that one of the ways the North Atlantic water conserves its heat is that it is subducted as it flows northward. Finally, the results of Mauritzen (1996a,b) are averaged over a large area while the cores of the jets observed in Poulain et al. (1996) and Orvik et al. (2000) are very small. It is possible the behavior of the small, fast jets should not be directly compared to the broad wide northward flow that carries the majority of the North Atlantic Water.

Despite all of these caveats, the simple model does an acceptable job predicting the temperature at Spitzbergen for the two different configurations and it explains the problems of the NCAR model. The broad, slow current of the NCAR model looses more heat to the atmosphere over its longer transit from the Iceland-Faroe ridge to Spitzbergen than the swift, narrow shelfbreak current in the real ocean. Because the water at Spitzbergen is cooler than it should be, it is easier to freeze. This allows for

31

the formation of ice across the basin and leads to the other changes observed in the model circulation and meridonal overturning.

The difficulties with the NCAR model, and other similar models, are derived from inadequate resolution of the small scale shelfbreak currents. The cross stream resolution of the model at the Iceland Faroe ridge is about 20 km and the width of the current is about 20 km. Failure to resolve the shelfbreak current results in a major shift in circulation of the GIN Sea basin. The change in circulation of the GIN sea basin has global consequences by altering the rate at which North Atlantic Deep Water is formed and causing a shift in its properties.

While the shelfbreak currents are small features in the ocean, at high latitudes they often transport a substantial fraction of the heat and mass in the ocean. They are a critical link in the global circulation which is only partially understood.

1.3   Observations of the East Greenland Current

Observations of the East Greenland Current and Front are difficult because the system is ice covered for much of the year. There have been a variety of estimates of the transport of the current. Early hydrographic estimates of 2-5 Sv were made by Jakhelln (1936), Mosby (1962) and Timofeyev (1963). For a summary of the early observation programs see Aagaard and Coachman (1968). Methods which attempt to conserve mass, heat, and other tracers, produced similar estimates. Aagaard and Greisman (1975) estimate a transport of 7 Sv and Mauritzen (1996a,b) estimates 4 Sv. Schlichtholz and Houssais (1999), in an inverse modeling study of just Fram Strait, estimate an Arctic outflow of 5 Sv.

Bourke et al. (1987) combine two surveys, one conducted in 1979 and one conducted in 1984, of the East Greenland Shelf between 76° N and 83° N. They find the water flows on the shelf in a clockwise gyre with a baroclinic northward transport near the coast of 0.85 Sv and a baroclinic southward transport near the shelf break
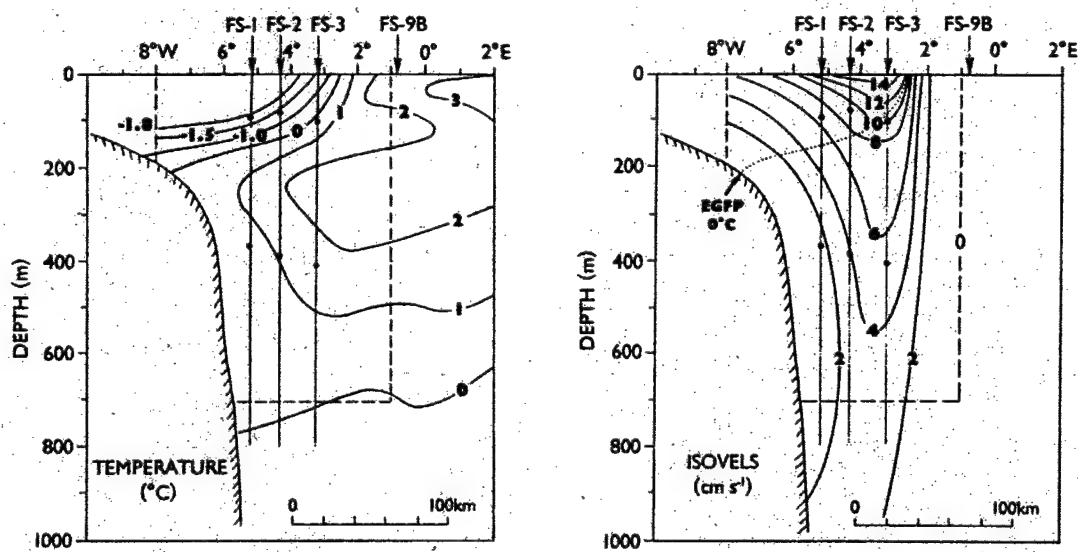
Figure 1-5: The annual mean temperature and northward velocity from current meters moored in Fram Strait at 79° N. From Foldvik et al. (1988)

of 1.47 Sv. The net southward transport in their survey is 0.89 Sv.

Current meter arrays have also been used to study the East Greenland Current. Foldvik et al. (1988), with a one year deployment at 79° N, observe a transport of about 3 Sv through Fram Strait above 700 m. About half of the transport is barotropic and half baroclinic. The annual mean temperature and velocity they observe is shown in figure 1-5. If Polar Water is defined as water with a temperature less than 0° C, there is a clear temperature front visible in the annual mean. The 0° C isotherm intersects the bottom at the shelf break. The front is associated with a surface intensified jet, with a speed of about 15 cm/s at the surface. Although the current meters do not measure it, the temperature front coincides with a salinity front. The water on the shelf is cold and fresh and the water over the slope is salty and warm. In density, the two properties mostly compensate. There is a density difference of about 0.9 kg m^{-3} (Mauritzen (1996a,b)) across the front, with lighter water on the shelf.

Two different current meter deployments have been done at 75° N. Aagaard and Coachman (1968) discuss an array which was in place over the winter and they observe a mostly barotropic transport of 35 Sv. Woodgate et al. (1999) observe a transport of

33
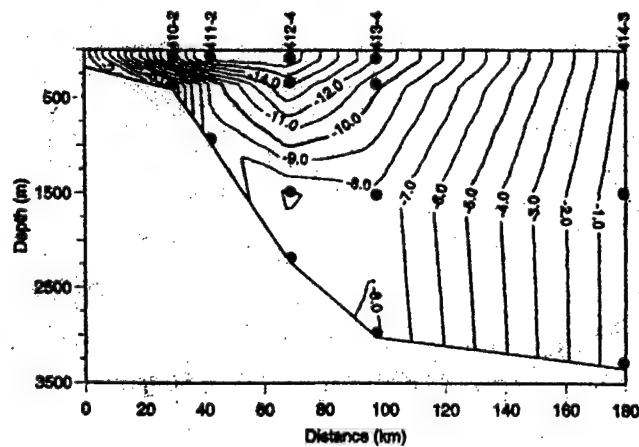
Figure 1-6: The annual mean velocity field at 75° N, off the coast of Greenland. From Woodgate et al. (1999).

21 ± 3 Sv in the annual mean with a seasonal cycle ranging from 11 Sv in the summer to 37 Sv in the winter. Figure 1-6 shows the annual mean velocity field they observe. There is still a surface intensified jet but the velocity field is far more barotropic than it is near Fram Strait (figure 1-5).

There is quite a discrepancy between the transports observed by mid-basin current meters and the other measurements of the East Greenland Current. Woodgate et al. (1999) argue that the difference is caused by a barotropic, wind driven gyre which develops in the GIN Sea during the winter. In the summer, the winds are mild and there is not a strong gyre. In the winter, the winds are strong and the East Greenland Current is superimposed with the barotropic western boundary current of the gyre.

These studies focus on the current without paying particular attention to the sea ice, except as a hindrance to observations. In 1979, 1983 and 1984, an extensive field observation program was carried out known collectively as the Marginal Ice Zone experiments, or MIZEX. (J.A. Johannessen et al. 1983 and J.A. Johannessen et al. 1987) The thrust of these experiments is on the ice edge and not on the interaction with the East Greenland Current. They create a fairly comprehensive picture of the behavior of the ice edge and the underlying ocean but the field area is too far east

34
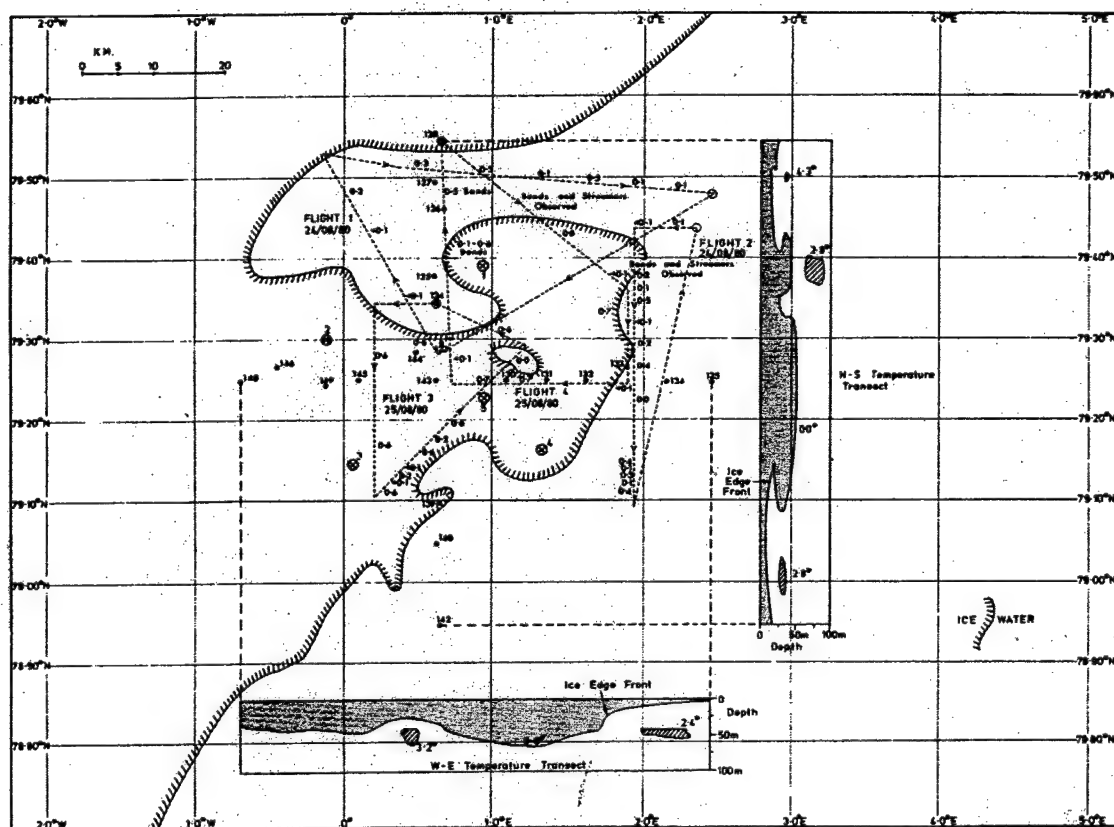
Figure 1-7: The ice edge (defined where ice concentrations exceed 0.8) deformed in response to an underlying ocean eddy. Dotted lines indicate paths of helicopter flights which mapped the feature. Insets show the temperature profiles beneath the ice. From Wadhams and Squire (1983).

to sample the East Greenland Current. The current regime under the ice edge in the field area is filled with eddies, consistent with the transient response seen in the current meter array of Foldvik et al. (1988). In response to the eddies, the ice edge is deformed into very visible whirls. A schematic of an ice edge deformed in response to an underlying eddy is shown in figure 1-7. (Wadhams and Squire, 1983)

At one point during the 1979 MIZEX cruise, there were persistent winds blowing parallel to the ice edge for several days (figure 1-8). Surveys of the ice edge were conducted during this time. The upper 18 m layer of water was well mixed. Initially, between a depth of about 18 m and 30 m, there was a strong, flat pycnocline. After

35
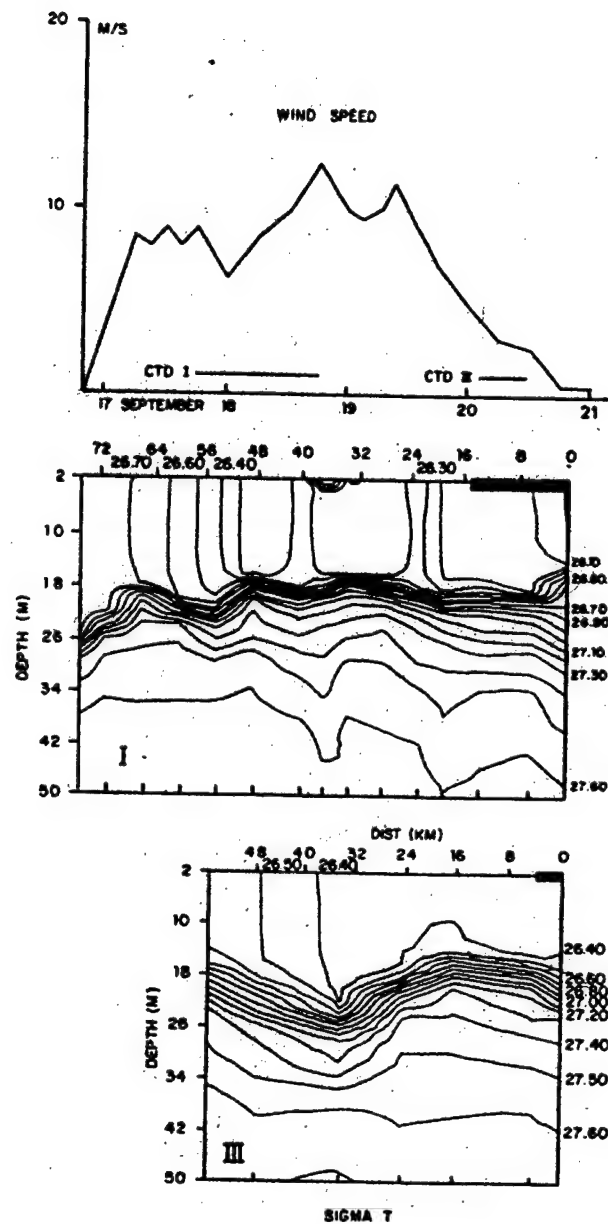
Figure 1-8: The pycnocline response to persistent, 10 m/s, along ice edge winds. Top panel shows the wind speed versus time. The middle panel shows the density structure on September 18, 1979. The bottom panel shows the density structure on September 20, 1979. The $26.4\sigma_t$ contour was displaced about 6 m in two days. From J.A. Johannessen et al. (1983).

several days of persistent winds, the isopycnals were observed to be domed upwards near the ice edge. This was attributed to differential Ekman transport across the ice edge, causing ice edge upwelling.

During MIZEX, it was observed that when the wind is blowing off the ice, there are often bands of regularly spaced ice floes, aligned perpendicular to the ice edge. Muench et al. (1983) use linear wave theory and show that the spacing and propagation of the bands is consistent with the generation of internal waves at the ice edge through differential wind stress in the ice covered and ice free regions. The waves propagate away from the ice edge, carrying the bands of ice away with them.

Martin and Wadhams (1999) process satellite imagery of sea ice through an algorithm which identifies features in the ice and tracks them through time. This allows them to estimate the spatial distribution of sea ice flux. They observe a strong southward flux of ice along the East Greenland Current. The ice edge is dominated by eddies with diameters of the order of 10 km. The median ice velocity is between 5 cm/s in the summer and 15 cm/s in the winter.

In the annual average, the winds along the East Greenland Current are southward, parallel to the ice edge, the front and in the same direction as the current (da Silva, 1994). This study focuses on annual average conditions, rather than the transient responses to synoptic weather events such those observed in MIZEX.

1.4   Previous modeling work

1.4.1   Shelf Currents

Chapman and Lentz (1994) develop a three-dimensional primitive equation channel model to look at the behaviour of buoyant river out flows onto the shelf. The river water enters a homogeneous denser fluid, turns in the direction of Kelvin wave propagation, and develops into a front downstream of the inflow. The front carries a transport, set by the inflow of river water at the boundary. Through thermal wind,

there is a shear in the current's velocity, set by the density difference across the front.

Initially, before much light water enters the channel, the front is in shallow water, close to the channel wall. Because the transport of the front is set by the boundary condition and the shear is set by the density difference across the front, the water velocity at the bottom is non-zero. The velocity at the bottom drives an offshore transport in the bottom Ekman layer which carries light coastal water under heavier interior water. Convective mixing occurs and the front shifts off shore. As the front moves offshore, the shear causes a small region on the offshore side of the front to develop a reversed jet. Underneath the reversed jet, the Ekman transport is shoreward. The front continues to move offshore until the transport under the entire front is shoreward. The adjustment process is shown in figure 1-9.

The front reaches an equilibrium depth beyond which it does not move. Yankovsky and Chapman (1997) derive a scaling for the trapping depth, h_b, of the front:

$$h_b = \sqrt{\frac{2 f_0 T}{g'}} \tag{1.7}$$

where T is the transport in the front and g' is the reduced gravity, $\frac{g \Delta \rho}{\rho_o}$. Both T and $\Delta \rho$ are parameters specified as inflow boundary conditions.

Chapman (2000) expands the scope of the previous papers to include both stratification in the offshore ocean water and a shelf break and finds that the trapping mechanism, first identified in Chapman and Lentz (1994), is so robust that the front does not attach to the shelfbreak but rather moves to the appropriate depth predicted by the scaling. Chapman (2000) also modifies equation 1.7 to account for stratification in the ocean interior. Chapman (2002) compares the adjustment and trapping of the front with two different mixing schemes: constant vertical mixing (as used in Chapman and Lentz 1994) and Mellor Yamada 2.0 (as used in Chapman (2000)). He finds that the trapping mechanism and the convergence in the bottom boundary remain the same while the frontal width and some of the details of the circulation
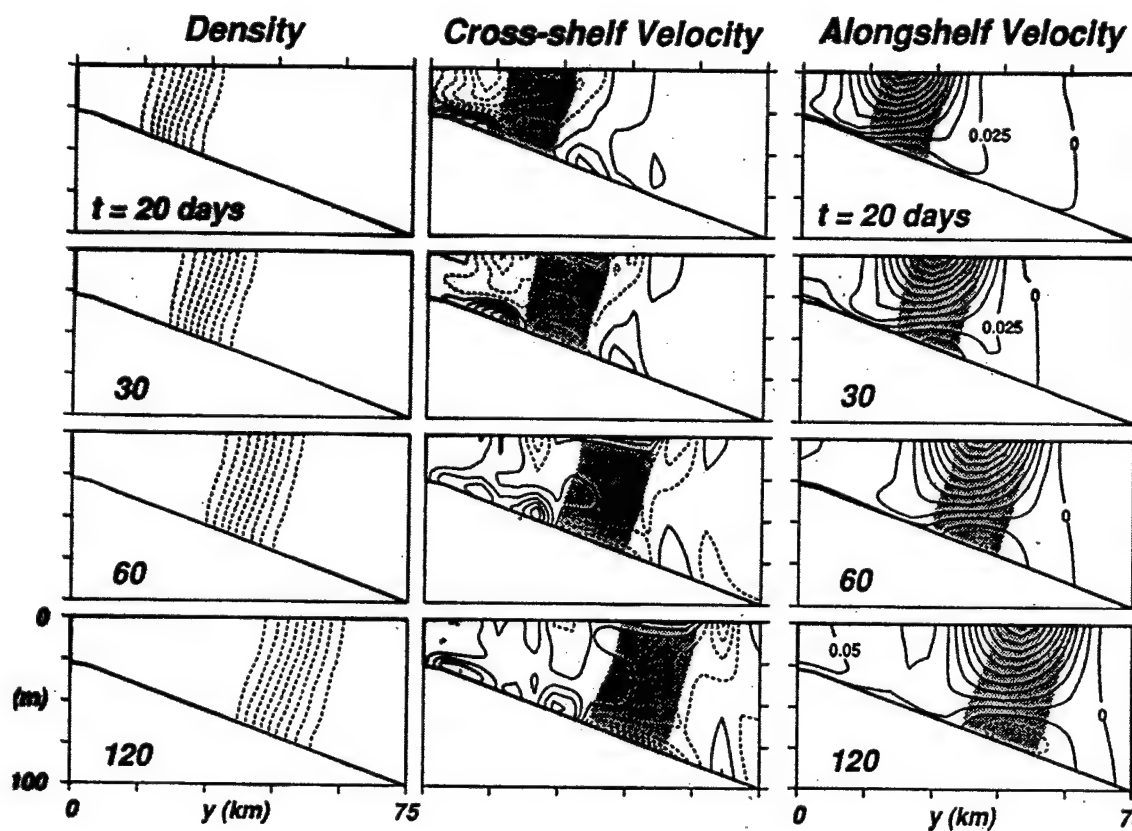
Figure 1-9: The density, cross shelf velocity and along shelf velocity during the adjustment of a buoyant front over a sloping bottom. Shading indicates the location of the density front. Negative contours are dashed. Contours for density anomaly are -0.9 to -0.1 by 0.1 with units of kg m^{-3}. Contours for cross shelf velocity are -0.0225 to 0.0375 by 0.005 with units m/s. Contours for along shelf velocity are -0.025 to 0.275 by 0.025 with units of m/s. From Chapman and Lentz (1994).

change.

The Chapman and Lentz (1994) trapping mechanism predicts a convergence in the bottom boundary layer. A different study with a slightly different trapping mechanism, Gawarkiewicz and Chapman (1992), also predicts convergence in the bottom boundary layer. For mass to be conserved, the convergence must drive an upward motion in the front. A number of observational programs have tested this prediction. Houghton and Visbeck (1998) released dye in the bottom boundary layer of a shelfbreak front and traced the dye up an isopycnal. Barth et al. (1998) examined the distribution of suspended sediment near the front and trace a plume of sediment upwards. Pickart (1999) develops a method using CTD data to track the detached bottom boundary layer.

Allen et al. (1995) and Allen and Newberger (1996) work with a two dimensional model (vertical and cross-shelf) of the Oregon shelf and slope. Allen et al. (1995) blow upwelling favorable winds over the domain and Allen and Newberger (1996) have downwelling favorable winds. In both cases, they study the development of a front from an initially uniform stratification. For upwelling favorable winds, the winds drive an offshore flux in the surface Ekman layer. At the coast, mass is balanced by a shoreward flow in the bottom Ekman layer and coastal upwelling. For downwelling favorable winds, there is a shoreward flux in the surface Ekman layer and mass is balanced by an offshore flow in the bottom boundary layer. Coastal downwelling drags light water down the slope, under heavier water. In both cases, a region of unstratified water develops near the coast and a front forms. Through thermal wind, a current develops along the front with transport perpendicular to the model domain.

Because Allen et al. (1995) and Allen and Newberger (1996) work with two dimensional models and the adjustment process of Chapman and Lentz (1994) requires the current to adjust to topography as it travels downstream, the two models can not be easily compared or rectified. A full three dimensional model, with wind, is needed to begin to understand the interaction between a front and the wind.

One close compromise was done by Middleton and Cirano (1999). They develop a three-dimensional model of the shelf and investigate the role wind plays in the system. Their model is a large closed domain with enhanced resolution near the shelf and shelf break. There is no throughflow of light water. They start the system with a uniform stratification and blow downwelling favorable wind over a section of the domain. As in Allen and Newberger (1996), Ekman transport drives the creation of a front. Through thermal wind, the front develops an along-shelf jet. The front and jet adjust to the bottom topography in a manner that is similar to Chapman and Lentz (1994).

1.4.2 Sea ice

The first primitive equation dynamic-thermodynamic ice model was developed by Hibler (1979). Others have improved his original formulations and implementations in an effort to make ice models more realistic and computationally affordable. In general, interest in the community has focused on developing sea-ice ocean coupled models that can be used either for mid-range weather forecasting or climate research. To allow for long integrations, such models must be coarse resolution. There has been little effort focusing on simple sea-ice dynamics.

One such simple dynamics experiment was done by Roed and O'Brien (1983). They created a 1.5 layer coupled ice-ocean model and blew wind over the domain, parallel to the ice edge. They examined the interaction of the ice edge with a stratified ocean. Their study is followed by Hakkinen (1986) who expanded their model to two dimensions. These papers explore the ice edge upwelling observed in MIZEX. The upwelling at the ice edge domes the isopycnals upwards and through thermal wind a jet develops along the ice edge. The stability of the ice edge jet under both steady and fluctuating wind (similar to a storm) were studied. They found both the ice edge jet and the shape of the ice edge itself are unstable. The instability has a growth rate of 3-5 days in ice edge upwelling favorable conditions.

41

This study aims to pick up where those studies left off, examining the simple dynamic interactions between sea-ice and underlying ocean currents and wind.

1.5   Organization

This thesis tries to understand how a shelfbreak current responds to surface stress which is either homogeneous, like the wind, or heterogeneous, like a partially ice covered surface. This study focuses on dynamic couplings and does not address the issues related to ocean or ice thermodynamics. The interaction illustrated in section 1.2 definitely contains a vital thermodynamic component, but it is unlikely the complex thermodynamics can be understood until there is a basic understanding of the dynamics.

Two different numerical models are used in this study. One model is SPEM, a σ coordinate, primitive equation model, developed by Haidvogel et al. (1991). The version of SPEM used was provided by D. Chapman and the configuration is similar to the channel model of shelfbreak currents presented in Chapman (2000). It is easy to modify SPEM to study the behavior of a current forced by wind. It is much more difficult to incorporate a full sea-ice model. For the sea ice part of this study, a second model was developed. The second model, called the "toy model", is a one dimensional, ice-ocean coupled model, similar to Roed and O'Brien (1983).

Chapter 2 focuses on the interaction between a shelf current, a barotropic inflow and the wind. Scaling arguments, thought experiments and numerical model experiments are presented which identify the effect of the wind alone, the barotropic current alone, and the wind and barotropic current together on the shelf current. While the system is complex, two different responses are identified. The wind stress alters the surface Ekman layer and the barotropic inflow alters the bottom Ekman layer and both Ekman layers cause the development of mixed layers in the front. In addition, the location of the front is modified by the barotropic forcing. It may also be modified

by wind stress.

Chapter 3 focuses on the interaction between a shelf current and sea ice, both with and without wind. In the absence of wind, the ice is advected along with the current while any changes in the velocity of the underlying geostrophic current spawn significant inertial oscillations. In the presence of wind, the complete ice-ocean system has transport to the right of the wind, by Ekman transport but the individual components have transports which resemble a two layer Ekman spiral: the ice has transport downstream and to the right of the wind while the ocean has transport upstream and to the right of the wind. Because the mass of the ice is much smaller than the mass of the water, the downstream ice velocity is much larger than the upstream water velocity.

Chapter 4 summarizes the results and conclusions and presents a variety of suggestions for future experiments.

Chapter 2

Buoyant shelf currents with "wind"

2.1 Introduction

Continental shelf breaks are sometimes associated with a transition in water properties. Cold shelf water encounters the warmer, saltier ocean interior water. The change in water properties creates a cross shelf density gradient, driving a density driven flow along the shelf break, parallel to the coast.

The East Greenland Shelf is typical of other shelves. The water on the shelf is light and fresh, originating from the Arctic Ocean and modified by ice melt. Seaward of the shelfbreak, the Norwegian and Greenland Sea water is substantially warmer and saltier, originating far to the south in the Atlantic Ocean (Bourke et al., 1987). Due to persistent ice cover over the shelf, far fewer observations have been made of the East Greenland Front and Current than have been made of the highly accessible Mid-Atlantic Bight. Foldvik et al. (1988) and Woodgate et al. (1999) each use current meter arrays, positioned across the shelfbreak at 79° N and 75° N respectively, to study the East Greenland Current. The current meters at 79° N record a mostly baroclinic transport of about 3 Sv through Fram Strait. The mid-basin current meters at 75° N record a steady, probably density driven, transport of about 8 Sv and a seasonally varying wind driven transport in excess of 20 Sv. The picture

that emerges from Woodgate et al. (1999) and Mauritzen (1996a,b) is that there are two components to the transport in the East Greenland current: a baroclinic, density driven through flow and a seasonal barotropic wind driven flow confined to the Norwegian/Greenland basin.

In this chapter, the interaction between a density driven shelfbreak current, a barotropic background current and the wind is explored. This work confines itself to barotropic currents and winds with transport in the same direction as the shelfbreak current. Both the barotropic currents and the winds produce Ekman transports perpendicular to the density driven current. The way the boundary conditions are developed, neither the wind nor the barotropic inflow alters the potential vorticity of the imposed inflow.

Chapman and Lentz (1994) develop a three-dimensional primitive equation channel model to look at the behavior of buoyant river outflows onto the shelf. The river water enters a homogeneous denser fluid, turns in the direction of Kelvin wave propagation, and develops into a front downstream of the inflow. The front does not move offshore indefinitely, but reaches an equilibrium depth beyond which it can not move. Yankovsky and Chapman (1997) derive a scaling for the trapping depth of the front. Chapman (2000) expands the scope of the previous papers to include both stratification in the offshore ocean water and a shelf break and finds that the trapping mechanism, first identified in Chapman and Lentz (1994), is so robust that the front does not attach to the shelfbreak but rather moves to the appropriate depth predicted by the scaling. Chapman (2002) explores the impact of different vertical mixing schemes on the frontal trapping and identifies which features of the fronts are robust, regardless of the mixing scheme.

Allen and Newberger (1996) work with a two dimensional model (vertical and cross-shelf) of the Oregon shelf and slope. They blow downwelling favorable winds over the domain and study the development of a front from the initial stratification. The winds drive a shoreward flux in the surface Ekman layer and mass is balanced

by an offshore flow in the bottom boundary layer. Coastal downwelling drags light water down the slope, under heavier water. Convective mixing removes the density inversion and a bottom mixed layer is formed. Over many days, the mixed layer grows and forms a front. Through thermal wind, a current develops along the front with alongshelf transport.

Allen and Newberger (1996) investigate an important dynamic in the coastal region: the interplay between the wind and coastal currents. However, the results of Chapman and Lentz (1994) suggests the downstream interaction between the front and friction on the sloping bottom plays a critical role in the behavior of shelf currents; a two-dimensional model simply can not encompass the critical dynamics.

Middleton and Cirano (1999) develop a three-dimensional model of the shelf and investigate the role wind plays in the system. Their model is a large closed domain with enhanced resolution near the shelf and shelf break. There is no throughflow of light water. They start the system with a uniform stratification and blow downwelling favorable wind over a section of the domain. As in Allen and Newberger (1996), Ekman transport drives the creation of a front. Through thermal wind the front develops an along-shelf jet. The front and jet adjust to the bottom topography in a manner that is similar to Chapman and Lentz (1994).

The motivation of this study is to come to some understanding of how the density driven throughflow of the East Greenland Current interacts with the barotropic component and the wind. Woodgate et al. (1999) discuss one possible interaction. They observe the core of the East Greenland Current (and presumably the foot of the front, though they do not observe it directly) move shoreward in the winter when the wind and barotropic transport are at a maximum.

This study uses Chapman and Lentz (1994) as a starting point. The numerical channel model of the Greenland shelf used is developed in section 2.2. In section 2.3, a conceptual picture of the model physics is discussed, with particular emphasis on the behavior of the model under various wind stresses and barotropic inflows. While

46

the wind stress and barotropic inflow imposed on the model are independent of each other, it seems likely that a wind stress will drive a particular barotropic current, and the relation between wind stress and barotropic current is derived in section 2.4. This relationship is used to choose appropriate values for the bottom drag coefficient and maximum vertical mixing allowed. The barotropic inflow and wind stress affect the shape and size of the mixed layers in the model and a relationship predicting the mixed layer depth based on the wind stress and barotropic inflow is developed in section 2.5. Finally, the predictions are tested and discussed in reference to selected actual model runs in section 2.6 and conclusions are presented in section 2.7.

2.2   The numerical model

This study uses SPEM 5.1, a σ-coordinate primitive equation model that solves the momentum, density and continuity equations under the hydrostatic and Boussinesq approximations. The model is configured as a channel on an f plane.

The equations are:

$$\frac{\partial u}{\partial t} + u\frac{\partial u}{\partial x} + v\frac{\partial u}{\partial y} + w\frac{\partial u}{\partial z} - f_0 v = -\frac{1}{\rho_0}\frac{\partial p}{\partial x} + \mathcal{F}_u + \mathcal{D}_u \tag{2.1}$$

$$\frac{\partial v}{\partial t} + u\frac{\partial v}{\partial x} + v\frac{\partial v}{\partial y} + w\frac{\partial v}{\partial z} + f_0 u = -\frac{1}{\rho_0}\frac{\partial p}{\partial y} + \mathcal{F}_v + \mathcal{D}_v \tag{2.2}$$

$$\frac{\partial p}{\partial z} = -g\rho \tag{2.3}$$

$$\frac{\partial u}{\partial x} + \frac{\partial v}{\partial y} + \frac{\partial w}{\partial z} = 0 \tag{2.4}$$

$$\frac{\partial \rho}{\partial t} + u\frac{\partial \rho}{\partial x} + v\frac{\partial \rho}{\partial y} + w\frac{\partial \rho}{\partial z} = \mathcal{F}_\rho + \mathcal{D}_\rho \tag{2.5}$$

where (u, v, w) are the (x, y, z) components of the velocity vector, p is the pressure, ρ_0 is the background density, ρ is the density anomaly, f_0 is the Coriolis parameter set to a constant value and g is the acceleration due to gravity. $\mathcal{F}_u$, $\mathcal{F}_v$ and $\mathcal{F}_\rho$ represent

the forcing terms and $\mathcal{D}_u$, $\mathcal{D}_v$ and $\mathcal{D}_\rho$, represent the vertical and horizontal diffusive terms.

Equations 2.1 and 2.2 are the x and y momentum equations in the Boussinesq limit. Equation 2.3 is the z momentum equation in the hydrostatic limit. Equation 2.4 is the incompressible continuity equation. Equation 2.5 represents the evolution of the density field of the fluid. The model is described in detail by Haidvogel et al. (1991).

Figure 2-1 shows the model configuration. The model domain is a uniformly rotating straight channel with $f_0 = 1.4 \times 10^{-4}\,\mathrm{s}^{-1}$. x is the along-channel coordinate, positive downstream. y is the cross-channel coordinate, positive offshore. z is the vertical coordinate, positive upwards. The channel is 400 km long and 200 km wide. Between x=100 km and x=400 km, the depth increases linearly away from the coast with a depth at the coastal wall of 70 m and a depth at the offshore wall of 234 m. Between x=0 km and x=100 km, the isobaths are curved towards the coastal wall in an ellipse pattern, allowing the front to adjust naturally to the topography and develop an appropriate bottom boundary layer. The solution is not sensitive to details of the bathymetry. This technique is discussed in more detail in Chapman (2000).

A variety of model dimensions were tested and the smallest grid that satisfied the following conditions was used. The channel walls must not interfere with the front. The front must be fully developed before it reaches the downstream boundary. The depth of the water and slope of the bottom must be similar to the northeast coast of Greenland. When the model domain was selected, it was believed that such a configuration had been found; by the end of the study, it is believed that the channel is not wide enough and the offshore wall interacts with the front under some circumstances such as experiments with large wind stress. The repercussions of this interaction are discussed throughout the chapter.

The model grid has 321 points in the along-channel direction and 161 points in the cross-channel channel direction, giving a resolution of about 1.1 km in the along-

48
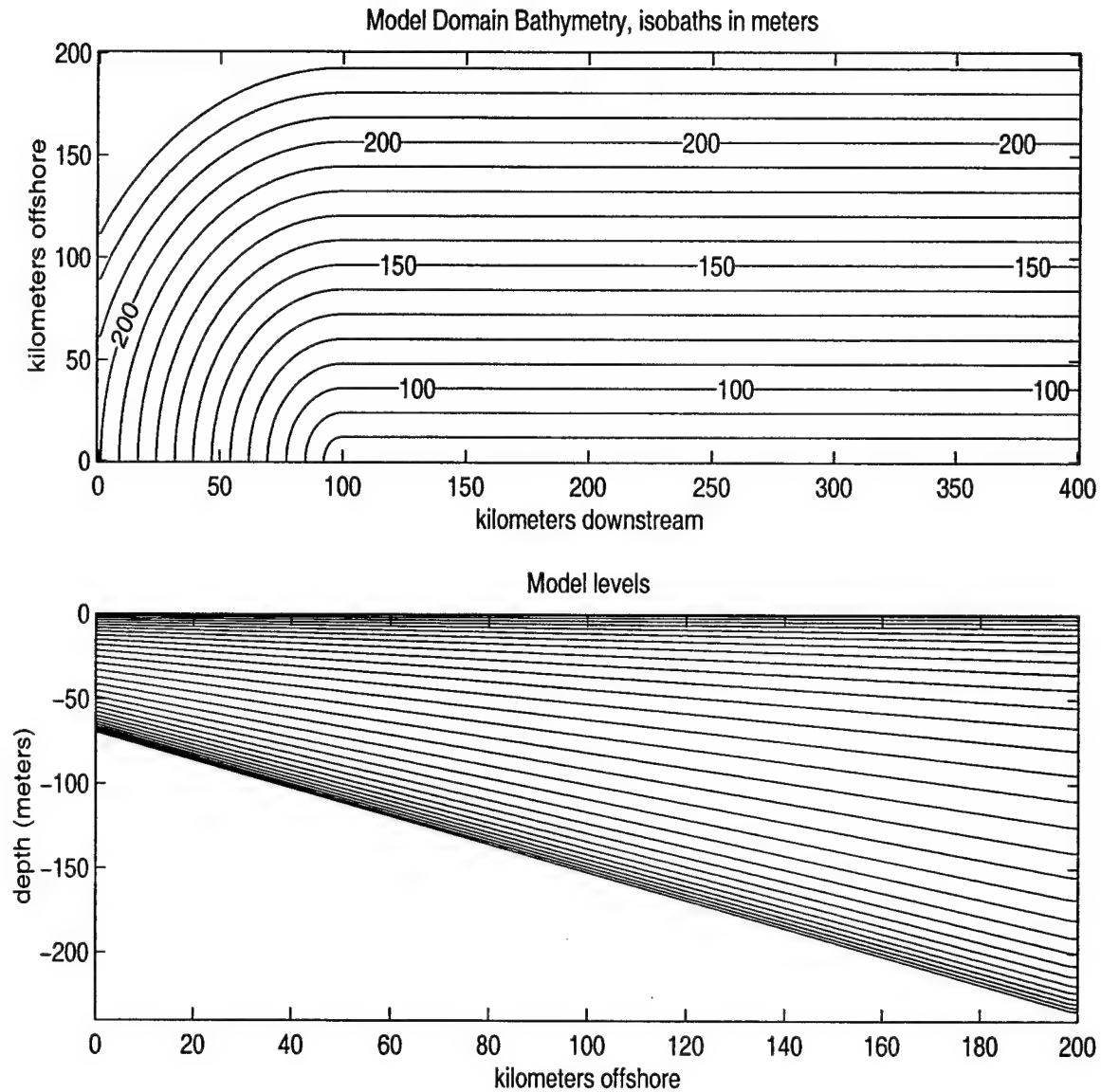
Figure 2-1: The model configuration. An inflow is imposed at x=0 km. There is an open boundary at x=400 km. There are solid walls at y=0 km and y=200 km. (a) The model bathymetry in meters, (b) A cross section of the model levels at x=200 km. The model levels follow the topography and are more closely spaced in the two boundary layers.

channel direction and 1.2 km in the cross-channel direction. This resolution amply resolves the baroclinic Rossby radius, which is typically about 10 kilometers for these experiments. There are 30 grid points in the vertical; the grid points are concentrated near the upper and lower boundaries. The Ekman layers are explicitly resolved. The model uses a stretched vertical coordinate that is described in detail in Hedstrom (1997). The model time step is 288 s (1/300th of a day).

The boundary conditions are as follows. A rigid lid is assumed at the surface ($w=0$ at $z=0$). No flow is permitted through the bottom or side walls. There is neither stress nor density flux at the side walls. At the bottom, there is no density flux and the viscous stress has a linear friction parameterization:

$$\left. \begin{array}{l} A_v \frac{\partial u}{\partial z} = ru \\[2mm] A_v \frac{\partial v}{\partial z} = rv \end{array} \right\} z = -h \qquad (2.6)$$

where $r=0.002$ m s^{-1}. This choice of r is discussed in section 2.4. On the upper surface there are no density fluxes and the stress is specified as:

$$\left. \begin{array}{l} A_v \frac{\partial u}{\partial z} = \frac{\tau_x^s(t)}{\rho_o} \\[2mm] A_v \frac{\partial v}{\partial z} = 0 \end{array} \right\} z = 0 \qquad (2.7)$$

$\tau_x^s(t)$ is discussed in reference to specific experiments. The boundary conditions at the entrance and exit of the channel are discussed below.

The diffusive terms, $\mathcal{D}_u$, $\mathcal{D}_v$ and $\mathcal{D}_\rho$ are broken up into horizontal and vertical components.

$$\begin{array}{l} \mathcal{D}_u = A_H \nabla^2 u + \mathcal{D}_{vert} \\[2mm] \mathcal{D}_v = A_H \nabla^2 v + \mathcal{D}_{vert} \\[2mm] \mathcal{D}_\rho = K_H \nabla^2 \rho + \mathcal{D}_{vert} \end{array}$$

Laplacian mixing is applied in the horizontal. For the momentum equations, the horizontal diffusion coefficient, A_H, is 300 m^2 s^{-1}. For the density equation, the horizontal diffusion coefficient, K_H, is 40 m^2 s^{-1}. The values of A_H and K_H are con-

siderably larger than values used in similar experiments such as Chapman and Lentz (1994), Yankovsky and Chapman (1997) and Chapman (2000). These experiments apply only a small barotropic inflow boundary condition. This study uses much larger barotropic inflows. The barotropic inflow generates offshore transport in the bottom Ekman layer. To conserve mass there must be a region of downwelling at the coastal wall and a region of upwelling at the offshore wall. A_H and K_H are chosen to be the smallest possible values that give stability[1] in these boundary layers. If the horizontal mixing is too small, the regions of vertical motion are poorly resolved resulting in alternating one grid cell wide bands of upwelling and downwelling. To eliminate these artificial features, the Laplacian mixing coefficients are increased.

The vertical mixing, $\mathcal{D}_{vert}$, uses the Mellor-Yamada 2.0 scheme (Mellor and Yamada (1982), Chapman 2000), implemented with an implicit time step. In some places in the model domain there is very little stratification and the Mellor-Yamada scheme produces very large values for the vertical diffusivity. The vertical diffusivity is limited to a maximum value of 0.02 m^2 s^{-1}. The justification for this is discussed in section 2.4. The implicit time step makes it difficult to diagnose the magnitude of the vertical mixing in the momentum equations. Additional vertical mixing occurs through convective adjustment wherever the density field is statically unstable, typically in the surface and bottom mixed layers. The convective adjustment scheme mixes density and not momentum.

The downstream boundary condition is a modified Orlanski condition described in Chapman(2000).

---

[1] If the diffusion is smaller, the downwelling at the coastal wall is replaced with alternating bands up upwelling and downwelling, each one grid cell wide. For $A_H = 50$ m^2 s^{-1}, the value in the cited papers, the bands of vertical motion extend about a quarter of a way into the domain before diminishing. Similar behavior is observed at the offshore wall. This suggests a numerical instability created by inadequate horizontal resolution of the wall boundary layers. By increasing the horizontal diffusion, the width of the boundary layers is increased and the model resolution becomes adequate.

2.3 Conceptual discussion of model physics

A conceptual sketch of the model dynamics is presented in this section, which will be validated later by actual model runs.

2.3.1 No wind stress and no barotropic inflow

The basic case of a buoyant plume with no forcing is discussed first. Chapman and Lentz (1994) show that a density front moves to a stable position and is trapped in one specific location by the behavior of the bottom boundary layer. There is a surface intensified jet and, on the shoreward side of the front, the jet's downstream motion drives an offshore transport in the bottom boundary layer. Because the jet is in geostrophic balance, the velocity shear is determined by the density difference across the front. Within the foot of the front there is a bottom intensified jet in the reverse direction created by the geostrophic shear associated with the front. The opposing jet drives a shoreward Ekman transport in the bottom boundary layer. At the shoreward edge of the front, there is convergence in the bottom boundary layer which drives an upwelling circulation from the bottom boundary layer upwards and offshore along the front. A number of different observational programs have observed this upward motion along the front, commonly called bottom boundary layer detachement. (Visbeck and Houghton (1998), Barth et al. (1998), Pickart (1999)). The process is summarized in figure 2-2.

The convergence in the bottom boundary layer is a stable trapping mechanism. Where the along shelf velocity, u, vanishes, the cross shelf velocity, v, does as well. Therefore, there is no cross shelf advection of density and the front remains stationary. Should the density difference across the front increase, the shear increases and the onshore bottom boundary layer transport increases. The up-slope transport dominates and the front moves shoreward. If the density difference across the front decreases, the down-slope transport dominates and the front moves offshore. In both
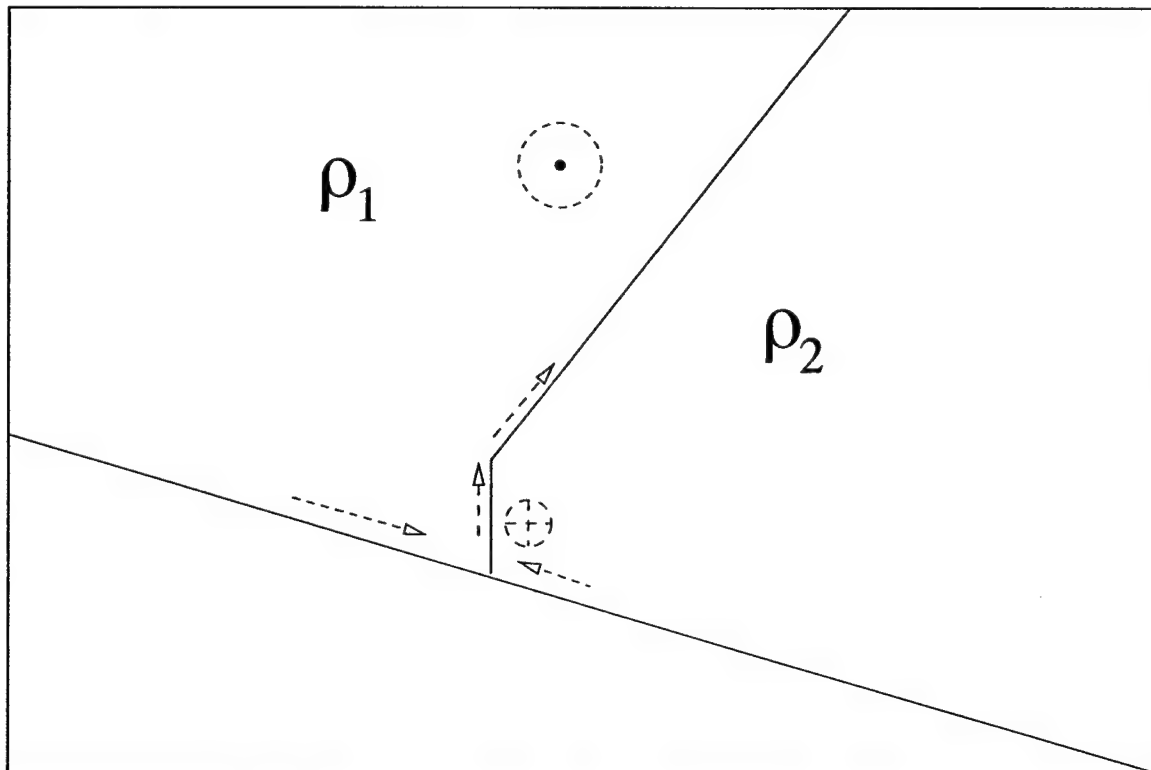
Figure 2-2: The behavior of the front when there is no barotropic background flow. A convergent bottom Ekman layer pumps water up and out of the bottom boundary layer, along the front.

cases a balance is achieved when the front reaches the correct depth, h_b, given by equation 2.8 (Yankovsky and Chapman, 1997).

$$h_b = \sqrt{\frac{2f_0 T}{g'}} \qquad (2.8)$$

where T is the transport of the front, and $g' = \frac{\Delta \rho}{\rho} g$ is the reduced gravity.

Chapman and Lentz (1994) use vertical mixing with a constant mixing coefficient. Chapman (2002) compares the results with a constant mixing coefficient to the results with a variable coefficient, using the Mellor-Yamada 2.0 scheme. He finds that the basic trapping mechanism, described above, is insensitive to the vertical mixing scheme, as is the location of the front, the pumping of water out of the bottom boundary layer and the surface intensified jet. However, the cross-frontal circulation and the front shape are significantly altered. In particular, the front with Mellor-Yamada 2.0 mixing is narrower than the front with constant vertical mixing. This leads to stronger density gradients and more vertical shear, causing the jet to be more strongly surface intensified. The bottom boundary layer is also stronger with Mellor-Yamada 2.0, which enhances the upwelling along the front. In addition, he observes that the cross shelf velocity in the bottom boundary layer is not steady within the foot of the front. Instead, there are bottom trapped waves with a period of a little over 1 day that travel along the front. The cross shelf and vertical velocity varies as a function of time as the waves pass. The downstream velocity does not reverse direction in the bottom layer but it does become very small. The results from this study are similar but because the horizontal mixing is stronger than is applied in Chapman (2002), the front in this study is wider. In the bottom boundary layer, Chapman (2002) finds that there is a balance between the cross shelf advection of density and the vertical diffusion of density at the shoreward side of the front. However, in this study, because the horizontal diffusion is so much stronger, the balance appears to be between the cross shelf advection of density and the horizontal diffusion of density when the along
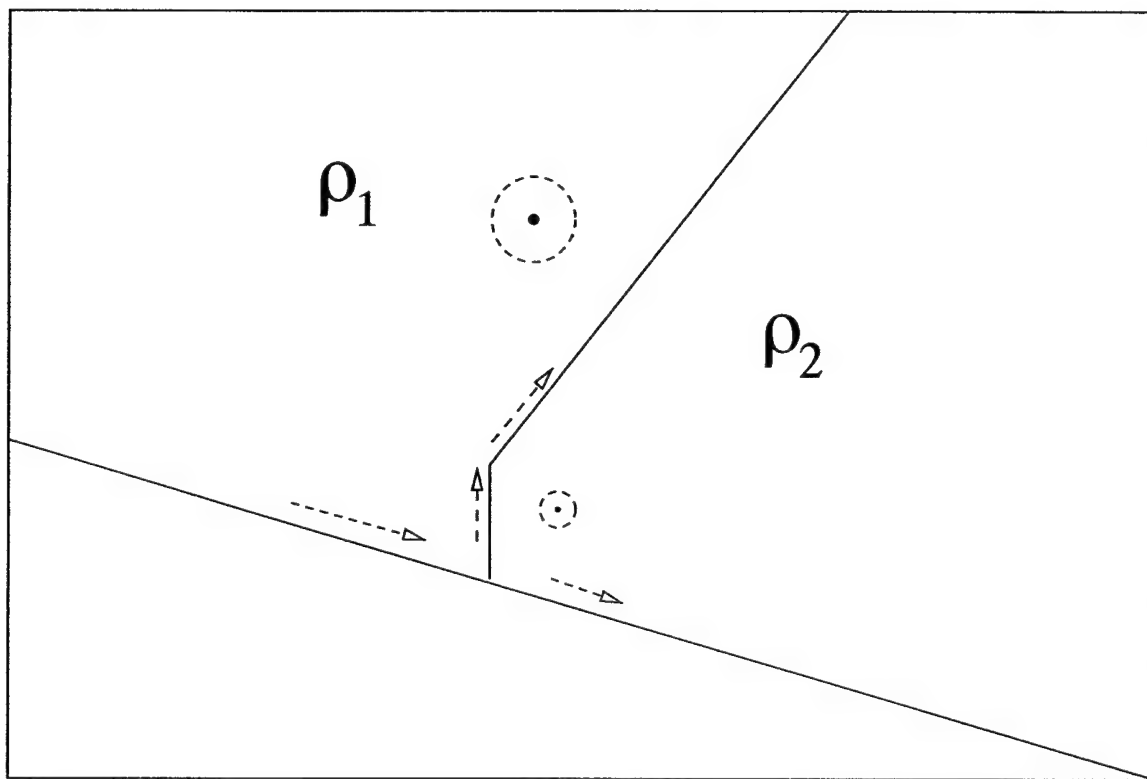
Figure 2-3: The front with Mellor-Yamada 2.0 mixing, based on the results of Chapman 2002. There is no reversal in the along shelf geostrophic velocity but it does approach 0. The cross shelf and vertical velocity at the bottom vary periodically, suggesting a wave trapped in the density gradient of the front. The front still traps at approximately the same place and there is still convergence at the base of the front, driving water upwards along the isopycnals.

shelf barotropic velocity is small. When there are large along shelf barotropic velocities, the vertical flux of density out of the bottom boundary layer becomes significant in the trapping of the front. The behavior of the system with Mellor-Yamada 2.0 mixing is summarized in figure 2-3.

2.3.2 Wind stress and no barotropic inflow

When wind is blowing in the same direction as the current, the model develops a surface Ekman layer which transports dense water shoreward in the surface boundary layer. Because this is convectively unstable, a thick surface mixed layer develops. The

shoreward transport leads to a region of coastal downwelling. The cross shelf mass flux in the surface boundary layer is balanced by an offshore flow in the bottom boundary layer. In section 2.4, it is shown that the wind stress will develop an along-channel barotropic current and this current generates the offshore bottom Ekman transport. Because the channel used in this study is prescribed on three walls (open only at the outflow boundary), the along shelf barotropic flow generated by the wind must be balanced by an upstream jet at the model's offshore boundary to conserve mass. A region of upstream transport also develops under the front, as it does in Chapman and Lentz (1994). In both places where there is upstream transport, there is shoreward Ekman transport along the bottom. The reverse jet under the front carries dense water up-slope and causes the mixed layer to detach from the bottom. The reversed jet along the offshore wall is a region of strong convergence and as water is drawn into it, the interior of the front is pulled offshore. A cartoon of the front with wind is shown in figure 2-4.

While the basic trapping mechanism is unaffected by the wind stress, the front is modified by wind stress in several ways: the surface of the front is advected significantly shoreward by Ekman transport, the mixed layer at the base of the front becomes detached from the bottom by the shoreward Ekman transport under the reversed jet and the rest of the front is pulled offshore by the mass convergence at the offshore wall.

The variability of the front and jet system is not studied in detail, however preliminary results suggest that for a steady wind, the frontal response is steady.

2.3.3 A barotropic inflow with no wind stress

The barotropic inflow is imposed as a spatially homogeneous velocity, at $x = 0$. However, as the flow moves along the channel, it does not remain spatially homogeneous. Csanady (1978) studied the adjustment of a barotropic flow over a sloping bottom. His results, as they apply to this problem, are summarized in figure 2-5.
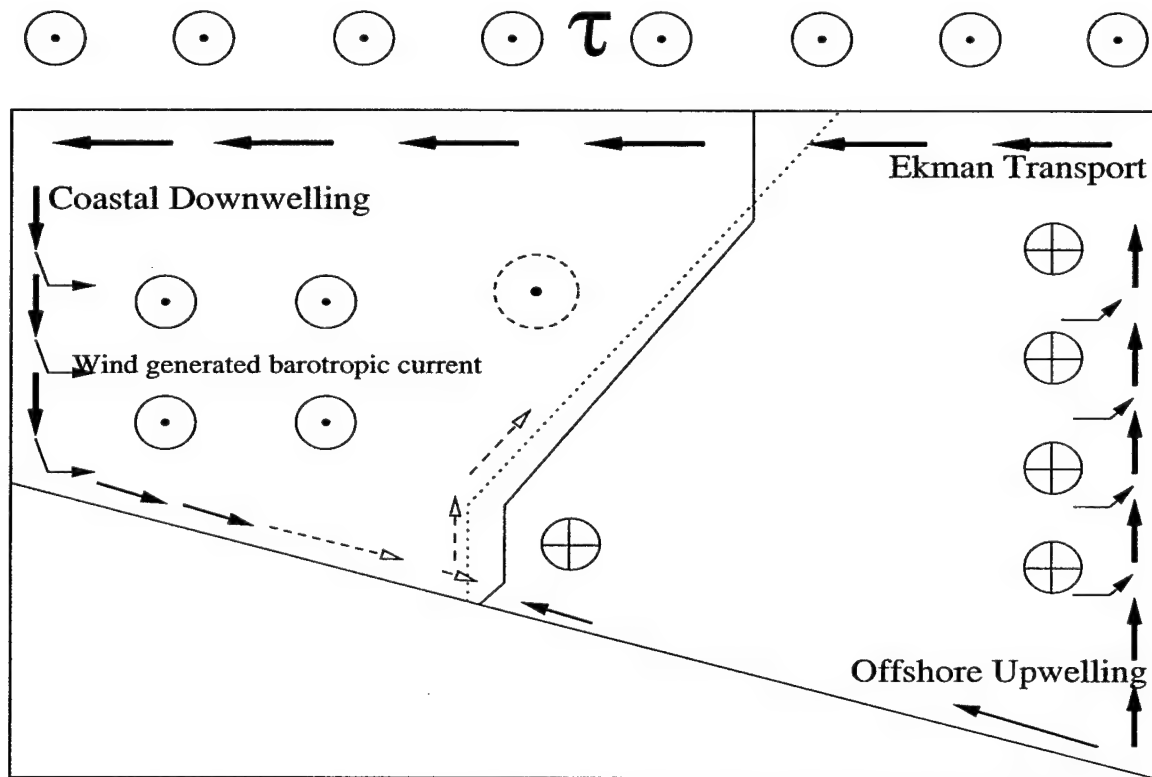
Figure 2-4: The behavior of the front when there is wind but no barotropic current. A surface Ekman layer develops which advects the surface water shoreward. The surface Ekman transport creates a surface mixed layer. Mass is conserved in the cross shelf direction by an offshore return flow in the bottom Ekman layer. The bottom Ekman layer is generated by the along shore barotropic transport, driven by the wind. Mass is conserved in the along shelf direction by the upstream jet along the offshore wall and under the front. The dotted line indicates the original position of the front and the solid line indicates the position of the front after the wind has altered it. This sketch assumes that MY2.0 mixing is used.
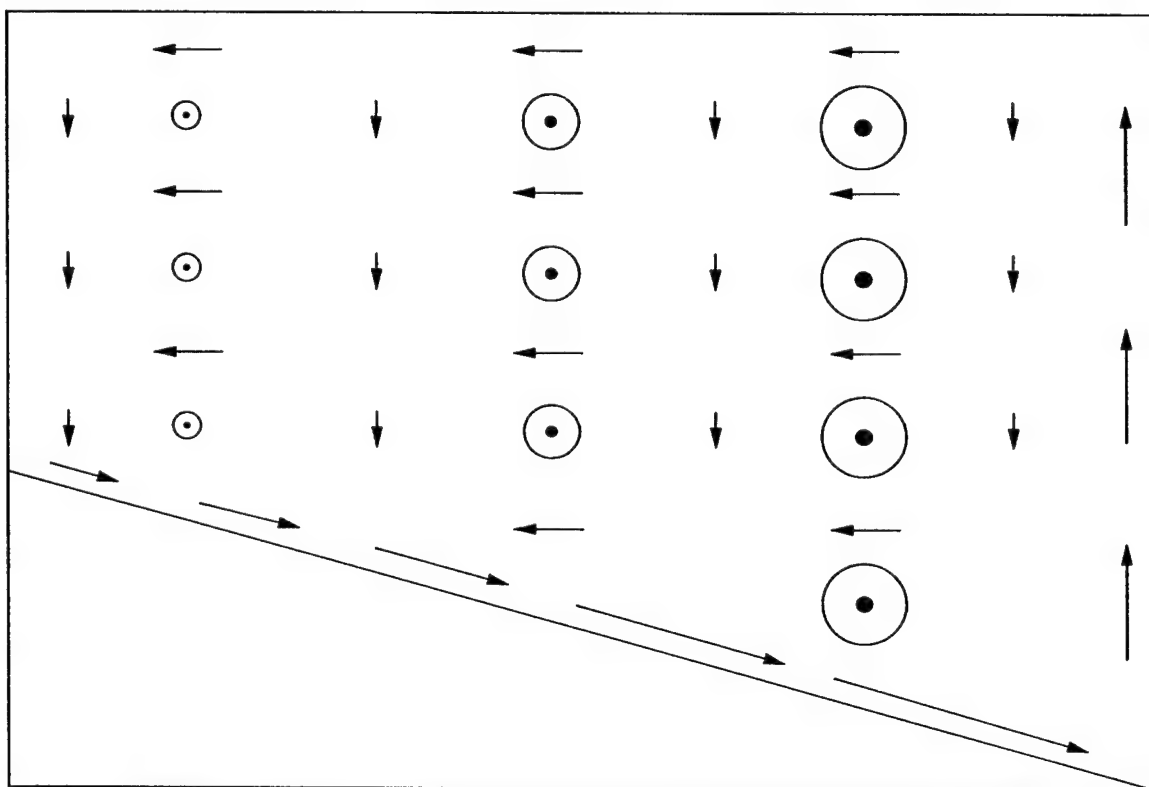
Figure 2-5: The adjustment of a barotropic flow over a sloping bottom. The along shelf flow is stronger in deeper water resulting in a divergent bottom boundary layer. To balance the mass, the interior has a small return flow.

Across the shelf, from shallow water to deep water, there is a continuous, monotonic increase in u. This occurs because vorticity is put into the water column through bottom friction in the bottom boundary layer. The increase in vorticity requires the water column to move offshore. At any single location, the cross shelf transport of the bottom Ekman layer is proportional to the along shelf water speed directly above it. The offshore transport in the bottom Ekman layer is everywhere divergent: in shallow water the transport is less than it is further offshore. In the cross shelf direction, mass moves down-slope with $v > 0$ in the bottom Ekman layer. It is balanced with a return flow, with $v < 0$, in the interior.

When a barotropic current is superimposed on the front, it has two effects on the frontal system. First, the bottom Ekman layer carries less dense water under more dense water, causing the front to develop a bottom mixed layer thicker than the one developed by the adjustment process alone. Second, the return flow from the bottom Ekman layer, pushes the front shoreward. This causes the front to move into shallower water. The dynamics of the front and barotropic inflow are summarized in figure 2-6.

2.3.4 A barotropic inflow and wind stress

As discussed above, when there is wind stress, the base of the front will tend to shift offshore and when there is a barotropic inflow, the base of the front will tend to shift shoreward. If the barotropic velocity is held constant and the wind stress is increased, the front should move offshore into deeper water; if the wind stress is held constant and the barotropic velocity is increased, the front should move shoreward into shallower water. Therefore the change in position of the front will be less if both are increased simultaneously.
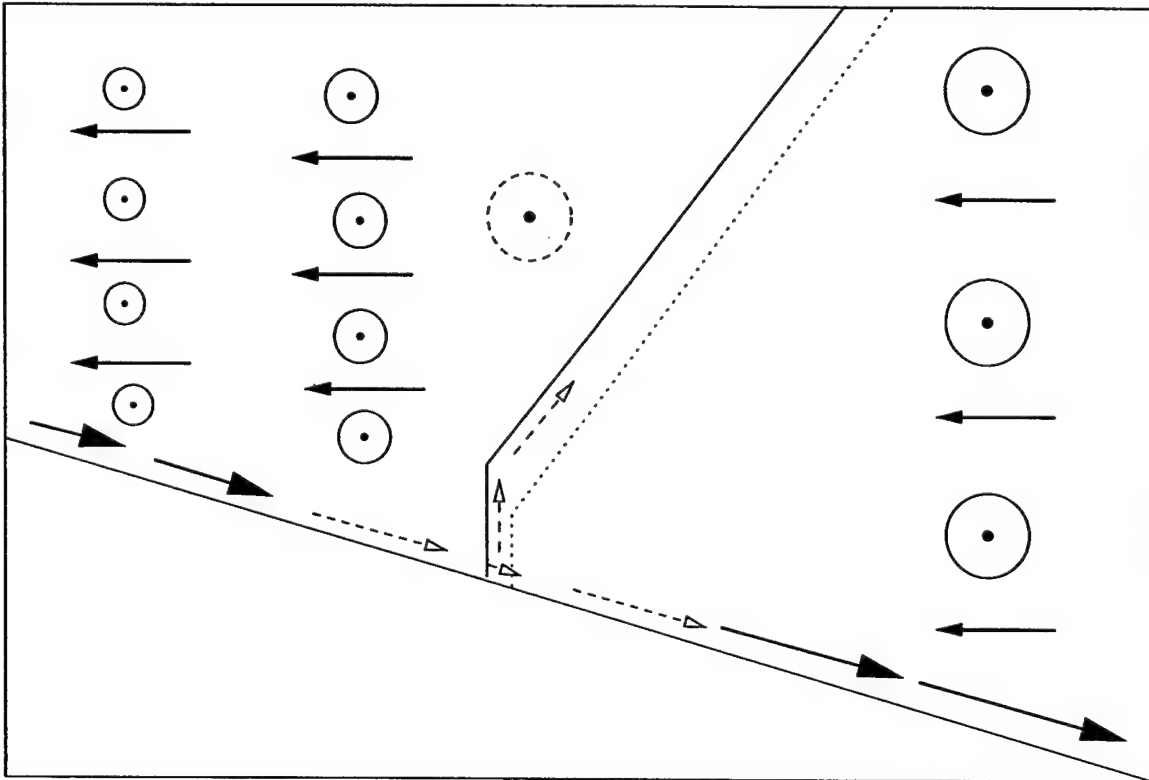
Figure 2-6: The behavior of a front when it interacts with a barotropic inflow. The bottom Ekman transport enlarges the bottom mixed layer. Mass is conserved in the cross shelf direction by an on-shore return flow in the interior which pushes the front shoreward. The dotted line indicates the original position of the front and the solid line indicates the position of the front after the barotropic inflow has altered it. The dotted arrows are transport associated with the front and the solid arrows are transport associated with the barotropic current.

2.4 The inflow boundary condition

A large number of experiments with varying wind stress and barotropic inflow were conducted. It is argued below that there is a certain barotropic current that is expected for a known wind stress, however in this study, most of the model runs were conducted with a barotropic inflow which is independent of the wind stress. If the appropriate mass flux is not provided at the inflow boundary, the model attempts to spin up the barotropic velocity. In this section, the relationship between the imposed wind stress and the related barotropic current is developed. This barotropic velocity is used as the modified boundary condition imposed at $x = 0$, for some experiments and is used to determine appropriate values for the bottom drag coefficient, r, and the maximum vertical mixing, A_v.

To do this calculation, first the form of the bottom Ekman layer with partial slip boundary conditions is derived. The Ekman layer solution is used to find an expression for the magnitude of the barotropic current, depending on the magnitude of the wind. Finally, the choice of the bottom drag coefficient and the maximum vertical diffusivity, used in all experiments, is discussed.

2.4.1 The Bottom Ekman Layer

The standard Ekman layer derivation is modified to allow for a slip-type bottom boundary condition. Because this study uses a bottom drag coefficient, r, some slip is allowed at the bottom boundary. Assuming the boundary layer is linear and steady, the equations are:

$$-f_0 v = -\frac{1}{\rho_0}\frac{\partial p}{\partial x} + A_v \frac{\partial^2 u}{\partial z^2} \tag{2.9}$$

$$f_0 u = -\frac{1}{\rho_0}\frac{\partial p}{\partial y} + A_v \frac{\partial^2 v}{\partial z^2} \tag{2.10}$$

where x is along-channel and y is cross-channel. The boundary conditions are

$$\left. \begin{array}{l} A_v \frac{\partial u}{\partial z} = ru \\[2mm] A_v \frac{\partial v}{\partial z} = rv \end{array} \right\} z = 0$$

and

$$\left. \begin{array}{l} u = u_I \\[2mm] v = v_I \end{array} \right\} z \to \infty$$

where u_I and v_I represent the interior flow of the fluid. The vertical coordinate, z, is 0 on the bottom of the ocean and increases upwards. (The numerical model puts the origin at the surface of the ocean. In this section, it is chosen to be at the bottom of the ocean so the equations are in a simpler format.) Assuming the interior is in geostrophic balance

$$\begin{array}{l} -f_0 v_I = -\frac{1}{\rho_0} \frac{\partial p}{\partial x} \\[2mm] f_0 u_I = -\frac{1}{\rho_0} \frac{\partial p}{\partial y} \end{array}$$

and equations 2.9 and 2.10 become

$$-f_0 v = -f_0 v_I + A_v \frac{\partial^2 u}{\partial z^2} \tag{2.11}$$

$$f_0 u = f_0 u_I + A_v \frac{\partial^2 v}{\partial z^2} \tag{2.12}$$

Multiplying 2.12 by i and adding it to 2.11,

$$i f_0 q = i f_0 q_I + A_v \frac{\partial^2 q}{\partial z^2} \tag{2.13}$$

where

$$q = u + iv$$

and

$$q_I = u_I + iv_I$$

Rearranging equation 2.13

$$\frac{\partial^2 q}{\partial z^2} - \frac{if_0}{A_v}q = -\frac{if_0}{A_v}q_I \tag{2.14}$$

The boundary conditions become

$$A_v\frac{\partial q}{\partial z} = rq \quad z = 0$$

$$q = q_I \quad z \to \infty$$

Equation 2.14 has the solution

$$q = Ae^{-(1+i)\frac{z}{\delta}} + Be^{(1+i)\frac{z}{\delta}} + q_I \tag{2.15}$$

the Ekman layer thickness, δ, is defined as $\sqrt{\frac{2A_v}{f_0}}$. The boundary condition as $z \to \infty$ requires the solution remains bounded: $B = 0$. The boundary condition at the bottom determines A. The solution for q is

$$q = q_I(1 - (\alpha_r + i\alpha_i)e^{-(1+i)\frac{z}{\delta}}) \tag{2.16}$$

where α_r and α_i are dimensionless parameters of magnitude

$$\begin{aligned} \alpha_r &= \frac{r\delta(r\delta + A_v)}{(r\delta + A_v)^2 + A_v^2} \\ \alpha_i &= -\frac{A_v r\delta}{(r\delta + A_v)^2 + A_v^2} \end{aligned} \tag{2.17}$$

This solution appears in the appendix of Gawarkiewicz and Chapman (1995), in a somewhat different form. The bottom stress term, r, and the vertical mixing, A_v, play significant roles in the partial slip case.

The familiar no-slip solution is recovered by letting $r \to \infty$. Then $\alpha_r \to 1$, $\alpha_i \to 0$ and q reduces to

$$q = q_I(1 - e^{-(1+i)\frac{z}{\delta}})$$

63

The components of the velocity, u and v, are obtained from q as

$$
\begin{aligned}
u &= \mathrm{Real}(q) \\
v &= \mathrm{Imag}(q)
\end{aligned}
\tag{2.18}
$$

Figure 2-7 shows the solution in the Ekman layer for $u_I = 0.1$ m/s, $v_I = 0$ m/s, $r = 0.002$ m/s and $A_v = 0.02$ m^2 s^{-1}. The no-slip results are also plotted. The bottom boundary condition allows a flow of a few cm/s at $z = 0$. It also shifts the locations of the maxima downward.

2.4.2 The transport driven by along-channel wind

In the simple case of a two dimensional (depth and cross-channel position), homogeneous fluid, an analytical solution for the behavior of the fluid under uniform along-channel wind is found. (D. Chapman, class notes. 4/3/97. Based on notes from S. Lentz. Also presented in Dever (1997).)

The following assumptions are made.

1. The flow is two dimensional. It varies in the vertical (z) direction and the cross-channel (y) direction, but not in the along-channel (x) direction. $\frac{\partial}{\partial x} \to 0$

2. There is no cross-channel surface stress. $\tau_y^s = 0$.

3. The along-channel surface stress is homogeneous. $\frac{\partial \tau_x^s}{\partial y} = 0$.

4. The Rossby number is small; nonlinear advection terms are neglected.

5. Deformation of the surface, η, is small compared to the water depth, H.

6. The barotropic deformation radius is much larger than the horizontal scale of the motion. When applied to the continuity equation, this implies $\frac{\partial \eta}{\partial t} < \frac{\partial V}{\partial y}$ where V is the transport.
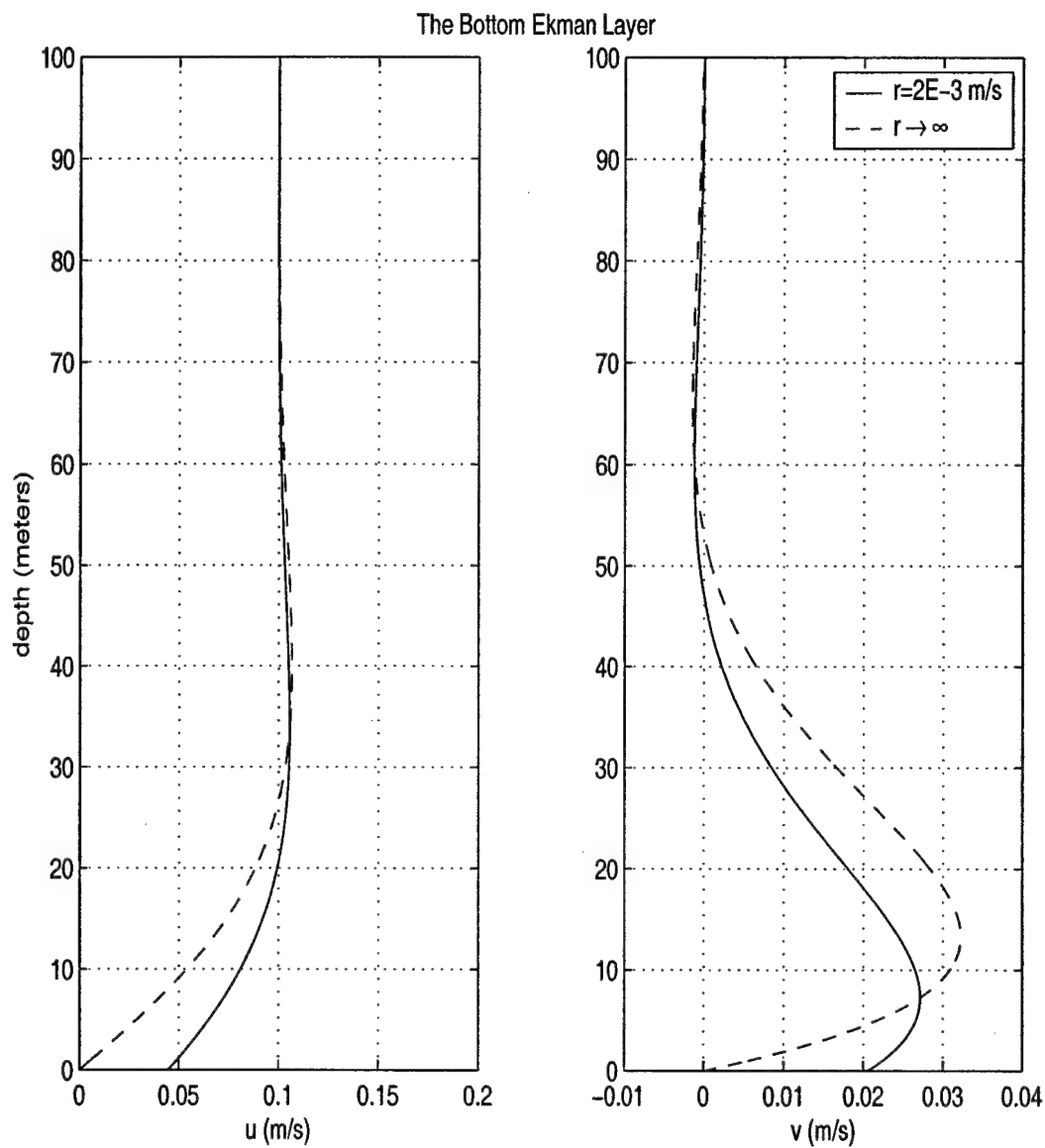
Figure 2-7: The structure of the bottom Ekman layer with $u_I = 0.1$ m/s and $A_v = 0.02$ m²/s. (a) The along shelf velocity, u. (b) The cross shelf velocity, v. The solid line is the solution with a slip type boundary condition. The dashed line is the no-slip solution.

Assumptions 2 and 3 are clearly simplifications of the more complex wind field found in the actual ocean. Further study is needed to address the complications of the real wind field. Assumption 4 requires a brief discussion. Because the flow examined in this case is two-dimensional, the downstream advection of momentum is neglected. In the cross stream direction, the wind stress is homogeneous which means there is no variation in velocity in the cross shelf direction. If the velocity is constant in the cross shelf direction, there is no cross shelf advection of momentum and assumption 4 is reasonable. Furthermore, the predicted velocities given in equation 2.33, yield Rossby numbers of about 0.1 or less, if the length scale is chosen to be the baroclinic deformation radius, suggesting that the nonlinear terms are negligible.

The depth integrated momentum and continuity equations, written in transport form reduce to:

$$\frac{\partial U}{\partial t} - f_0 V = \frac{1}{\rho_o}(\tau_x^s - \tau_x^b) \tag{2.19}$$

$$\frac{\partial V}{\partial t} + f_0 U = -gH\frac{\partial \eta}{\partial y} - \frac{\tau_y^b}{\rho_o} \tag{2.20}$$

$$\frac{\partial (V)}{\partial y} = 0 \tag{2.21}$$

where (U, V) are the depth integrated transports in the along- and cross-shelf directions respectively, H is the fluid depth, τ_x^b is the along-channel surface stress, τ_x^b is the along-channel bottom stress, τ_y^b is the cross-channel bottom stress and $-gH\frac{\partial \eta}{\partial y}$ is the cross-channel pressure gradient.

Initially it is assumed the flow is steady and the time derivatives in equations 2.19 and 2.20 are neglected. The steady state solution of equations 2.19, 2.20 and 2.21 is found.

Integrating equation 2.21 once

$$V = C$$

where C is some constant in y, the cross-channel direction. Because no flow is allowed

through the walls, $V = C = 0$. V refers to the net cross shelf transport integrated over the entire water column. Depth dependent flows, such as the Ekman layers, may have cross shelf transport.

The transports are expanded as a sum of three terms

$$
\begin{aligned}
U &= U_S + U_I + U_B \\
V &= V_S + V_I + V_B &= 0
\end{aligned}
\tag{2.22}
$$

where U_S and V_S represent the transport in the surface Ekman layer, U_I and V_I represent the interior geostrophic transport and U_B and V_B represent the transport in the bottom Ekman layer. Substituting 2.22 into the steady state version of equations 2.19 and 2.20

$$
-f_0 V_S - f_0 V_I - f_0 V_B = \frac{1}{\rho_o}(\tau_x^s - \tau_x^b) = 0
\tag{2.23}
$$

$$
f_0 U_S + f_0 U_I + f_0 U_B = -gH\frac{\partial \eta}{\partial y} - \frac{\tau_y^b}{\rho_o}
\tag{2.24}
$$

The Ekman transport relationships for each boundary layer and their substitution into 2.23 and 2.24 give

$$
\begin{aligned}
f_0 U_S &= 0 & -f_0 V_S &= \frac{\tau_x^s}{\rho_o} \\
f_0 U_I &= -gH\frac{\partial \eta}{\partial y} & -f_0 V_I &= 0 \\
f_0 U_B &= -\frac{\tau_y^b}{\rho_o} & -f_0 V_B &= -\frac{\tau_x^b}{\rho_o}
\end{aligned}
\tag{2.25}
$$

U_S, V_S, U_B and V_B are integrated transports in the surface and bottom Ekman layers. In equation 2.25 the top line and bottom line are the Ekman balances for each boundary layer. The interior geostrophic transports are U_I and V_I. The middle line of 2.25 expresses the geostrophic balance.

From 2.22, $V_S + V_I + V_B = 0$. Applying this to 2.25, $V_S = -V_B$. In steady state, the Ekman transport in the surface and bottom boundary layers must balance. If the transports match, the stresses must also be equal and $\tau_x^s = \tau_x^b$.

Newtonian friction relates frictional stress to the vertical shear in the fluid. In the bottom Ekman layer,

$$\left.\begin{array}{rll} \frac{\tau_x^b}{\rho_o} & = A_v \frac{\partial u}{\partial z} & = \frac{\delta^2 f_0}{2}\frac{\partial u}{\partial z} \\[2mm] \frac{\tau_y^b}{\rho_o} & = A_v \frac{\partial v}{\partial z} & = \frac{\delta^2 f_0}{2}\frac{\partial v}{\partial z} \end{array}\right\} z = 0 \tag{2.26}$$

where $\delta = \sqrt{\frac{2A_v}{f_0}}$. Lower case u and v represent the velocity of the fluid. The z derivative of equation 2.18 gives expressions for $\frac{\partial u}{\partial z}$ and $\frac{\partial v}{\partial z}$. Equation 2.26 becomes

$$\left.\begin{array}{rl} \frac{\tau_x^b}{\rho_o} & = \frac{\delta^2 f_0}{2}\text{Real}\frac{\partial q}{\partial z} \\[2mm] \frac{\tau_y^b}{\rho_o} & = \frac{\delta^2 f_0}{2}\text{Imag}\frac{\partial q}{\partial z} \end{array}\right\} z = 0 \tag{2.27}$$

where the derivative of equation 2.16 gives

$$\left.\frac{\partial q}{\partial z}\right|_{z=0} = \frac{q_I(\alpha_r + i\alpha_i)(1+i)}{\delta} \tag{2.28}$$

In steady state $v_I = 0$ and $q_I = u_I$. Equation 2.28 is multiplied by H and substituting $U_I = Hu_I$, equation 2.27 becomes

$$\frac{\tau_x^b}{\rho_o} = \frac{\delta f_0}{2H}U_I(\alpha_r - \alpha_i) \tag{2.29}$$

$$\frac{\tau_y^b}{\rho_o} = \frac{\delta f_0}{2H}U_I(\alpha_r + \alpha_i) \tag{2.30}$$

where the dimensionless variables α_r and α_i are defined in equation 2.17. Equation 2.29 is rearranged for U_I

$$\begin{aligned} U_I & = \frac{\tau_x^b}{\rho_o f_0}\frac{2H}{\delta}\frac{1}{\alpha_r - \alpha_i} \\[2mm] & = \frac{\tau_x^s}{\rho_o f_0}\frac{1}{\epsilon}\frac{1}{\alpha_r - \alpha_i} \end{aligned} \tag{2.31}$$

because $\tau_x^b = \tau_x^s$. The aspect ratio, ϵ, is $\frac{\delta}{2H}$. Equation 2.30 is combined with 2.25 and rearranged for U_B:

$$\begin{aligned} U_B & = -\frac{\tau_y^b}{\rho_o f_0} \\[2mm] & = -\frac{\delta}{2H}U_I(\alpha_r + \alpha_i) \\[2mm] & = -\frac{\tau_x^s}{\rho_o f_0}\frac{\alpha_r + \alpha_i}{\alpha_r - \alpha_i} \end{aligned} \tag{2.32}$$

Summarizing, the steady state solution is

$$
\begin{aligned}
V_S &= -\frac{\tau_x^s}{\rho_o f_0} & U_S &= 0 \\
V_I &= 0 & U_I &= -V_S \frac{1}{\epsilon(\alpha_r - \alpha_i)} \\
V_B &= -V_S & U_B &= V_S \frac{\alpha_r + \alpha_i}{\alpha_r - \alpha_i}
\end{aligned}
\tag{2.33}
$$

This derivation assumes a steady state and provides no insight on how long it takes for the system to reach this state. The Ekman layers spin up with an e-folding time scale of $\frac{1}{f_0}$. The interior adjusts more slowly. The question is: how much more slowly?

When the wind first "turns on", shoreward transport develops in the surface Ekman layer. (For the purpose of this discussion, the Ekman layer spin up is assumed to happen instantaneously.) Mass is balanced by an offshore flow in the interior. Over time, the downstream interior flow develops and generates the bottom Ekman layer. Once U_I has reached equilibrium, the shoreward transport of the surface Ekman layer is balanced by the offshore transport in the bottom Ekman layer. In the following derivation, the interior velocity spin up time scale is estimated from the x momentum equation and it assumes the cross shelf velocity is steady. A more accurate estimate could be obtained by considering the fully coupled equations.

Substituting equation 2.22 into equation 2.19

$$
\frac{\partial}{\partial t}(U_S + U_I + U_B) - f_0(V_S + V_I + V_B) = \frac{1}{\rho_o}(\tau_x^s - \tau_x^b)
\tag{2.34}
$$

In the cross shelf direction, the mass balance during the spin-up must be between the shoreward surface Ekman transport and the return flow in the interior. Because there is no along-shelf barotropic flow yet, there is no bottom Ekman transport so

$$
\begin{aligned}
0 &= V_S + V_I + V_B \\
&= V_S + V_I
\end{aligned}
$$

69

Therefore, the cross shelf interior transport can be written in terms of the wind stress:

$$
\begin{aligned}
V_I &= -V_S \\
&= \frac{\tau_x^s}{\rho_o f_0}
\end{aligned}
$$

The real part of 2.28, integrated over the Ekman layer, gives an expression for the bottom stress, τ_x^b, in terms of the interior along shelf and cross shelf transports.

$$
\frac{\tau_x^b}{\rho_o} = \frac{\delta}{2} \frac{f_0}{H} \left[U_I \left(\alpha_r - \alpha_i \right) - V_I \left(\alpha_r + \alpha_i \right) \right]
$$

If the Ekman layers spin up faster than the interior, they reach steady state while the interior is still adjusting. Once the Ekman layers have spun up, $\frac{\partial}{\partial t} \left(U_S, U_B \right) \ll \frac{\partial}{\partial t} U_I$, and

$$
\frac{\partial}{\partial t} \left(U_S + U_I + U_B \right) \approx \frac{\partial}{\partial t} \left(U_I \right)
$$

The expression for τ_x^b is substituted into 2.34 and a first order differential equation for U_I is found.

$$
\frac{\partial U_I}{\partial t} + f_0 \epsilon \left(\alpha_r - \alpha_i \right) U_I = \frac{\tau_x^s}{\rho_o} \left[1 + \epsilon \left(\alpha_r + \alpha_i \right) \right] \tag{2.35}
$$

The aspect ratio, $\epsilon = \frac{\delta}{2H}$, is used in this expression.

Equation 2.35 has the solution

$$
U_I = A e^{-\frac{t}{T}} + \frac{\tau_x^s}{\rho_o f_0} \frac{1 + \epsilon \left(\alpha_r + \alpha_i \right)}{\epsilon \left(\alpha_r - \alpha_i \right)}
$$

where the time scale, T is

$$
\frac{1}{f_0 \epsilon \left(\alpha_r - \alpha_i \right)} \tag{2.36}
$$
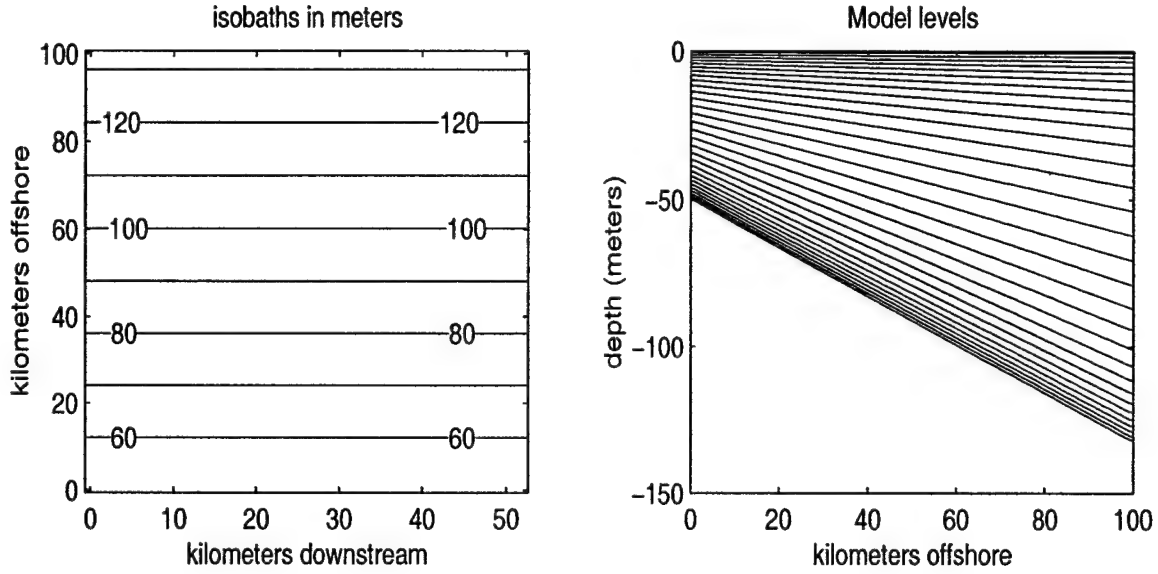
Figure 2-8: The model configuration for the reduced domain, periodic channel model used to test the Ekman layer dynamics. (a) The model bathymetry. (b) A slice through the channel showing the model levels.

and A is a constant of integration. If $U_I = 0$ at $t = \frac{1}{f_0}$, then the general solution is[2]

$$
\begin{aligned}
U_I &= \frac{\tau_x^s}{\rho_o f_0} \frac{1+\epsilon(\alpha_r+\alpha_i)}{\epsilon(\alpha_r-\alpha_i)} \left(1 - e^{\frac{1}{T}\left[\frac{1}{f_0}-t\right]}\right) \\
&= -V_S \frac{1+\epsilon(\alpha_r+\alpha_i)}{\epsilon(\alpha_r-\alpha_i)} \left(1 - e^{\frac{1}{T}\left[\frac{1}{f_0}-t\right]}\right)
\end{aligned}
\tag{2.37}
$$

In the limit $t \to \infty$, equation 2.37 does not quite reduce to the steady solution for U_I stated in equation 2.33 because in that limit, the cross shelf mass transport in the surface Ekman layer is balanced by the mass transport in the bottom Ekman layer, not the interior. However, because $1 + \epsilon(\alpha_r + \alpha_i) \approx 1$ for the standard values used in this text, the solution is very close to the steady solution in 2.33.

Tests of this solution are conducted in a simplified model. A periodic channel with a sloping bottom (figure 2-8) is constructed. The model domain is smaller than the full model but it has the same resolution and horizontal mixing coefficients. The

---

[2]Admittedly this is not the ideal initial condition as the internal flow will have spun up slightly by $t = \frac{1}{f_0}$.
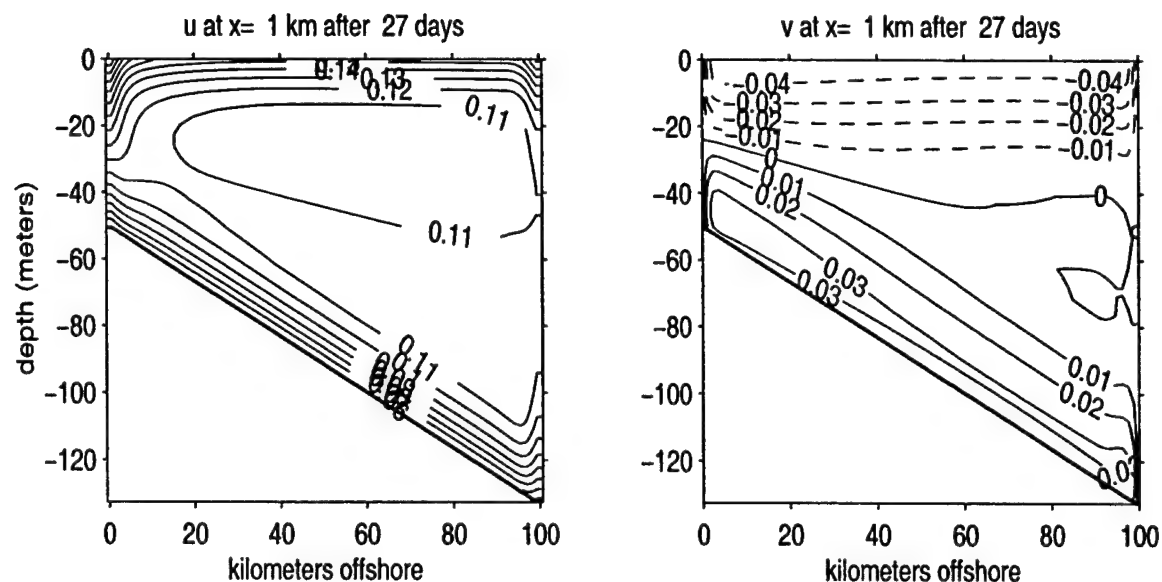
Figure 2-9: The velocity structure under the influence of wind in the periodic channel. (a) along-channel velocity (b) cross-channel velocity. Negative contours are dashed.

channel is filled with water of a single density and a constant wind stress is imposed. Many model runs are conducted with different values of r and the maximum allowed A_v. Because this is a homogeneous model, Richardson number dependent mixing schemes do not affect the solution and the vertical mixing in the reduced model is the maximum allowed value of A_v.[3] Each run is integrated until the velocity of the interior reaches a steady value.

A cross-section of a typical run is shown in figure 2-9. The along-channel direction has surface and bottom Ekman layers. The structure in the interior is mostly depth independent. The cross-channel direction has surface and bottom Ekman layers. The interior flow is small.

A distinct depth varying boundary layer structure develops along the channel walls. A jet approximately 10 km wide develops on the coastal wall at the surface and a region of slower flow of approximately the same width develops on the offshore

---

[3]A variety of mixing schemes were tested including Mellor-Yamada 2.0 with an implicit time step (used in the complete model) and simple diffusive mixing. The results are independent on the mixing scheme.

wall. At depth, there is a region of slower flow at the coastal wall and a jet off shore. The boundary layers occur in regions of strong Ekman convergence (coastal wall) and divergence (offshore wall) because flow is not allowed through the walls. The horizontal structure is not accounted for in the simple analytical model.

Figure 2-10 shows a typical vertical profile away from the wall boundary layers. The theoretical solution is plotted over it. The theoretical solution for the bottom Ekman layer is calculated from equation 2.18. An appropriate value for q_I is found by dividing equation 2.33 by H.

$$
\begin{aligned}
q_I &= u_I + iv_I \\
&= \frac{U_I}{H} + i\frac{V_I}{H} \\
&= \frac{\tau_x^s}{\rho_o f_0}\frac{2}{\delta}\frac{1}{\alpha_r - \alpha i} + 0
\end{aligned}
\tag{2.38}
$$

The theoretical solution for the surface Ekman layer is found in the usual way: solving equation 2.13 and matching the surface stress at the surface boundary condition and matching q_I at depth. The two solutions are matched in the middle of the model domain to the interior along-shelf velocity, u. (For the choice of parameters in this example, the top and bottom boundary layers do not come into contact.)

The dependence on r and the maximum allowed A_v are tested by varying them widely. In all runs, the surface wind stress is held constant at 0.1 N m^{-2}. This wind stress is comparable to the annual mean wind stress found over the East Greenland Current (Legutke, 1991). Figure 2-11 shows the theoretical u_I with numerical model values plotted over it. The model values for u_i are taken from the center of the domain after 27 days of wind. In 2-11a, r is held constant at $2{\cdot}10^{-3}$ m/s. In 2-11b, A_v is held constant at 0.02 m^2 s^{-1} There is good agreement between the theoretical values and numerical model results.

The adjustment of the model is examined in figure 2-12. In all cases, the model adjusts slower than is predicted by equation 2.37, suggesting that the time scale T is smaller than it should be. From the model runs, the adjustment time scale is two or
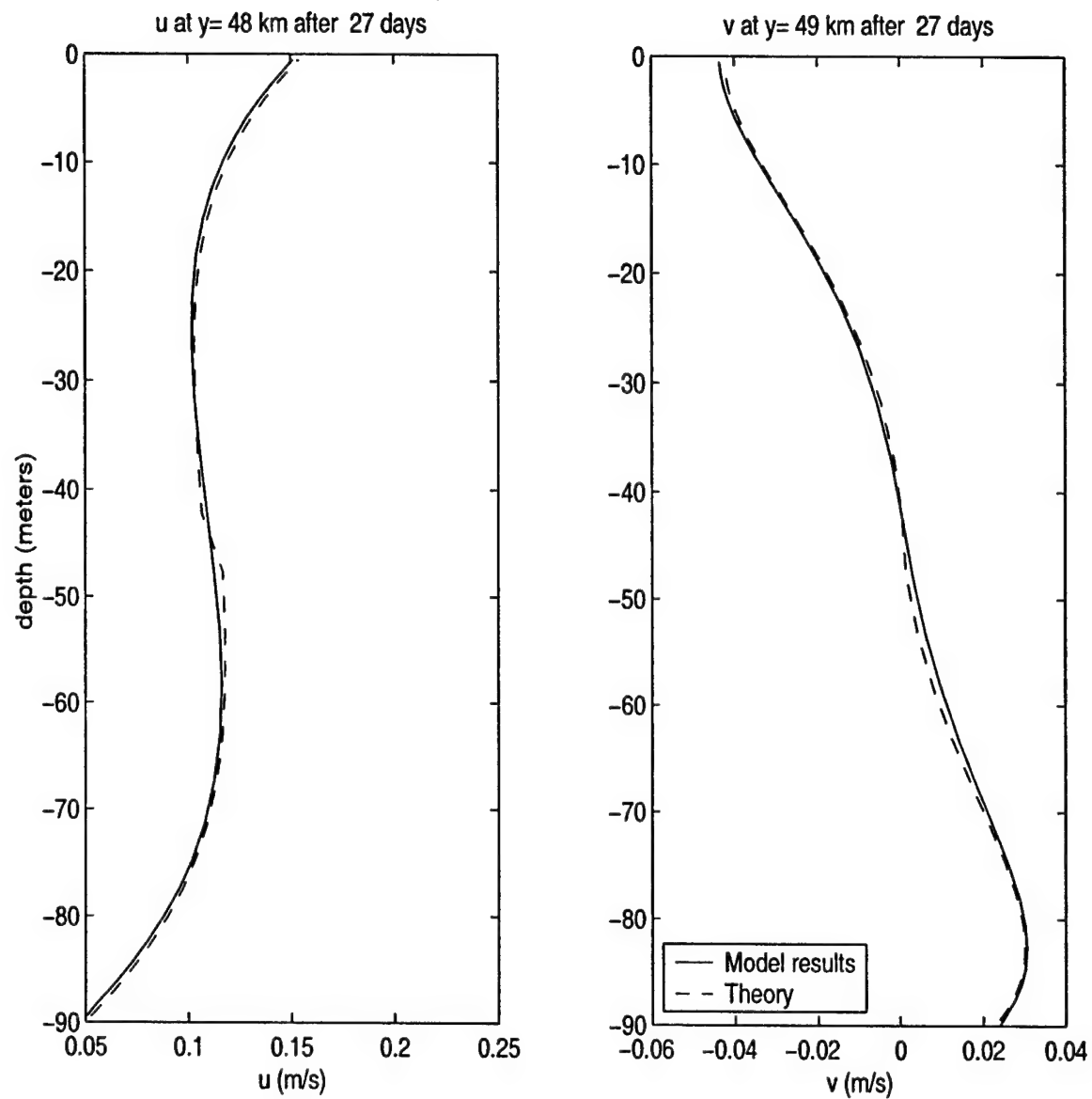
Figure 2-10: A vertical section through the center of figure 2-9. (a) u (b) v. The model results are plotted as solid lines and the theoretical solution for the bottom boundary layer is dashed.
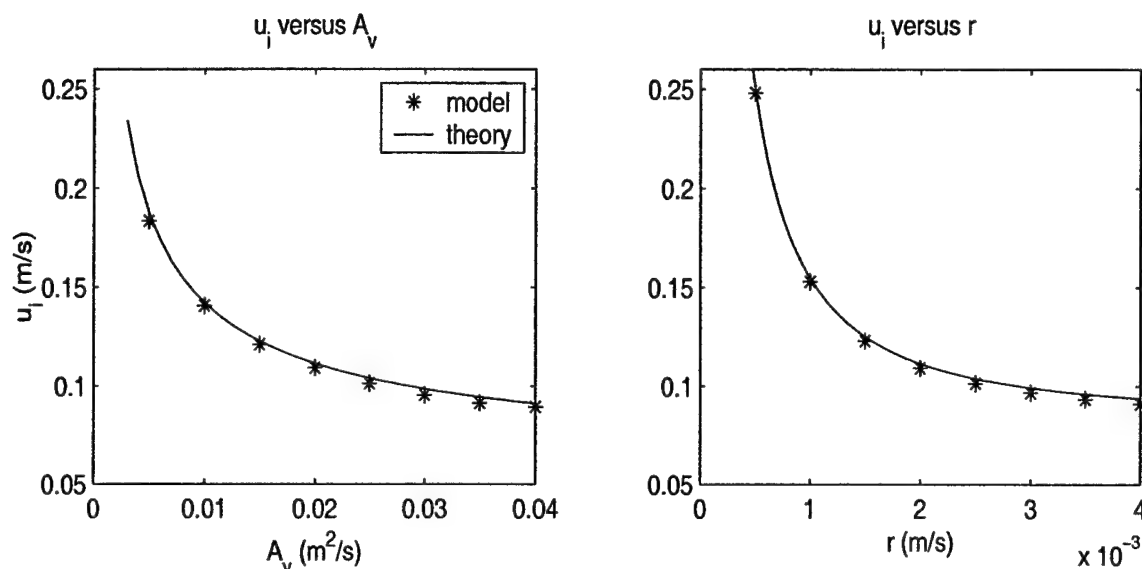
Figure 2-11: The dependence of u_i on (a) the maximum allowed A_v and (b) r. Equation 2.38 is shown as a solid line. Individual model runs are shown as asterisks.

three times longer than is estimated in equation 2.36. That may be because T is not much longer than $\frac{1}{f_0}$, as was assumed in the derivation, and the Ekman layers and interior flow adjust simultaneously.

2.4.3   The inflow boundary condition with wind forcing

An analytical solution to a two dimensional, homogeneous channel under along-channel wind stress was developed in the previous section. The solution depends on the value of the wind stress, τ_x^s, the strength of the vertical mixing, A_v, and linear friction parameter, r.

In the full model, τ_x^s is chosen by examining weather station data and compiled climatologies. Figure 2-13a is the daily average wind speed from NOAA NCDC Weather Station BGDH located 12 m above sea level on the eastern coast of Greenland at 76.76° N by 18.66° W. There are large variations in the wind speed, especially in the winter months. The short time scale events are storms crossing the Norwegian sea (not considered here). The lower panel (figure 2-13b) shows monthly mean wind
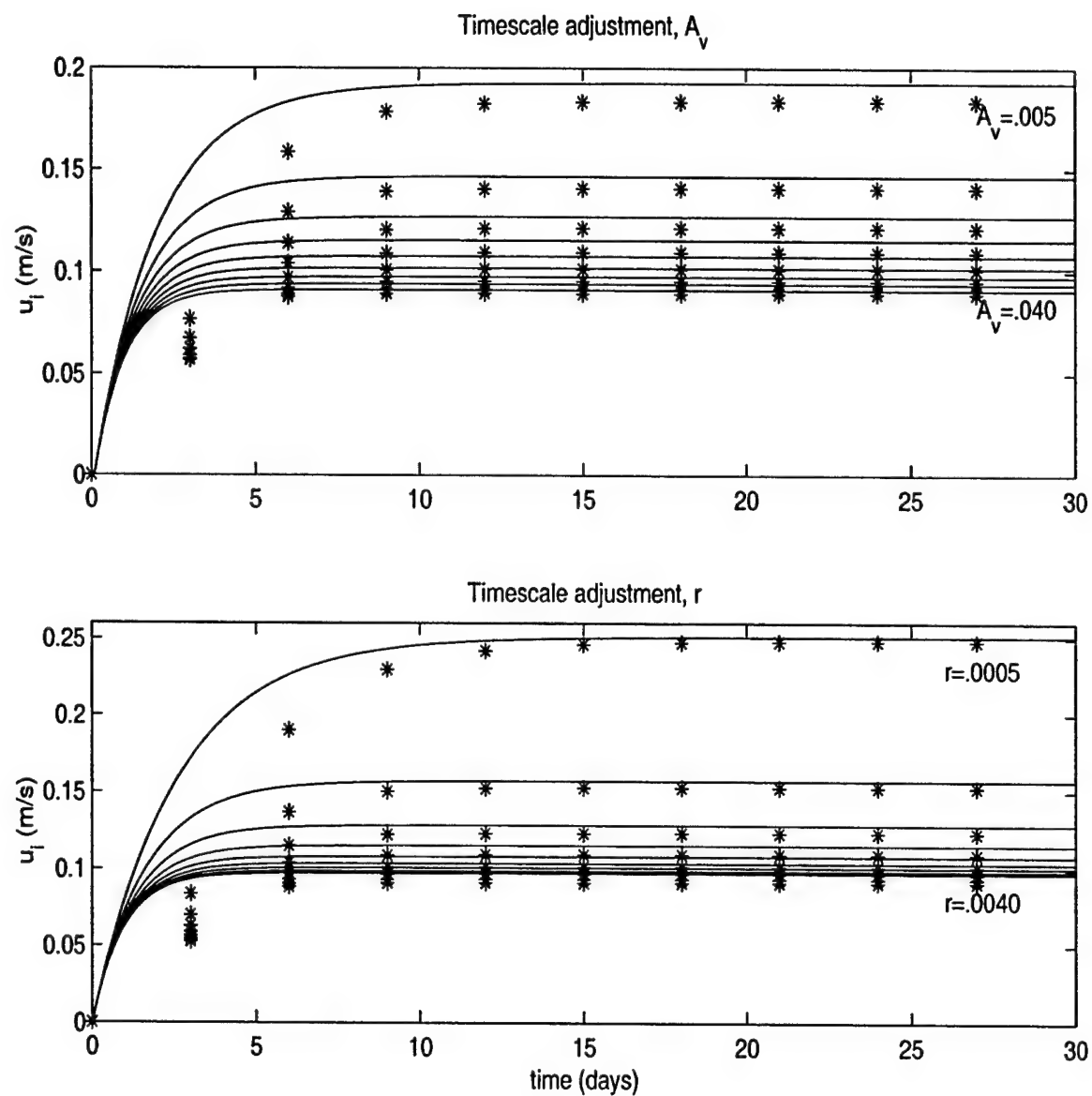
Figure 2-12: The development of u_i over time. (a) Varying the maximum allowed A_v (b) Varying r. Equation 2.37 for each run is show as a solid line. Model results are shown as asterisks.
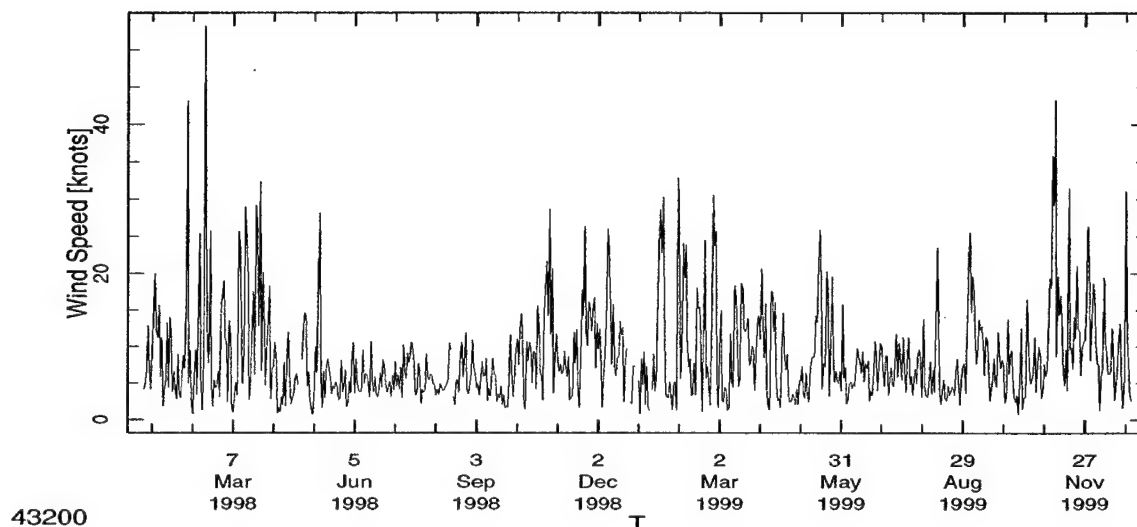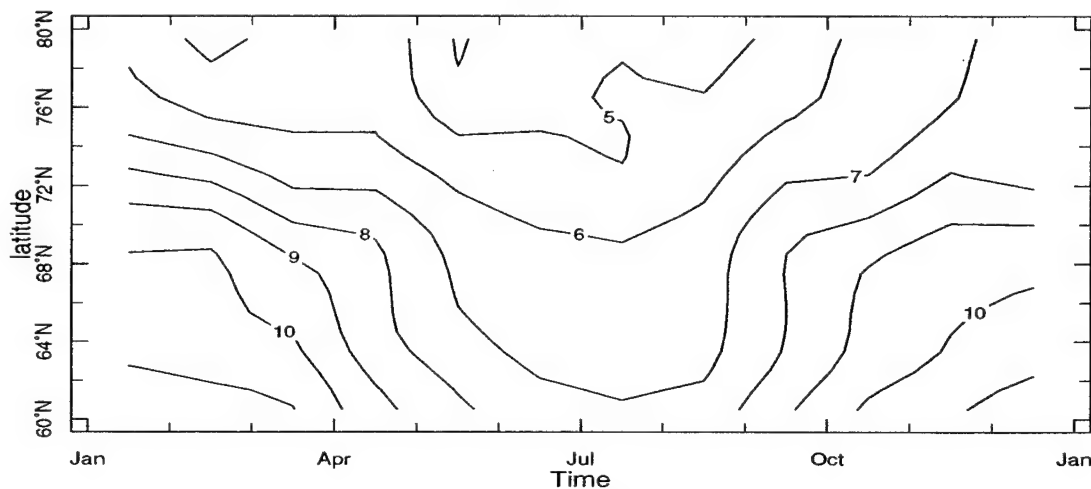
Figure 2-13: The observed wind speeds near the East Greenland Current. (a) weather station data from NOAA NCDC Weather Station BGDH. This weather station is located off the eastern coast of Greenland on a small island at an elevation of 12 m and at 76.76° N by 18.66° W. There are small hills near the weather station but no large mountains. The plot shows the daily mean wind speed. (b) Monthly mean wind speed at 10° W from the daSilva (1994) climatology.

speeds along the 10.5° W line. In the annual average, the wind speed off the Greenland coast is about 7.5 m/s directed approximately parallel to the coastline. In the winter, monthly mean wind speeds are about 10 m/s; in the summer they are about 5 m/s. In this chapter, the effect of sea ice on surface stress is neglected. A uniform drag coefficient between the ocean and atmosphere of $C_{aw} = 1.4 \cdot 10^{-3}$ is used[4]. The wind stress is calculated with equation 2.39.

$$\vec{\tau}_{aw} = \rho_{air} C_{aw} |\vec{U}_{air} - \vec{u_w}|(\vec{U}_{air} - \vec{u_w}) \approx \rho_{air} C_{aw} |\vec{U}_{air}| \vec{U}_{air} \qquad (2.39)$$

For typical wind speeds, the wind stress 0.1 N/m$^2 \pm$ 0.05 N/m^2 (Legutke, 1991).

Woodgate et al. (1999) observed a barotropic current of about 11 cm/s ± 6 cm/s in the vicinity of the East Greenland Current. They argue it is driven by wind. They use current meters moored primarily on the slope and shelfbreak rather than on the shelf and they do not directly measure the current at the foot of the East Greenland Front. For the purposes of this modeling effort and in the absence of better data, it is assumed the dynamics of the barotropic currents on the shelf are the same as those observed over the slope. This seems reasonable because the shallowest current meter, moored in about 400 m of water, has a similar signal to the current meters in deeper water. The parameters A_v and r are tuned so the solution for u_I matches the observed barotropic speeds.

Equation 2.33 gives the vertically integrated transport associated with U_I. Dividing by H gives an expression for the speed

$$u_I = \frac{\tau_x^s}{\rho_o f_0} \frac{2}{\delta} \frac{1}{\alpha_r - \alpha_i} \qquad (2.40)$$

---

[4]There is a wide range of estimates of the surface stress. In other modeling work related to this study (Hibler, 1979; Hakkinen, 1986) a value of $C_{aw} = 1.2 \cdot 10^{-3}$ is used. Legutke (1991) argues that the wind stress off the coast of Greenland should be about 0.1 N/m^2 in the annual average. For annual average winds of 7.5 m/s, a value of $C_{aw} = 1.4 \cdot 10^{-3}$ is backed out of equation 2.39. This value is higher than previous modeling work, but some observations (Brown and Liu (1982); Kellner et al. (1987)) suggest C_{aw} could be as high as $2.0 \cdot 10^{-3}$ in the Greenland Sea area.
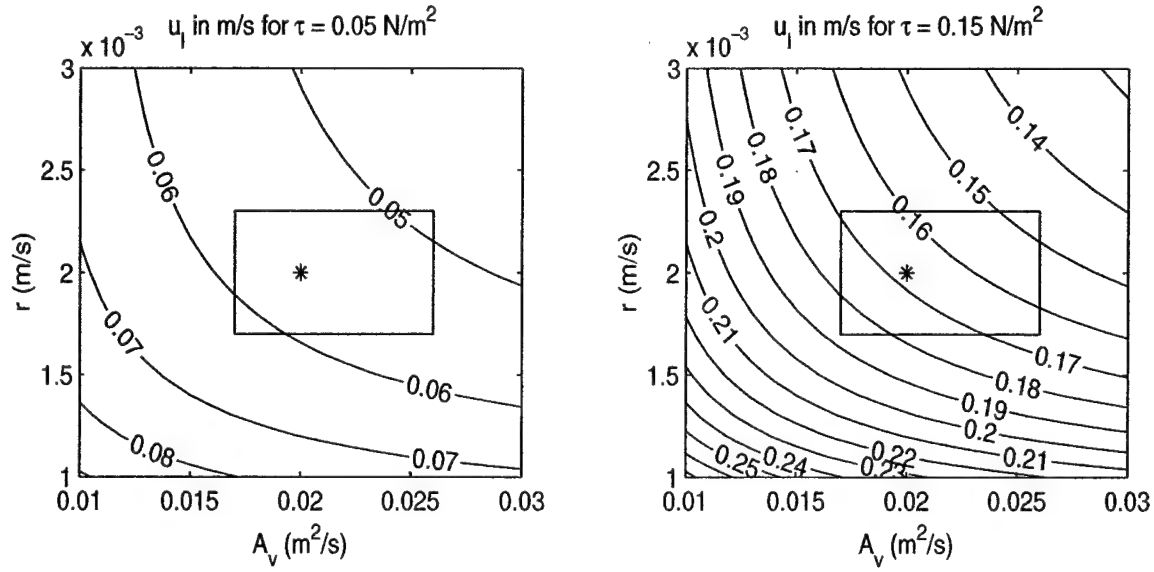
Figure 2-14: The dependence of u_I on r and A_v. (a) Under "summer-like" winds. (b) Under "winter-like" winds. The box indicates the region of acceptable values for r and A_v which produce barotropic flows close to those measured by Woodgate et al. (1999). The asterisk indicates the exact values used.

Figure 2-14 shows the dependence of u_I on r and A_v at two different wind stresses. To get speeds consistent with the observed speeds, A_v must be between 0.017 m^2 s^{-1} and 0.026 m^2 s^{-1} and r must be between $1.7 \cdot 10^{-3}$ m/s and $2.3 \cdot 10^{-3}$ m/s. In this study, $A_v = 0.02$ m^2 s^{-1} and $r = 2 \cdot 10^{-3}$ m/s. For this choice of A_v, the Ekman layer thickness, δ, is 17 m. The aspect ratio, $\epsilon = \frac{\delta}{2H}$ varies across the basin from 0.12 to .04 and it is 0.05 in the region where the front is situated.

For these values of r and A_v, the interior barotropic spin up time scale calculated from equation 2.36 is between 2 and 4 days. Since this time scale is short compared to the seasonally varying winds used in this study, the barotropic interior flow can be considered as quasi-steady.

2.5 The thickness of the mixed layers

In the previous section it was predicted that the wind and the barotropic inflow would both affect the thicknesses of the mixed layers at the top and bottom of the front. When there is wind, the surface mixed layer develops because the surface Ekman transport is to the right of the wind, or shoreward, and it advects heavy interior water over lighter coastal water. When there is a barotropic inflow, the bottom mixed layer thickness is increased because the bottom Ekman transport is offshore, advecting light water under the heavier water. The wind also generates a barotropic current but because of the constraint of mass conservation in the channel, there is not a net through transport of water. A downstream current is generated in shallow water but a jet with upstream transport develops at the offshore wall. Because this section will deal with net transports, the barotropic transport is assumed to be unrelated to the wind stress. In both cases, the density inversion is quickly corrected with convective mixing, forming a region of vertically homogeneous water. In this derivation, entrainment at the interface between the mixed layer and the interior water is neglected except for what arises from the convective adjustment.

2.5.1 Scaling the density equation

The density equation (2.5) is scaled to show that the first order balance is between the downstream and cross stream advection terms. It is then integrated across the mixed layers to develop relations for the thickness of the surface and bottom mixed layers. The density equation is rewritten below. The starred quantities indicate fully dimensional variables:

$$\frac{\partial \rho_*}{\partial t_*} + u_*\frac{\partial \rho_*}{\partial x_*} + v_*\frac{\partial \rho_*}{\partial y_*} + w_*\frac{\partial \rho_*}{\partial z_*} = \mathcal{F}_{\rho_*} + \mathcal{D}_{\rho_*} \tag{2.41}$$

The following simplifications are made. There is no forcing of the density field: $\mathcal{F}_{\rho_*}$ is zero. A steady or quasi-steady state is assumed. Obviously, during the initial

80

adjustment period, other terms (the time tendency, in particular) may be significant. The diffusive term, $\mathcal{D}_{\rho_*}$, is broken up into horizontal and vertical components. The horizontal component is Laplacian mixing. The vertical component is determined by the Mellor-Yamada scheme in the model. For scaling it is approximated as

$$K_v \frac{\partial^2 \rho_*}{\partial z_*^2}$$

Because the mixed layer is assumed to be a region of vertically uniform density, i.e. where $\frac{\partial \rho}{\partial z} = 0$, the vertical diffusion of density and the vertical advection of density are neglected. While this does not have to happen where the front intercepts either the top or bottom boundaries, it is assumed that the mixed layers are in contact with a boundary in this derivation. With these simplifications, equation 2.41 reduces to

$$u_* \frac{\partial \rho_*}{\partial x_*} + v_* \frac{\partial \rho_*}{\partial y_*} = K_H \nabla^2 \rho_* \tag{2.42}$$

The variables are scaled as:

$$
\begin{aligned}
\rho_* &= \Delta\rho \cdot \rho' & u_* &= \mu \cdot u' \\
x_* &= \Delta x \cdot x' & v_* &= \nu \cdot v' \\
y_* &= \Delta y \cdot y'
\end{aligned}
$$

where $\Delta\rho$ is the density difference across the front, Δx is the along channel scale of the front, Δy is the cross channel scale of the front or the width of the front in the cross channel direction, μ is the velocity scale in the along channel direction and ν is the velocity scale in the cross channel direction. The primes indicate dimensionless variables. Equation 2.42 becomes

$$\frac{\mu\Delta\rho}{\Delta x} u' \frac{\partial \rho'}{\partial x'} + \frac{\nu\Delta\rho}{\Delta y} v' \frac{\partial \rho'}{\partial y'} = \frac{K_H \Delta\rho}{\Delta y^2} \left(\left(\frac{\Delta y}{\Delta x}\right)^2 \frac{\partial^2 \rho'}{\partial x'^2} + \frac{\partial^2 \rho'}{\partial y'^2} \right) \tag{2.43}$$

81

Dividing 2.43 by $\frac{\nu \Delta \rho}{\Delta y}$

$$\frac{\mu}{\nu}\frac{\Delta y}{\Delta x}u'\frac{\partial \rho'}{\partial x'} + v'\frac{\partial \rho'}{\partial y'} = \frac{K_H}{\nu \Delta y}\left(\left(\frac{\Delta y}{\Delta x}\right)^2\frac{\partial^2 \rho'}{\partial x'^2} + \frac{\partial^2 \rho'}{\partial y'^2}\right) \qquad (2.44)$$

It is now shown that $\frac{K_H}{\nu \Delta y} < 1$ and the first order balance is between the advective terms. To show that $\frac{K_H}{\nu \Delta y}$ is small, estimates of Δy and ν are needed.

The cross shelf scale, Δy, is chosen as the baroclinic Rossby radius.

$$\Delta y = \sqrt{\frac{gH}{f_0^2}\frac{\Delta \rho}{\rho_o}} \qquad (2.45)$$

The baroclinic Rossby radius is the natural horizontal scale for the geostrophic adjustment of a rotating light fluid over a denser fluid.

The cross stream velocity scale is estimated from the transport in equation 2.33. Velocity is obtained by dividing by the appropriate vertical scale. For the cross shelf velocity scale, ν, the Ekman layer transport is divided by the thickness of the Ekman layer, δ

$$\nu \approx \frac{\tau_x^s}{\rho_o f_0}\frac{1}{\delta} \qquad (2.46)$$

Substituting 2.45 and 2.46 into $\frac{K_H}{\nu \Delta y}$,

$$\frac{K_H}{\nu \Delta y} \approx \frac{K_H}{\frac{\tau_x^s}{\rho_o f_0}\frac{1}{\delta}\sqrt{\frac{gH}{f_0^2}\frac{\Delta \rho}{\rho_o}}} \qquad (2.47)$$

All of the parameters in 2.47 are independent of the model dynamics and set as initial or boundary conditions. They are defined in section 2.2. They have the following values: $K_H = 40$ m^2 s^{-1}; $\tau_x^s = .1$ N m^{-2}; $\rho_o = 1000$ kg m^{-3}; $\Delta \rho = 0.9$ kg m^{-3}; $f_0 = 1.4 \cdot 10^{-4}$ s^{-1}; $\delta = \sqrt{\frac{2A_v}{f_0}} = 17$ m; $g = 10$ m s^{-2}; and $H = 160$ m. Substituting these values into the scales derived above, the cross shelf scale, identified as the baroclinic Rossby radius, is about 8.6 km; the cross stream velocity scale is 0.042 m/s and $\frac{K_H}{\nu \Delta y} \approx 0.1$. This ratio is less than one and the diffusion is neglected in the density

equation. Equation 2.44 becomes

$$\frac{\mu}{\nu}\frac{\Delta y}{\Delta x}u'\frac{\partial \rho'}{\partial x'} + v'\frac{\partial \rho'}{\partial y'} \approx 0 \tag{2.48}$$

From the continuity equation, $\frac{\mu}{\nu}\frac{\Delta y}{\Delta x} \approx 1$. Writing 2.48 in dimensional form, the first order balance in the density equation is

$$u\frac{\partial \rho}{\partial x} + v\frac{\partial \rho}{\partial y} = 0 \tag{2.49}$$

2.5.2 Predicting the thickness of the mixed layers

To estimate the thickness of the mixed layer, equation 2.49 is integrated in z from the lower surface of the mixed layer to the upper surface of the mixed layer. For the bottom mixed layer, the lower limit of integration is $z = 0$ m and the upper limit is unknown, notated as h_b. For the surface mixed layer, the upper limit of integration is the water depth, H and the lower limit of integration is unknown, $H - h_t$. h_b and h_t are assumed to be dependent on the downstream position, x.

This section carries out parallel derivations for $h_b(x)$ and $h_t(x)$. At each step the equations are paired. The expression for the bottom mixed layer is first and the expression for the surface mixed layer follows.

Integrating 2.49 over the mixed layers

$$\int_0^{h_b(x)} u\frac{\partial \rho}{\partial x}dz + \int_0^{h_b(x)} v\frac{\partial \rho}{\partial y}dz = 0 \tag{2.50}$$

$$\int_{H-h_t(x)}^{H} u\frac{\partial \rho}{\partial x}dz + \int_{H-h_t(x)}^{H} v\frac{\partial \rho}{\partial y}dz = 0 \tag{2.51}$$

The density gradients, $\frac{\partial \rho}{\partial x}$ and $\frac{\partial \rho}{\partial y}$ are assumed to be constant in the vertical direction in the mixed layer. They are removed from the integral and are evaluated at the boundary with stratified water. The density field can be approximated as a piecewise function. It is linear, with vertical isopycnals, in the mixed layer and it is

stratified above (below) that. As these integrals work from the bottom (surface) to the top (bottom) of the mixed layer and do not cross the boundary into the stratified region, they are one-sided integrals and the horizontal gradients do not need to be evaluated within the integral. Equations 2.50 and 2.51 become

$$\left.\frac{\partial\rho}{\partial x}\right|_{z=h_b}\int_0^{h_b(x)}u\,dz + \left.\frac{\partial\rho}{\partial y}\right|_{z=h_b}\int_0^{h_b(x)}v\,dz = 0 \qquad (2.52)$$

$$\left.\frac{\partial\rho}{\partial x}\right|_{z=H-h_t}\int_{H-h_t(x)}^{H}u\,dz + \left.\frac{\partial\rho}{\partial y}\right|_{z=H-h_t}\int_{H-h_t(x)}^{H}v\,dz = 0 \qquad (2.53)$$

where

$$
\begin{aligned}
\left.\frac{\partial\rho}{\partial x}\right|_{z=h_b} &= \left.\frac{\partial\rho}{\partial z}\right|_{z=h_b}\left.\frac{\partial z}{\partial x}\right|_{z=h_b} \qquad &(2.54)\\[2mm]
&= \left.\frac{\partial\rho}{\partial z}\right|_{z=h_b}\frac{\partial h_b}{\partial x}\\[2mm]
\left.\frac{\partial\rho}{\partial x}\right|_{z=H-h_t} &= \left.\frac{\partial\rho}{\partial z}\right|_{z=H-h_t}\left.\frac{\partial z}{\partial x}\right|_{z=H-h_t} \qquad &(2.55)\\[2mm]
&= \left.\frac{\partial\rho}{\partial z}\right|_{z=H-h_t}\frac{\partial}{\partial x}(H-h_t)\\[2mm]
&= -\left.\frac{\partial\rho}{\partial z}\right|_{z=H-h_t}\frac{\partial h_t}{\partial x}
\end{aligned}
$$

It was previously assumed that $\frac{\partial\rho}{\partial z} = 0$ in the mixed layers. However, this expansion of the horizontal derivatives includes the vertical density gradient evaluated at the top and bottom of the mixed layer. While $\frac{\partial\rho}{\partial z} = 0$ within the mixed layers, at the interface between the mixed layers and the stratified interiors, there is a density gradient. Physically, the reason the interior density gradient appears is because for the bottom (surface) mixed layer to change in thickness, enough light (heavy) water must be horizontally advected into it so that after the water has mixed convectively, the water above (below) it will have changed its density. It is easy to imagine that if the stratification at the boundary is large, a significant amount of density must be

advected into the mixed layer to change its thickness appreciably. However, if the density gradient at the interface is small, the mixed layer thickness will grow quickly.

The integrals in equations 2.52 and 2.53 are evaluated as follows:

$$\int_0^{h_b(x)} u\,dz = U_{tw}^b + \frac{h_b(x)}{H}U_I + U_b \tag{2.56}$$

$$\int_{H-h_t(x)}^{H} u\,dz = U_{tw}^t + \frac{h_t(x)}{H}U_I + U_s \tag{2.57}$$

and

$$\int_0^{h_b(x)} v\,dz = V_b \tag{2.58}$$

$$\int_{H-h_t(x)}^{H} v\,dz = V_s \tag{2.59}$$

where U_I, U_b, U_s, V_b and V_S are as defined in equation 2.33. U_{tw}^b is the along channel transport due to thermal wind in the bottom mixed layer and U_{tw}^t is the along channel transport due to thermal wind in the surface mixed layer. (It is assumed there is no cross channel transport due to thermal wind .)

Substituting the transports and expressions for $\frac{\partial \rho}{\partial x}$ into equations 2.52 and 2.53:

$$\frac{\partial \rho}{\partial z}\frac{\partial h_b}{\partial x}\left(U_{tw}^b + \frac{h_b(x)}{H}U_I + U_b\right) + \frac{\partial \rho}{\partial y}V_b = 0 \tag{2.60}$$

$$-\frac{\partial \rho}{\partial z}\frac{\partial h_t}{\partial x}\left(U_{tw}^t + \frac{h_t(x)}{H}U_I + U_s\right) + \frac{\partial \rho}{\partial y}V_s = 0 \tag{2.61}$$

The vertical bars indicating where the density gradients should be evaluated are dropped for notational clarity. Dividing by $\frac{\partial \rho}{\partial z}$ and defining

$$m = \frac{\frac{\partial \rho}{\partial y}}{\frac{\partial \rho}{\partial z}}$$

equations 2.60 and 2.61 become

$$\frac{\partial h_b}{\partial x} \left(U_{tw}^b + \frac{h_b(x)}{H} U_I + U_b \right) + m V_b = 0 \tag{2.62}$$

$$\frac{\partial h_t}{\partial x} \left(U_{tw}^t + \frac{h_t(x)}{H} U_I + U_s \right) - m V_s = 0 \tag{2.63}$$

The transport due to thermal wind is

$$\begin{aligned}
U_{tw} &= \int_a^b u_{tw} dz \tag{2.64} \\
&= \int_a^b \frac{g}{\rho_o f_0} \frac{\partial \rho}{\partial y} z \, dz \\
&= \frac{g}{\rho_o f_0} \frac{\partial \rho}{\partial y} \frac{z^2}{2} \Big|_a^b
\end{aligned}$$

This assumes that the thermal wind velocity is 0 m/s at the base of the bottom edge of the mixed layer. For the bottom mixed layer this means that the thermal wind velocity is 0 at the bottom and for the surface mixed layer this means that thermal wind velocity is 0 at the interface between the mixed layer and the unstratified interior. For the bottom mixed layer, $a = 0$ and $b = h_b(x)$. For the surface mixed layer, $a = H - h_t(x)$ and $b = H$. The transport due to thermal wind in the bottom mixed layer is

$$U_{tw}^b = d h_b^2(x) \tag{2.65}$$

and in the surface mixed layer it is

$$U_{tw}^t = d \left(2H h_t(x) - h_t^2(x) \right) \tag{2.66}$$

where d is the constant

$$d = \frac{1}{2} \frac{g}{\rho_o f_0} \frac{\partial \rho}{\partial y} \tag{2.67}$$

Equations 2.62 and 2.63 are rearranged and are first order, non-linear partial

86

differential equations:

$$\frac{\partial h_b}{\partial x} = -\frac{mV_b}{dh_b^2(x) + bh_b(x) + c} \tag{2.68}$$

$$\frac{\partial h_t}{\partial x} = \frac{mV_s}{(2Hd + b)h_t(x) - dh_t^2(x)} \tag{2.69}$$

where

$$
\begin{aligned}
b &= \frac{U_I}{H} \tag{2.70}\\
c &= U_B\\
d &= \frac{1}{2}\frac{g}{\rho_o f_0}\frac{\partial \rho}{\partial y}\\
&\approx \frac{1}{2}\frac{g}{\rho_o f_0}\frac{\Delta \rho}{\Delta y}
\end{aligned}
$$

The expressions used for U_I, U_b, V_b and V_S are derived in section 2.4 and are restated here:

$$
\begin{aligned}
U_I &= H u_{bt}\\
U_b &= -\frac{\delta}{2H}\left(\alpha_r + \alpha_i\right)U_I\\
V_S &= \frac{-\tau_x^s}{\rho_o f_0}\\
V_b &= \frac{\delta}{2H}\left(\alpha_r - \alpha_i\right)U_I
\end{aligned}
$$

Unlike in section 2.4, this form of the interior bottom velocities only depends on the interior flow and not on the wind stress. (To recover the expressions for the bottom transport in equation 2.33, the expression for U_I in terms of the wind stress is substituted.) By writing the transport equations in this form, the barotropic transport can be varied independently of the wind stress.

It is interesting to note that the front's density structure near the bottom is initially set by the buoyancy shutdown process described in Chapman and Lentz (1994). When the barotropic inflow is superimposed on the system, the structure changes significantly in response: the mixed layer thickens and the bottom Ekman trans-

port increases. However, the mechanism that trapped the front in the limit of no barotropic inflow remains intact. The net cross shelf advection of density reaches a steady state and the front reaches an equilibrium configuration. The addition of a barotropic inflow and the enhanced cross shelf density fluxes it forces does not replace the Chapman and Lentz (1994) and Chapman (2002) trapping mechanism, it superimposes additional fluxes on top of it.

In the limit of wind and no barotropic inflow (assuming that the barotropic current is completely independent of the wind stress), d is unchanged, and b, c and V_b are all zero because there is no interior barotropic flow. In that limit, the differential equations reduce to

$$\frac{\partial h_b}{\partial x} = 0 \tag{2.71}$$

$$\frac{\partial h_t}{\partial x} = \frac{mV_s}{dh_t(x)\left[2H - h_t(x)\right]} \tag{2.72}$$

In the limit of no wind but a barotropic inflow, $V_s = 0$ because there is no surface Ekman transport. The interior is unchanged. The equations reduce to

$$\frac{\partial h_b}{\partial x} = -\frac{mV_b}{dh_b^2(x) + bh_b(x) + c} \tag{2.73}$$

$$\frac{\partial h_t}{\partial x} = 0 \tag{2.74}$$

Steve Lentz suggested the following, alternate derivation for the mixed layer thickness. Consider a coordinate frame moving along the channel at the velocity of either boundary layer. Then, as time passes and it moves down the channel, more and more water is displaced in the cross isopycnal direction due to Ekman transport and drives convective deepening of the mixed layer. The cross shelf displacement of water in time interval dt is

$$dy = \frac{V}{h}dt$$

where h is the mixed layer thickness and V is the Ekman transport appropriate to

that mixed layer. The corresponding change in density is

$$
\begin{aligned}
d\rho &= \frac{\partial \rho}{\partial y} dy \\
&= \frac{\partial \rho}{\partial y} \frac{V}{h} dt
\end{aligned}
$$

To be stable, the boundary layer thickness changes by

$$
\begin{aligned}
dh &= \frac{d\rho}{\frac{\partial \rho}{\partial z}} \\
&= \frac{Vm}{h} dt
\end{aligned}
$$

where m is defined above. Rearranging,

$$
h\frac{\partial h}{\partial t} = Vm
$$

which implies that $h \propto \sqrt{t}$ in the reference frame of the boundary layer. This result can be converted into along channel coordinates as follows

$$
h\frac{\partial h}{\partial t} = h\frac{\partial h}{\partial x}\frac{\partial x}{\partial t} = U\frac{\partial h}{\partial x}
$$

where U is the total along channel transport, consisting of the thermal wind transport, the barotropic transport and any Ekman transports. The differential equation becomes

$$
U\frac{\partial h}{\partial x} = Vm
$$

which is equivalent to equations 2.52 and 2.53 if appropriate choices for V and U are made for the mixed layer in question.

2.5.3   Solving the equations

Equations 2.68 and 2.69 are solved using the differential equation solver in Matlab, with an initial condition of $h = 3$ m.[5] Both the x and y equations have singularities for values of h less than 3 m. Because the mixed layers rapidly grow to values much larger than 3 m and SPEM does not have adequate vertical resolution to investigate the behavior of very thin mixed layers, the singularities are not examined in detail. For all initial conditions larger than 3 m, the same results are obtained.

The coefficients a, b, c, d and m are evaluated as follows. For all experiments, g, ρ_o, $\Delta\rho$, f_0, H and δ are defined in section 2.2. The dimensionless numbers α_r and α_i are defined in equation 2.17 and are functions of r and A_v, which are defined in section 2.2. The wind stress, τ_x^s, is defined for each experiment. The cross channel scale, Δy, is the baroclinic Rossby radius. It is calculated from equation 2.45. The vertical scale, Δz, represents the vertical thickness of the front and it clearly must be between δ, the Ekman layer thickness, and H, the water depth. At the limit where it is close to δ, the front is barely mixed; in the limit where it is close to H, the front is mixed from surface to bottom. As there is no good theoretical scaling estimate for Δz, and a full range of frontal responses are observed, it is assumed to be equal to $\frac{H}{2}$ or 80 m. The sensitivity of the equations to variations in the vertical scaling was tested (not shown) and it does not have a significant impact on the results. The parameter m is estimated as $\frac{\Delta z}{\Delta y}$.

2.5.4   Sensitivity to parameter variation

The mixed layer depths depend on a wide range of parameters: the depth scale, the density difference across the front, the bottom drag coefficient, the vertical mixing,

---

[5]It was brought to my attention near the end of this process that 2.68 and 2.69 are ordinary differential equations that can be solved analytically by separation of variables. Furthermore, the solutions, gotten that way, can be non-dimensionalized and the relative importance of the scaled terms can be judged. This avenue of investigation may be pursued at a later date. In this thesis, I present the numerical results.

the wind stress and the barotropic inflow. In this section, the dependence of the mixed layer depth on wind stress and barotropic inflow is discussed.

In figure 2-15, the mixed layer thicknesses as a function of along channel distance versus wind stress or barotropic inflow are plotted. In all four plots, the mixed layer thicknesses increase over the length of the channel. The top two plots in figure 2-15 show how the bottom mixed layer (left) and the surface mixed layer (right) depend on variation in the wind stress when the barotropic inflow is held constant. The bottom mixed layer's behavior is independent of wind stress in the calculation shown in figure 2-15. It was shown earlier that while the wind generates an along-shelf barotropic transport in an infinite channel, in the finite channel the net along shelf transport is unchanged. Therefore, for this calculation, it is assumed that the along channel barotropic flow is completely independent of the wind stress. The bottom mixed layer thickness grows over the length of the channel because the small barotropic inflow generates a mixed layer and that mixed layer thickness depends only on the interior barotropic velocity. The surface mixed layer, on the other hand, deepens significantly over the length of the channel and as the wind stress increases, the mixed layer thickness also increases. The mixed layer deepens as the wind stress increases because the larger the wind stress, the larger the cross shelf Ekman transport while the along shelf transport is held constant. Therefore, for the cross shelf and along shelf transports to balance, a thicker mixed layer is needed.

The bottom two plots in figure 2-15 show how the bottom mixed layer (left) and the surface mixed layer (right) depend on variation in the barotropic inflow when the wind stress is kept constant. The bottom mixed layer increases steadily over the length of the channel and the larger the barotropic inflow, the larger the bottom mixed layer. As in the surface mixed layer, this is easy to understand. A larger barotropic inflow causes a larger stress on the bottom and the stress drives a larger cross shelf transport of density. For there to be a balance between the cross shelf transport of density and the along shelf transport of density, a thicker mixed layer is

91
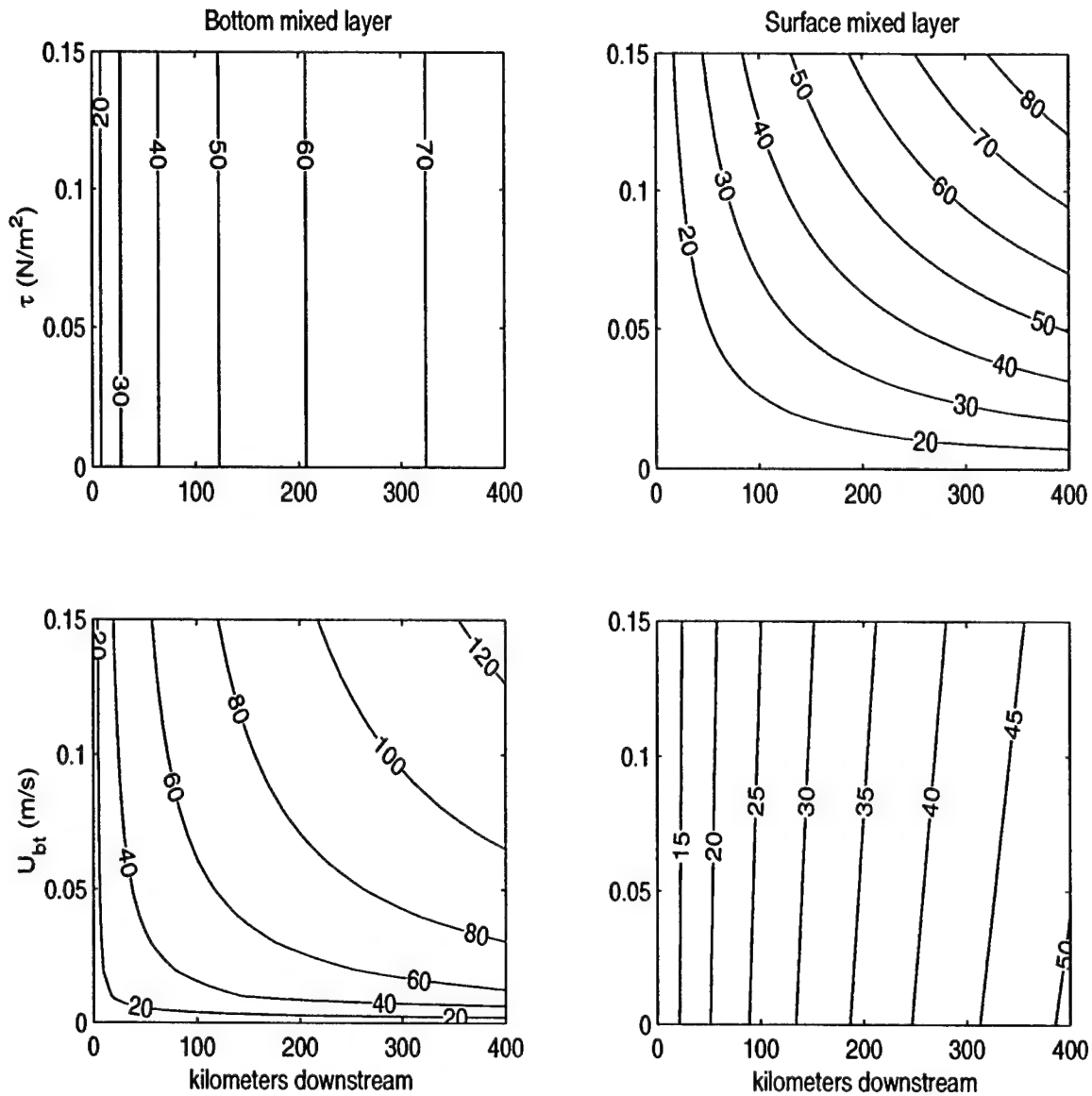
Figure 2-15: The predicted mixed layer as a function of distance downstream. On the left, the bottom mixed layer thicknesses are shown. On the right, the surface mixed layer thicknesses are shown. In the top two plots, the wind stress is varied from 0 N/m^2 to 0.15 N/m^2 while the barotropic inflow is held constant at 0.025 m/s. In the bottom two plots, the barotropic inflow is varied from 0 m/s to 0.15 m/s while the wind stress is held constant at .05 N/m^2.

needed. The surface mixed layer is mostly independent of the barotropic inflow and depends on the wind stress to create the cross shelf transport. However, the barotropic velocity does have some impact. The density balance is between the along stream advection and cross stream advection. When the barotropic inflow is increased, the along stream advection is increased and so the mixed layer thickness needed for this balance decreases.

The wind stress drives the cross shelf transport of water at the surface. If the wind stress is zero, the surface mixed layer has zero thickness, regardless of what any of the other parameters are. If there is no barotropic inflow, the bottom mixed layer has zero thickness because the barotropic inflow causes the bottom stress and the cross shelf advection of density at the base of the front. If the wind stress is able to spin up a barotropic current, the front will have both a bottom and surface mixed layer however in the calculations presented here, it is assumed that the wind stress and barotropic current is completely de-coupled.

In figure 2-16, the mixed layer depths 200 kilometers downstream are shown as a function of wind stress and barotropic inflow. The bottom mixed layer thickness only depends on the barotropic inflow. Its behavior is entirely independent of the wind stress imposed on the surface. On the other hand, the surface mixed layer depends on both the wind stress and the barotropic inflow. The surface mixed layer thickness is directly proportional to the wind stress and is inversely proportional to the barotropic inflow. The dashed line shows the predicted relationship between the wind stress and the barotropic current from 2.33. As one would expect, as the wind stress increases in strength, the barotropic current increases in speed and the surface mixed layer thickens. As a result of the barotropic current's increase speed, the bottom mixed layer also thickens. Therefore, in an infinite channel where the wind may spin up a barotropic current, both the surface and bottom mixed layers increase their thickness.

This model predicts that both the surface and bottom mixed layers can become quite substantial. In shallow water, it is possible that the combined thickness of the
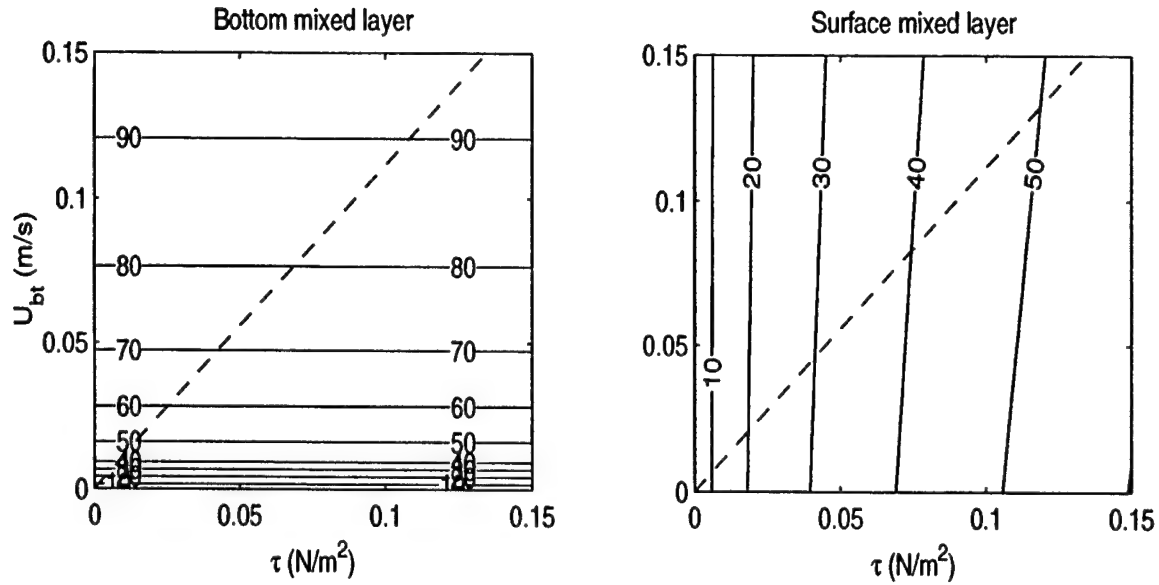
Figure 2-16: The mixed layer depths 200 kilometers downstream, as a function of wind stress and barotropic inflow. The bottom mixed layer is to the left and the surface mixed layer is to the right. The dashed line indicates the predicted relationship between the wind stress and the barotropic current from equation 2.33.

surface and bottom mixed layers may exceed the water depth. In that extreme, the mixed layers merge and the water is vertically uniformly mixed.

2.6 Model Results

In this section, a series of numerical experiments with different boundary conditions are discussed and compared to the predictions of the previous sections. First, model dynamics are examined when the model is forced by wind and/or a barotropic inflow. Then a discussion is given of the mixed layer thicknesses and finally frontal location is discussed as a function of wind stress and barotropic inflow.

All of the numerical experiments start from the same spun up, unforced, base run described below. The spin up experiment is similar to experiments in Chapman and Lentz (1994), Yankovsky and Chapman (1997), Chapman (2000) and Chapman (2002).
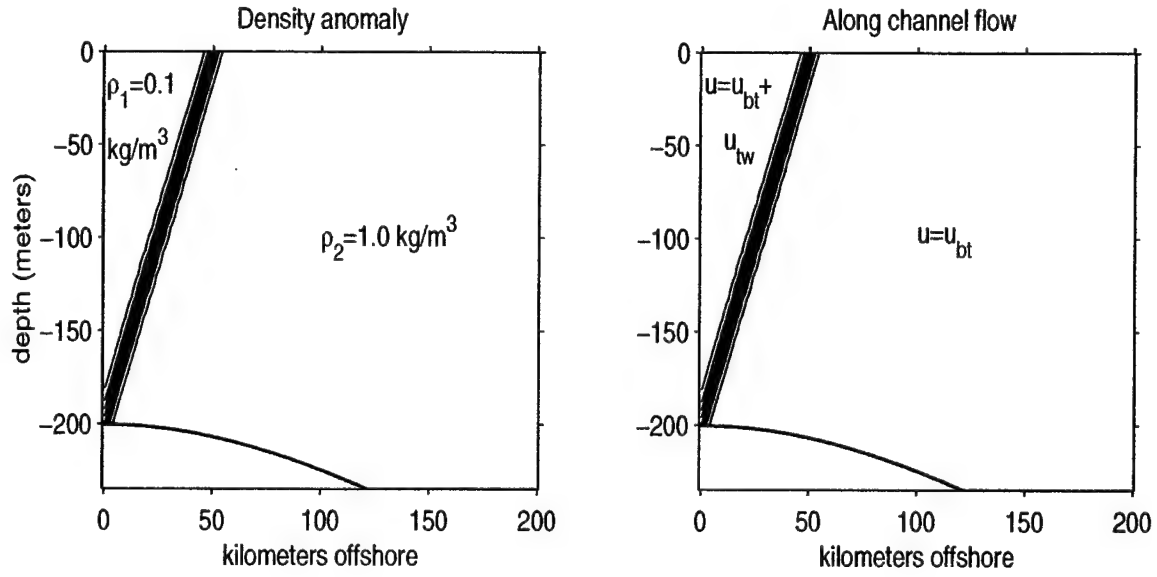
Figure 2-17: The inflow boundary condition. (a) The inflow density field. (b) The inflow along-channel velocity structure. u_{tw} refers to the along-channel flow generated by the density structure. u_{bt} is an additional barotropic velocity imposed over the entire inflow area.

The model is started from rest and the channel is filled with homogeneous water of density anomaly $\rho_2=1$ kg m^{-3}. At $t=0$, a steady flux of lighter water with $\rho_2-\rho_1 = \Delta\rho = 0.9$ kg m^{-3} is introduced as a wedge at $x=0$. The density difference is similar to the difference between the Polar Water and the interior water in the Norwegian Sea off the coast of Greenland (Mauritzen, 1996a).

The inflow velocity of light water is in thermal wind balance. A small barotropic velocity of 2.5 cm/s is added. This value is consistent with the estimated barotropic speed at Fram Strait (Foldvik et al., 1988). The upstream boundary conditions are shown in figure 2-17. There is no wind stress imposed on the initial condition.

The transport due to thermal wind is about 1.25 Sv. An additional 1.1 Sv of transport through the upstream wall comes from the barotropic component. Foldvik et al. (1988) observe a transport of about 3 Sv through Fram Strait above 700 m: about half barotropic and half baroclinic. The shape of the model domain is different from the topography near the mooring array from Foldvik et al. (1988) and the

95

barotropic component cannot be compared. The baroclinic part in the model's inflow boundary condition is similar to the observations.

Figure 2-18 shows several snapshots of the model's density field as it adjusts to equilibrium. The snapshots are a plan view of the model domain, mid-level through the water column. Initially, a tight stream of light water travels along the coastal wall. It is followed by a larger plume of light water which moves offshore before propagating downstream. The remaining adjustment of the model fills the region between the two plumes with light water. The time scale of this part of the adjustment is given by the volume of dense water displaced divided by the rate with which light water is introduced into the domain. This time scale is called the "filling time scale" for the shelf region.

The offshore plume travels downstream along an isobath. The details of the adjustment process are discussed in Chapman and Lentz (1994) and are summarized in section 2.3.1. The equilibrium depth where the front is trapped is discussed in that section and given by equation 2.8. For $T = 1.25$ Sv and $\Delta\rho = 0.9$ kg m^{-3}, the predicted equilibrium depth is 197 m, slightly deeper than the location where the front stops in the numerical experiment.

A cross section of the density field after 200 days of integration is shown in figure 2-19a. A well developed front with a distinct bottom mixed layer is present. The mixed layer is formed by the bottom Ekman layer: it transports light water offshore under heavier water. The water column convectively adjusts, creating the bottom mixed layer.

The front is associated with an along-channel surface intensified jet. The along channel velocity is shown in figure 2-19b. The jet has a cross channel width of about 50 km, about five times the baroclinic Rossby radius. Observations of the East Greenland Current such as Bourke et al. (1987), Woodgate et al. (1999) and Schlichtholz and Houssais (1999) all observe the jet of the East Greenland Current as having a cross shelf scale of about 50 km. Since the density difference across

The density field on k=15
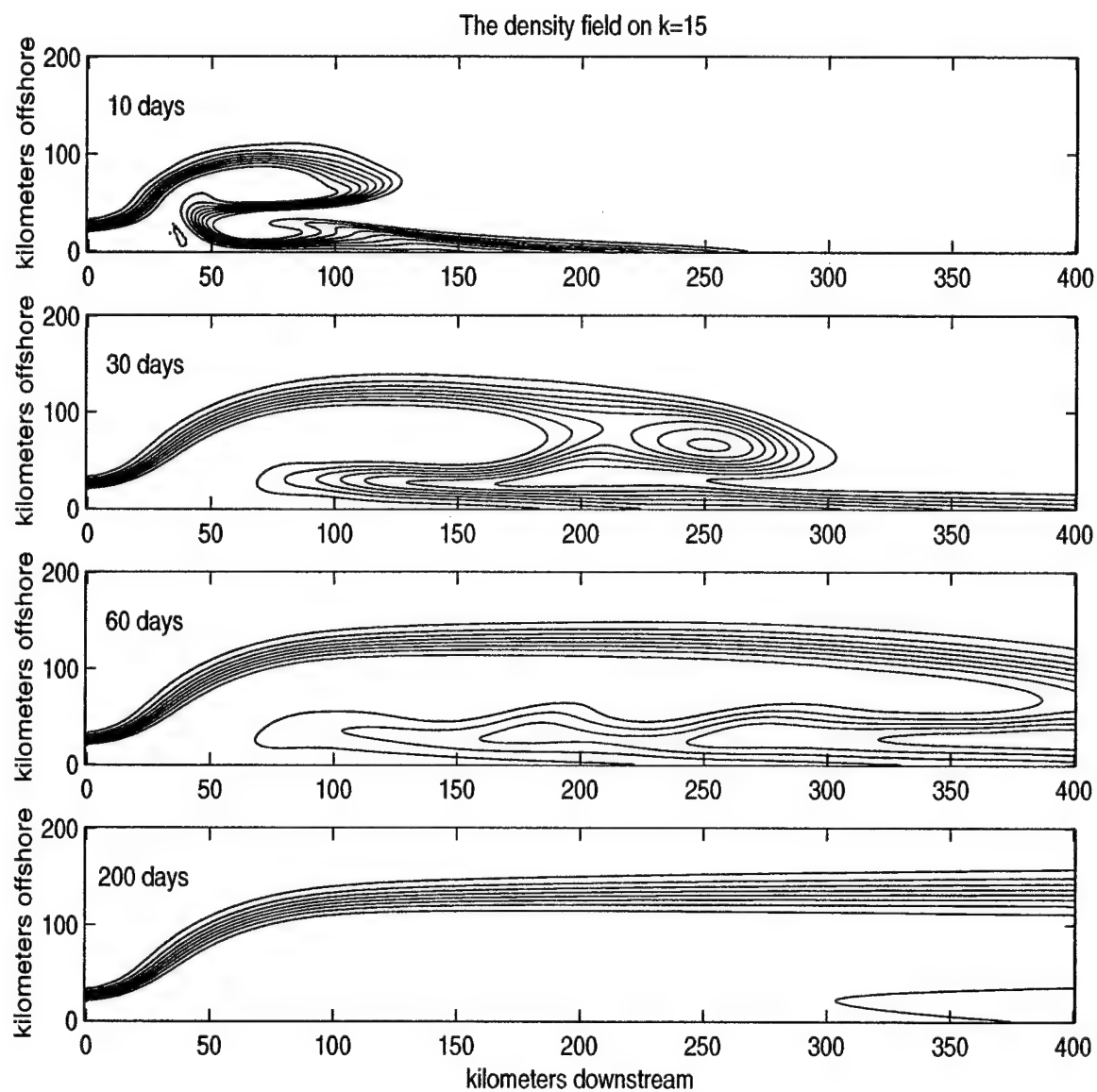
Figure 2-18: Four snapshots of the density structure during the spin up. The slice is taken at model level 15, which occurs roughly halfway down the model domain. After 200 days, the front has reached an equilibrium position.

Figure 2-19: The initial condition experiment, a slice through the channel at x=200 km, after 230 days. In this experiment, there density driven jet is superimposed on a barotropic inflow of 2.5 cm/s and there is no wind stress. (a) density anomaly (kg m^{-3}) (b) along-channel velocity, positive downstream (m/s) (c) cross-channel velocity, positive offshore (m/s)(d) vertical velocity, positive up (times 1·10^6 m/s). To reduce the contours, the 0 contour was eliminated from the w plot. In all figures, the location of the front is shaded. Dotted contours indicated negative values. Note the well developed bottom mixed layer.

the front, water depth and slope, and inflow are chosen to be similar to the East Greenland Current, the similarity between the two frontal widths is not surprising.

In figure 2-19c, the cross shelf velocity is shown. At the bottom, there is significant offshore Ekman transport, with a distinct convergence under the front. In the interior, the water velocity is shoreward, balancing the mass transport of the bottom Ekman layer. The shoreward velocity is larger within the jet, indicating that the jet is not parallel to the isobaths but is angled shoreward down the channel. These results differ from Chapman (2002) because there is a barotropic inflow of 2.5 cm/s imposed in this experiment.

Figure 2-19d gives the vertical velocity. Values are multiplied by $1 \cdot 10^6$. The most prominent feature is the noise in the bottom boundary layer. The noise may be related to the trapped frontal waves observed in Chapman (2002). Within the front, there is a region of upwelling and offshore of the front there is a region of downwelling. Mass is supplied to the bottom Ekman layer from vertical motion at the walls: at the shoreward wall there is downwelling and at the offshore wall there is upwelling.

2.6.1 Discussion of specific model runs

In this section, the model responses in the limits of a barotropic inflow with no wind and with wind and a very small barotropic inflow are discussed. The barotropic inflow experiment has no wind stress and a barotropic inflow of 11 cm/s. The wind stress experiment has stress of 0.15 N/m^2 imposed at the surface of the model (equivalent to the average winter wind stress in the Greenland sea) and a barotropic inflow of 0.5 cm/s. The barotropic inflow could not be set to 0 because the front moves so far offshore that it interacts with the offshore model wall.

The boundary condition for u is the sum of the thermal wind velocity associated with the front and the barotropic flow. At each time step, u_I is added to u_{tw}, at $x = 0$ km. An example of the inflow boundary condition under wind is show in figure 2-20.
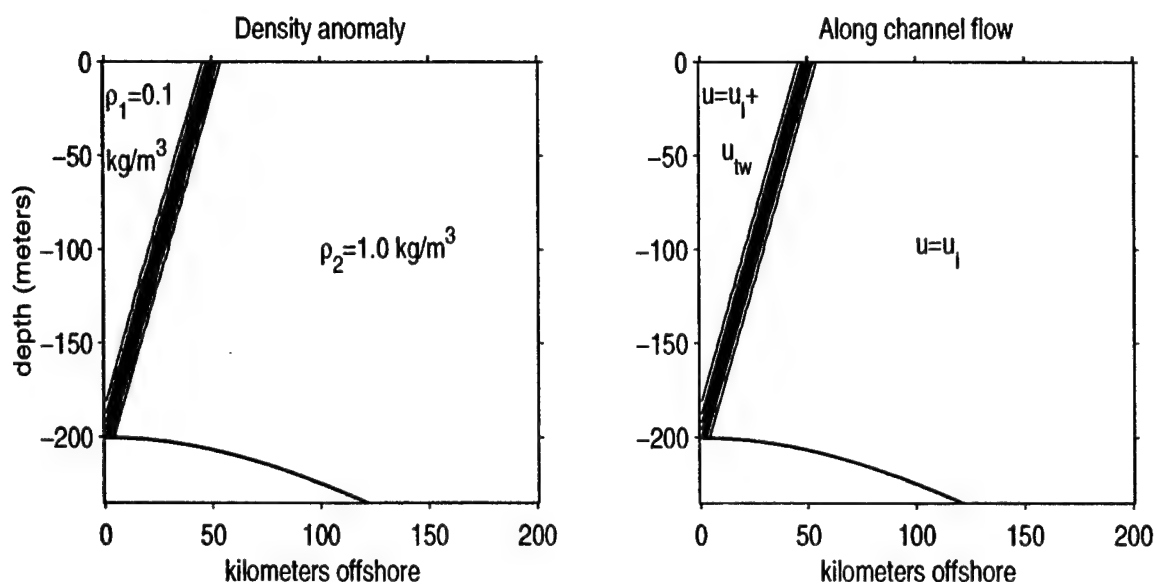
Figure 2-20: The modified inflow boundary condition under wind. It is similar to the configuration described in figure 2-17, except $u_{bt} = u_I$ and u_I is calculated from equation 2.40 at each time step.

In figure 2-21 the results of barotropic inflow only experiment are given and in figure 2-22 the results of wind only experiment are given. In both figures, the upper left panel gives the density anomaly field, the upper right panel gives the along channel velocity, the lower left panel gives the cross channel velocity and the lower right panel gives the vertical velocity. In all panels, the front is superimposed in grey. The cross section snap shots are taken 200 km downstream of the inflow, after 30 days of integration.

In both cases, there is a surface intensified jet moving in the along-shelf direction. In the wind stress experiment, the along-shelf velocity has regions of reversal on the offshore side of the front and under the front, while the along shelf velocity is always in the same direction in the barotropic inflow experiment. In both cases, the along channel velocity approaches 0 in the bottom boundary layer. The Chapman and Lentz (1994) observed this reversal and in Chapman (2002) it was noted that it was not required for the front to trap. While all experiments presented here use the Mellor-Yamada 2.0 mixing, like Chapman (2002), it seems that with the appropriate

100

Figure 2-21: The barotropic inflow only experiment. (a) density, (b) along-channel velocity, positive downstream (m/s) (c) cross-channel velocity, positive offshore (m/s)(d) vertical velocity, positive up (times $1 \cdot 10^6$ m/s). In (a) and (b) the contour intervals are the same as in figure 2-19; in (c) and (d) the contour interval is twice as large in figure 2-19. In all figures, over plotted shading shows the location of the front. Dotted contours indicated negative values.

101

Figure 2-22: The wind only experiment. (a) density, (b) along-channel velocity, positive downstream (m/s) (c) cross-channel velocity, positive offshore (m/s)(d) vertical velocity, positive up (times $1 \cdot 10^6$ m/s). In (a) and (b) the contour intervals are the same as in figure 2-19; in (c) and (d) the contour interval is twice as large in figure 2-19. In all figures, over plotted shading shows the location of the front. Dotted contours indicated negative values.

boundary forcing both trapping with and without the reversal occur.

In the barotropic inflow experiment, the jet is clearly superimposed on an along channel barotropic current which is stronger in deeper water. This is in agreement with Csanady (1978) and the arrested topographic solution previously discussed. In the wind stress only experiment, shoreward of the front, there is a barotropic velocity of about 3 cm/s, generated by the wind. This barotropic velocity increases down the channel (not shown), suggesting the barotropic transport is "spinning up" as the water is advected downstream. Offshore of the front and under the front there are regions of upstream transport. The upstream jets are required so that the mass is conserved in the along channel direction.

In the cross stream direction, the differences between the experiments are particularly obvious both in the velocity structure and the impact it has on the shape of the front. The barotropic inflow experiment (figure 2-21) has a bottom Ekman layer with a significant offshore transport. The velocity increases as the water moves offshore, as is expected from the arrested topographic wave behavior. Under the front, there is a region of local convergence, where the velocity decreases for a short distance and then increases. This convergence pumps water up and out of the bottom boundary layer. Throughout the interior, there is a slow return flow which pushes the front shoreward. The bottom Ekman transport causes the bottom mixed layer to be quite thick.

The wind stress experiment shows a different picture (figure 2-22). The wind stress creates a significant surface Ekman layer, advecting the surface water shoreward. The cross shelf transport creates a significant surface mixed layer. On the offshore side of the front, the surface mixed layer reaches the bottom mixed layer and the front is vertical.

The surface Ekman transport generates a barotropic current in the same direction as the wind, as discussed in section 2.4. This barotropic flow is particularly obvious in the shallow water shoreward of the front. The barotropic velocity generated by the

103

wind stress drives a bottom Ekman layer with an off shore cross shelf transport. As predicted in section 2.4, the surface shoreward mass flux is balanced by the transport in the bottom boundary layer. Offshore of the front and under the front, regions with upstream transports, balancing the downstream mass flux from the wind generated barotropic flow, drive shoreward Ekman transports. Directly under the front, this drives the isopycnals up-slope, causing a small "kink" in the isopycnals and detaching the mixed layer from the bottom.

The vertical velocity has two features, common on both plots. First, on the shoreward and offshore walls, there are regions of significant vertical transport. The vertical velocity is due to the convergences and divergences caused by the Ekman layers and they are clearly an artifact of the model geometry. The other common feature is upwelling in the general area of the front. This is expected from the various works that predict (and observe) upwelling out of the bottom boundary layer under the front.

2.6.2   The mixed layer thickness

In section 2.5, relationships that predict the thicknesses of the surface and bottom mixed layers are developed. In this section, the predictions are compared with the model results for a few selected model runs.

Figure 2-23 shows the thickness of the surface and bottom mixed layers for four experiments. The base of the bottom mixed layer is defined as the interception with the bottom of the anomaly isopycnal 0.5 kg/m^3. The top of the bottom mixed layer is defined as the height where the isopycnal has moved to the maximum distance of one kilometer from its bottom position. This condition is necessary because of the very small vertical density gradients still present within the mixed layers, which do not affect the overall well mixed nature of the layer. A schematic of this method is show in figure 2-24. The surface mixed layer is defined in a similar manner. The thickness of both mixed layers grows downstream until they merge. Where the mixed layers
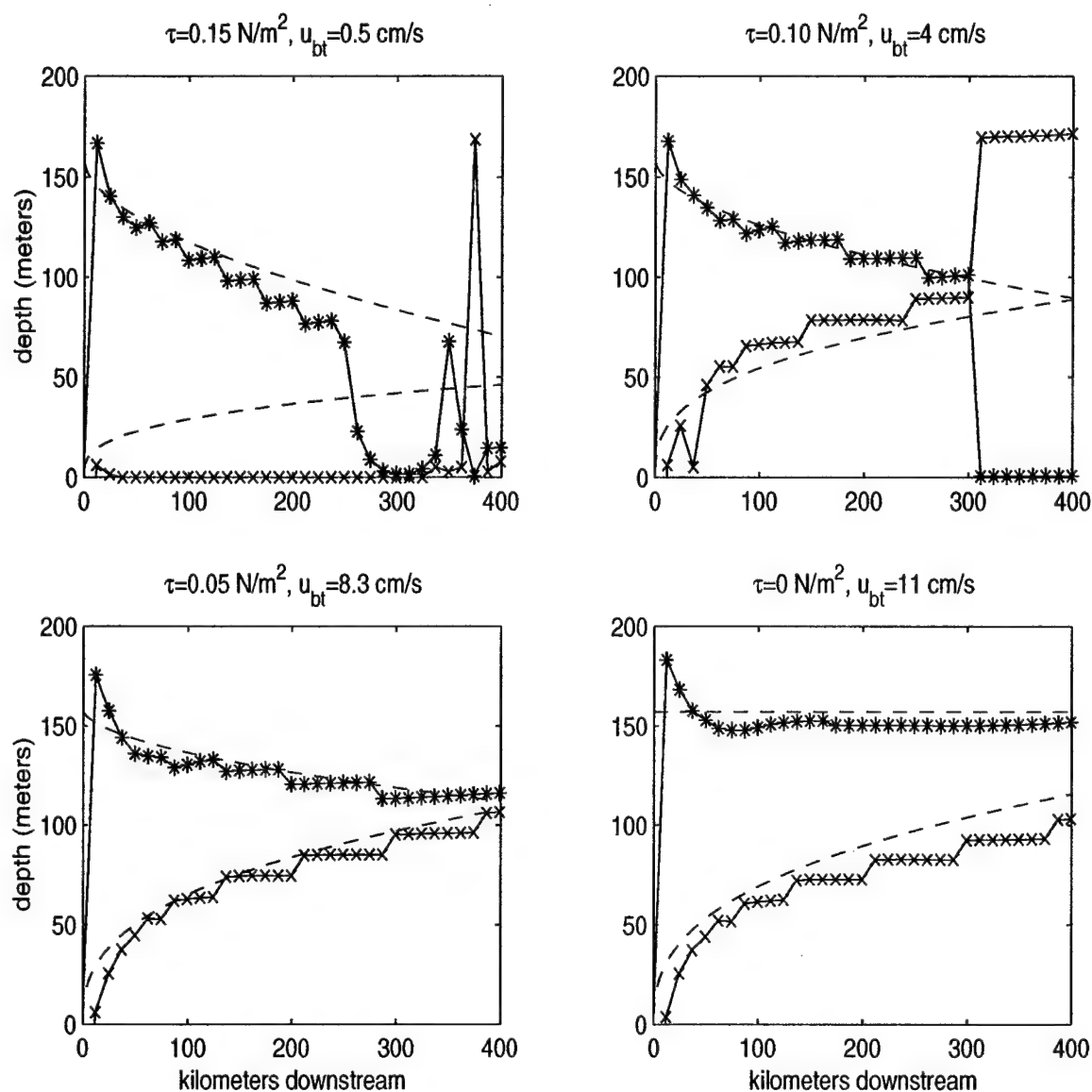
Figure 2-23: The model mixed layer thicknesses and the predicted mixed layer thicknesses as function of distance downstream for four different experiments. The upper left plot is the same experiment shown in cross-section in figure 2-22; the lower right plot is the same experiment shown in cross-section in figure 2-21. The other two plots show intermediate winds and barotropic inflows. For all experiments, the mixed layer thickness of the $\rho=0.5$ km/m^3 isopycnal is shown. The top of the bottom mixed layer is indicated by a line with crosses on it. The bottom of the surface mixed layer is indicated as a line with asterisks on it. The predicted mixed layers are indicated by a dashed line. The observed results have a step structure corresponding to locations where the mixed layer in the model penetrates to another model layer. The large jump in the mixed layer thickness 300 km downstream on the upper right figure is where the mixed layers touch and the water becomes vertically homogeneous.

105
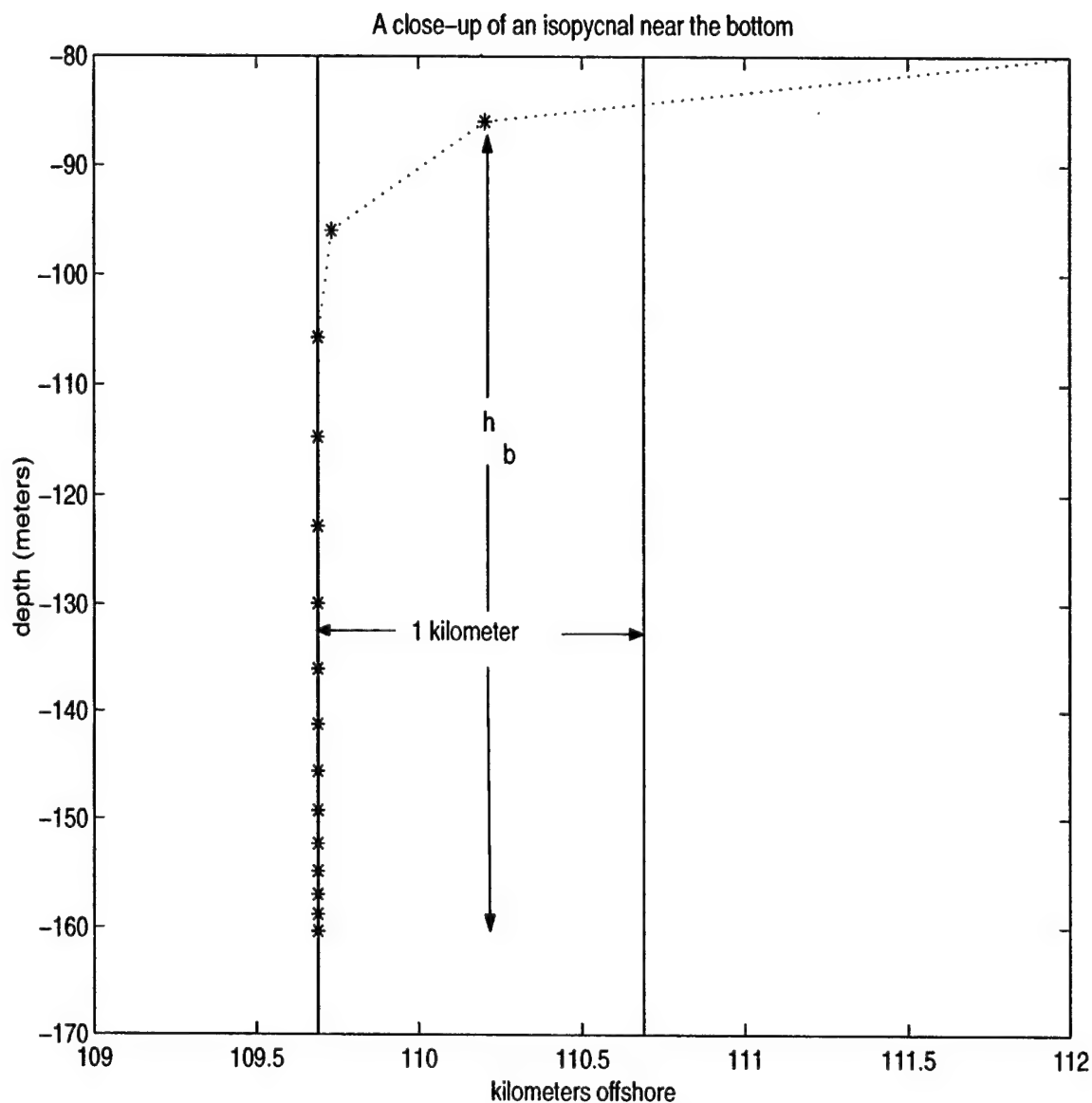
Figure 2-24: A schematic of how the mixed layer thickness is estimated. The dotted line with asterisks is a close up of a sample isopycnal near the bottom. The asterisks indicate model levels in the vertical. The solid line on the left where the isopycnal intercepts the bottom. The solid line on the right is one kilometer away. The bottom mixed layer thickness is the distance from the bottom, about 160 meters for this case, to the vertical grid point before the intersection of the right line with the isopycnal.

touch, a uniformly mixed water column forms. For the choice of $\Delta\rho$ and bottom slope in this study, vertical isopycnals are stable. Based on other runs, not discussed here, if $\Delta\rho$ increases or the bottom slope decreases, the front becomes unstable near the location where the isopycnals become vertical.

In general, the predicted relations are not unreasonable, but there are some discrepancies which require discussion. The upper-left plot in figure 2-23, which is the same experiment shown in cross-section in figure 2-22, shows the results for a wind stress of 0.15 N/m^2 and a barotropic inflow of 0.5 cm/s. The surface mixed layer agrees well with the prediction until about 275 km downstream where the two mixed layers touch, creating the large jump in mixed layer thickness. The large jump implies that nearly the entire water column is mixed at this point. The bottom mixed layer agrees very poorly with the prediction. Examining the density structure near the base of the front in figure 2-22, the isopycnals are clearly bent near the bottom. While there is a significant mixed layer in the interior, it does not intersect the bottom. The reason the isopycnals are no longer vertical is that the shoreward transport in the bottom Ekman layer has advected the isopycnals up-slope. The vertical density gradient would decrease with vertical mixing but because the Mellor-Yamada 2.0 scheme is used to parameterize vertical mixing there is almost no mixing within the front (Chapman, 2002). The definition of the mixed layer used in this study is the height above the bottom where the isopycnal is 1 kilometer from its intersection with the bottom. In this experiment, this condition is met within a few meters of the bottom.

The upper-right graph in figure 2-23 shows the result for a wind stress of 0.10 N/m^2 and a barotropic inflow of 4 cm/s. For both the surface and bottom mixed layers, there is good agreement over the length of the front until about 300 km downstream where the two mixed layers come into contact and the entire water column is mixed. While this happens earlier than expected from the scaling, the differences can be attributed to the finite layer thicknesses of the numerical model. It is interesting to note that

the bottom mixed layer agrees well with the prediction implying that the bottom mixed layer touches the bottom and the isopycnals are not tilted. By comparison with other experiments (not shown) both the increase in barotropic velocity and the decrease in wind stress contribute to this effect. By decreasing the wind stress, the downstream barotropic transport that the model creates in response to the wind is decreased and the upstream return flow is also diminished. By increasing the barotropic inflow, the front is pushed shoreward and the barotropic current is closer to the values predicted from the wind stress. Together, they contribute to a bottom mixed layer that intersects the topography.

The two bottom panels of figure 2-23 (left: wind stress is 0.05 N/m^2 and the barotropic inflow is 8.3 cm/s; right: wind stress is 0.0 N/m^2 and the barotropic inflow is 11 cm/s) show good agreement with the predictions. As the wind stress decreases, the surface mixed layer decreases in thickness and as the barotropic inflow increases, the bottom mixed layer increases in thickness. In general, for large barotropic inflows, the predictions agree well with the model results because the dominant cross shelf fluxes in both the surface and the bottom mixed layers create unstable density profiles resulting in convective mixing.

A possible reason the predictions may be poor for large wind stress has to do with choosing the barotropic transport, U_I, to be independent of the wind stress and equal to the barotropic inflow through the inflow boundary wall. As it was shown, this is a poor approximation: while the net along shelf transport is set by the boundary condition, the wind generates a barotropic velocity throughout the majority of the channel, including in the region of the front. Therefore, as the local barotropic velocity is controlled by the wind, the appropriate choice for U_I may be the velocity predicted from the wind stress. In general, the predictions fail when the cross shelf advection creates stable vertical density gradients and the dominant vertical mixing is given by the mixing scheme, rather than due to convective mixing.

2.6.3 Frontal location

In section 2.3 it was predicted that the front moves shoreward if there is a barotropic current and offshore if there is a wind stress. When both processes are present, the two compete and the frontal location is between where it would be with only one process acting on the front. In figure 2-25, the position of the intersection of the 0.5 kg/m^3 isopycnal with the bottom is shown for a wide range of wind stresses and barotropic inflows. The position of this isopycnal is used to define the location of the front and it is selected arbitrarily.

The depth of the front is strongly controlled by the barotropic inflow. The larger the barotropic inflow, the shallower the front, as predicted. The role of the wind stress is more subtle but for any selected barotropic inflow, as the wind stress increases, the depth of the front also increases.

To test the hypothesis that the interior cross shelf transport is related to the frontal position, the cross shelf transports of the bottom Ekman layer, the surface Ekman layer and the interior are calculated for all of the different experiments indicated in figure 2-25. The Ekman layer transports are defined as the water volume within two Ekman layer thicknesses from the boundary (either the air-water interface or the bottom). The interior is the water volume between the two Ekman layers. The cross shelf transports are calculated at two positions: 50 kilometers offshore and 185 kilometers offshore. In all of the experiments presented, the front is always offshore of 50 kilometers and shoreward of 185 kilometers, so these positions are always outside the jet. The transport is integrated over 100 kilometers, from 150 kilometers to 250 kilometers downstream of the inflow.

The transports are shown in figure 2-26. The bottom boundary layer transport is always offshore. Shoreward of the front, the transport is quite small and is mostly controlled by the wind stress. This is expected from the adjustment of a barotropic inflow over a sloping bottom: the barotropic current is weaker over shallower water and so the bottom boundary layer transport is also smaller. The importance of the

109
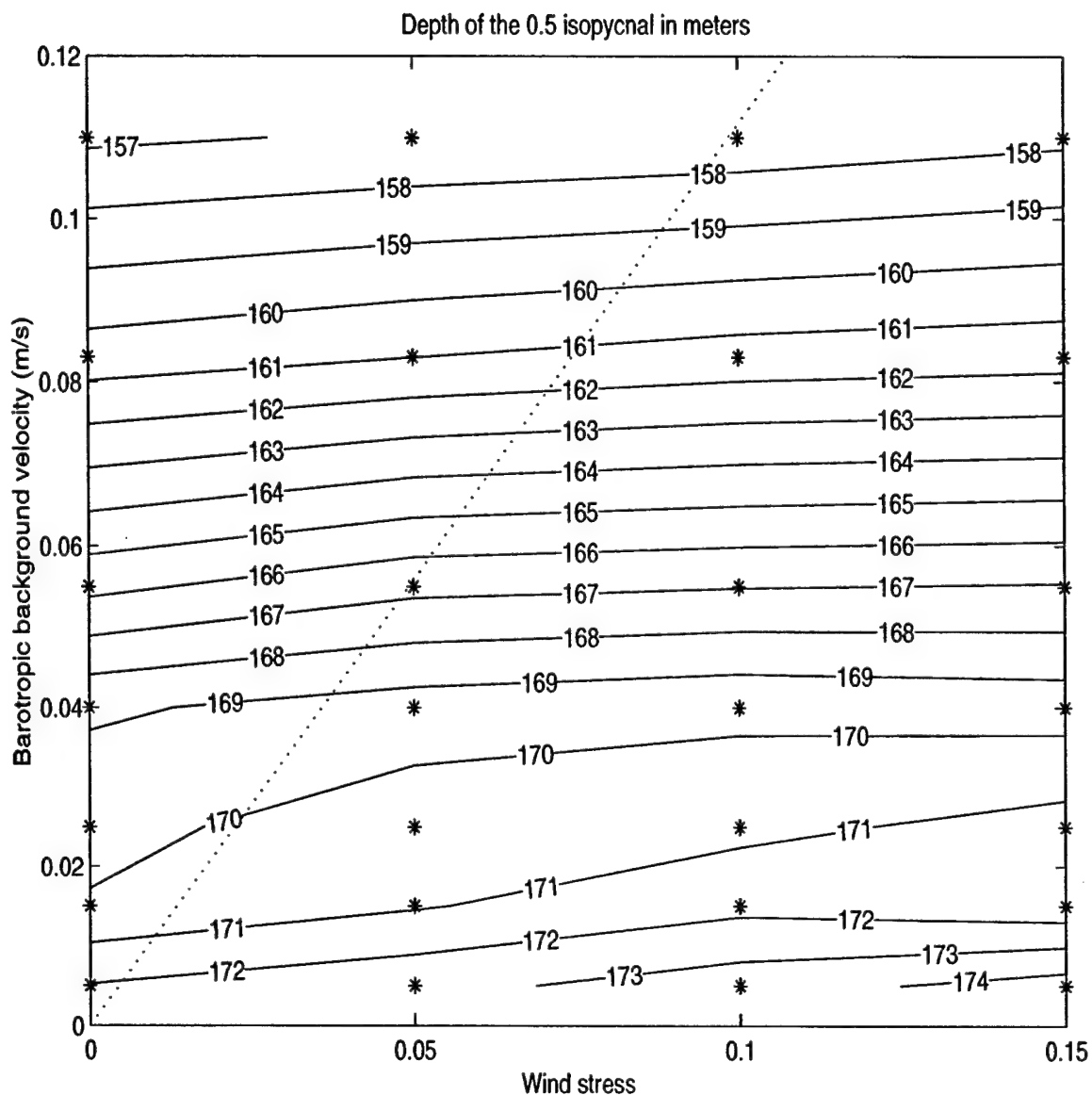
Figure 2-25: The depth of the intersection of the 0.5 kg/m^{-3} isopycnal with the bottom, as a function of wind stress and barotropic background flow. Measurements are made 200 kilometers downstream from the inflow. Asterisks indicate completed numerical experiments and the dotted line indicates the predicted relation between barotropic inflow and wind stress (equation 2.38). Experiments to the left of the line have a larger imposed barotropic velocity than would be expected for that wind stress and experiments to the right have a smaller imposed barotropic velocity than would be expected for that wind stress.
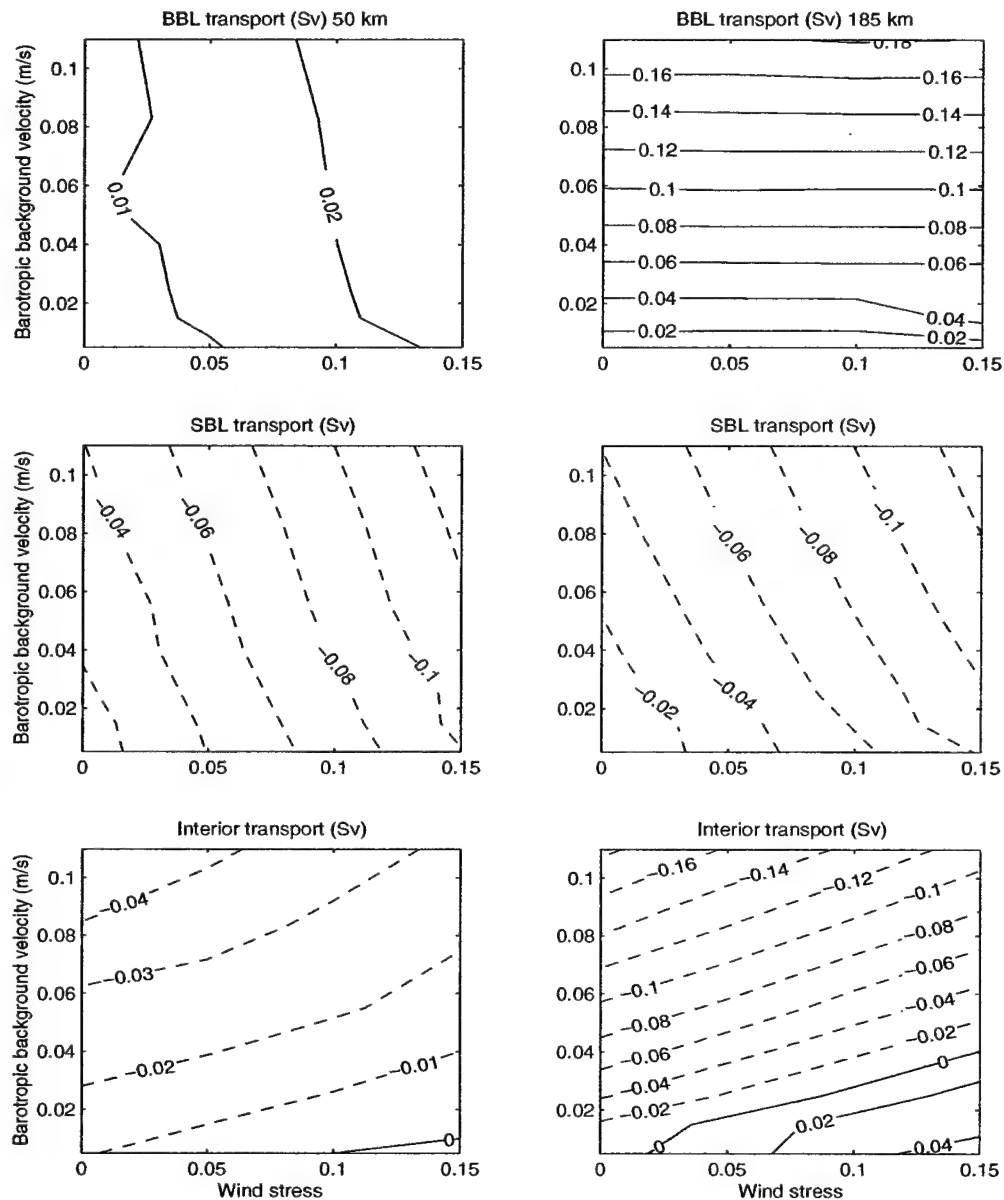
Figure 2-26: The cross shelf transports integrated from 150 to 250 kilometers downstream at 50 kilometers offshore (left) and at 185 kilometers offshore (right). The surface boundary layer (SBL) transport is defined as the transport in the region within 2δ of the air-water interface; the bottom boundary layer (BBL) transport is defined as the transport in the region within 2δ of the bottom; the interior transport is the transport of the water in between the two boundary layers. Dashed contours indicated negative values (shoreward) and solid contours indicate positive contours (offshore). All transports are in Sverdrups.

wind stress is due to the barotropic velocity that the model generates in the shallow water. Offshore, the transport is clearly dominated by the strength of the barotropic current: the larger the barotropic current, the higher the offshore transport of water in the bottom boundary layer. The wind stress is not a significant factor.

The interior transport cross shelf transport at 185 kilometers offshore is consistent with the behavior of the position of the front. For large barotropic inflows, the transport is always shoreward, thereby pushing the front into shallower water. However, for small barotropic inflows and large winds, the interior transport is actually offshore, pulling the front away from the shore and into deeper water. The interior transport 50 kilometers offshore is similar but it is smaller.

Because the wind stress applied to the model domain is spatially homogeneous, the surface boundary layer transport, both shoreward and offshore of the front, is unaffected by the position of the transport measurement. The surface boundary layer transport is always shoreward, to the right of the wind and the stronger the wind, the larger the shoreward flux of water. The wind driven cross shelf transport is independent of the barotropic inflow, however the stronger the barotropic inflow, the larger the cross shelf interior return flow. The interior return flow is barotropic and it includes transport in the surface boundary layer. Because the surface boundary layer transport is the sum of both the wind driven transport and the interior return flow, as the barotropic velocity increases, the surface boundary layer transport also increases.

2.7   Discussion and conclusions

This chapter examines the behavior of a bottom trapped front forced by wind and/or a barotropic inflow. Both the wind and the barotropic inflow alter the Ekman layers in the model. The wind generates a surface Ekman layer with shoreward transport and the barotropic inflow generates a bottom Ekman layer with offshore transport.

The Ekman transport affects the front in two significant ways addressed in this study: it alters the mixed layer structure of the front and it changes the cross-shelf location of the front.

In the boundary layers, both the surface and bottom Ekman transports create density inversions which lead to convective mixing. The cross shelf advection of density by the Ekman layers is balanced by the along shelf advection of density in the boundary layer creating the mixed layers observed in the front. The mixed layers increase in thickness downstream until they are sufficiently thick that they come in contact. Scalings are developed which predict the thickness of the mixed layers. When the mixed layers are in contact, the isopycnals are vertical.

The bottom mixed layer thickness scaling developed fails when the wind stress is very large and the barotropic inflow is small. When this happens, a region of upstream transport under the front and at the offshore model boundary develops. The upstream transport under the front drives a shoreward transport in the bottom Ekman layer which restratifies the density at the bottom. While a mixed region persists in the interior, it no longer extends to the bottom. In general, this scaling fails when the dominant vertical mixing in the boundary layer is given by the mixing scheme, rather than convective mixing.

Previous work with surface trapped fronts (R. Hetland, personal communication, Fong and Geyer (2002)) shows that when light water enters the domain, it develops a surface bulge near the inflow before the water is advected in the direction of Kelvin wave propagation. The vertical thickness of the bulge has a rather complex scaling, but is independent of the wind stress imposed on the domain. The results of this study find that the surface mixed layer thickness is dependent on the magnitude of the wind stress. Likewise the bottom mixed layer thickness is dependent on the magnitude of the bottom stress.

The cross shelf mass flux created by the Ekman layers is mostly balanced by an interior cross shelf mass flux. This is particularly evident offshore. The surface Ekman

113

layer has a shoreward transport and if the wind stress is dominant, the interior flow offshore of the front is offshore and it pulls the front into deeper water; the bottom Ekman layer has an offshore transport and if the barotropic inflow is dominant, the interior return flow is shoreward and pushes the front into shallower water.

In this study, the wind stress generates a downstream barotropic transport in shallow water and to conserve mass an upstream transport develops at the offshore wall. It is clear that this upstream jet is rather close to the front and is playing a significant role on the behavior of the front. The convergence of water into the jet pulls the front offshore. It is not clear how the behavior of the front would change if the mass return from the wind driven barotropic current was significantly separated from the front.

This study explores the parameter space of wind stress and barotropic inflow for the location of the front. The frontal location is predominantly controlled by the barotropic inflow but there is also a weaker dependence on the wind stress. While it is likely that the barotropic inflow results are robust, it is less clear that the wind stress results are definitive because of the finite width of the model domain.

The wind is a homogeneous forcing on the model domain: it is equal shoreward and offshore of the front. The along-shelf barotropic velocity, however, creates stronger stresses in deeper water than in shallower water because of the adjustment of the barotropic current over a sloping bottom. The dominance of the barotropic velocity over the wind stress in determining the frontal location may be due to the concentrated effect of the barotropic inflow in deeper water.

The momentum balance in the along shore direction of the interior region is geostrophic: the cross shelf transport of water is driven by an along shore pressure gradient. Chapman and Lentz (1994) found this pressure gradient and subsequent cross shelf transport displacing the front shoreward in their experiments. The cross shelf transport in this study occurs both in a shoreward and offshore direction, depending on the values of wind stress and barotropic inflow.

114

Chapter 3

Buoyant shelf currents with "ice"

3.1 Introduction

Global climate system models such as Boville and Gent (1997) and regional models of
the Arctic Ocean such as Hibler and Bryan (1987), Semtner (1987), and Oberhuber
(1993) often fail to resolve fine scale features such as shelf currents. At high latitudes
shelf currents transport a significant amount of heat and mass (Mauritzen, 1996a,b)
and are often closely related to the western boundary current of the basin. (Legutke,
1991 and Woodgate et al., 1999) As discussed in chapter 1, it is possible that problems
in the coarse resolution models may be traced to the failure to resolve these features.

Simply increasing the resolution of the GCMs is not the only answer to the prob-
lem. While all of the dynamics discussed in this chapter would certainly be present in
a high resolution GCM, the calculation times required to study the small scale dynam-
ics would be prohibitive. There is a great deal that is currently not understood about
how shelf currents behave and how they interact with their environment. In partic-
ular, cold equator-ward flowing shelf currents such as the East Greenland Current
and the Labrador current are often at least partially covered by sea ice. Dynamic
ice-ocean interactions are not completely understood at this point, particularly on
small spatial scales. It is difficult enough to understand ocean-only GCMs; coupling

an ice model into the system increases the complexity significantly.

Roed and O'Brien (1983) examined the interaction of the ice edge with a stratified ocean. They created a 1.5 layer coupled ice-ocean model and blew wind over the domain, parallel to the ice edge. Because the ice-air drag coefficient is larger than the water-air drag coefficient, there is divergent Ekman transport at the ice edge. Mass is conserved by the development of an upwelling region near the divergence. Their study is followed by Hakkinen (1986). She expanded their model to two dimensions. The upwelling at the ice edge leads to doming of the isopycnals, driving a geographically balanced jet the ice edge. She examined the stability of the ice edge jet under both steady and fluctuating wind (similar to a storm) and found that both the ice edge jet and the shape of the ice edge itself are unstable. The instability has a growth rate of 3-5 days in upwelling favorable conditions.

The ice model used in these studies is coupled to a 1.5 layer ocean model and can only be used to study small variations in ocean layer thickness. Shelf currents are associated with large variations in layer thickness, often with the front outcropping. A different method is needed to study shelf currents.

In a series of papers (Ikeda 1988, 1991 and Ikeda et al, 1996), a coupled ice-ocean model for studying the regional dynamics of the Labrador current was developed. The ocean component is a z coordinate model with 1 to 6 layers - a rather inadequate resolution for the shelf break. The ice component is simplified from Hibler (1979) and has rudimentary thermodynamics. In the Ikeda papers, the development of the jet associated with the ice edge upwelling of Roed and O'Brien (1983) is observed in a more complex model.

Observationally, there are little data examining the interaction between sea ice and underlying shelf currents. Emphasis of sections of the Greenland Sea or other partially ice covered basins often focuses on the properties of the ice free regions. Sections are commonly ended at the ice edge, well short of the shelf break, unless expensive ice breakers are used.

116

In 1979, 1983 and 1984, an extensive field observation program was carried out known collectively as the Marginal Ice Zone experiments, or MIZEX (J.A. Johannessen et al. 1983 and J.A. Johannessen et al. 1987). The thrust of these experiments was on the ice edge and not on the interaction with the East Greenland current. They create a fairly comprehensive picture of the behavior of the ice edge and the underlying ocean but the field area is too far east to sample the East Greenland Current.

Aagaard and Greisman (1975) used methods that conserved heat and fresh water in the Greenland-Iceland-Norwegian sea areas and they argue that the ice speed is faster than the water speed in the East Greenland Current. Drifters on the ice and in the water support the ice moving approximately twice as fast as the water. The ice moves faster than the water which is in contrast to the Canadian basin in the Arctic Ocean where the ice and water move at approximately the same speed. The large ice drift is attributed to high wind stress in the region.

This study concentrates on the dynamic ice-ocean coupling with along ice edge winds. It ignores the complex issues related to ice thermodynamics. Ice thermodynamics certainly play a first-order role in the integrated ice-ocean system. It is a complex system and it is not clear how much progress can be made without understanding the simple underlying dynamics first.

In this chapter, the behavior of the sea-ice when it is forced by an underlying ocean current, wind, or both is studied. Only cases where the wind and ice transports are parallel are considered. A simple one dimensional ice-ocean coupled model is used, similar to the model used in Roed and O'Brien (1983). The results are consistent with Aagaard and Greisman (1975): the transport of ice is with the wind and/or current and the ice transport perpendicular to the wind or current is very small. When there is only a current and no wind, the ice travels with the geostrophic current, at the same speed. When there is wind, the ice and the ocean form a two layer Ekman spiral and because the mass of ice is much less than the mass of the water, the ice transport

117

is mostly parallel to the wind while the ocean transport is perpendicular to the wind. As discussed in the previous chapter, the wind will spin up a barotropic geostrophic current in the ocean and that current enhances the downwind transport of ice.

In section 3.2, the ice dynamic equations are discussed and the toy model is developed. The remainder of the chapter discusses the behavior of ice when there is wind (section 3.3), when there is a geostrophic current (section 3.4) and when there is both a wind and a current (section 3.5). The chapter is summarized and discussed in section 3.6.

3.2   Ice dynamic equations

Sea ice moves in a two-dimensional plane, forced by the planetary boundary layer from above and the ocean from below (Hibler, 1979). Below is a short synopsis of the ice momentum, mass and compactness conservation equations that constitute the dynamic ice model. For a more complete treatment the reader is referred to Hibler (1979).

The momentum balance for sea ice is given by

$$m\frac{D\vec{u}_i}{Dt} = -mf\hat{k} \times \vec{u}_i + A(\vec{\tau_{ai}} + \vec{\tau_{wi}}) - mg\nabla H + \vec{F}_i \qquad (3.1)$$

where $\frac{D}{Dt} = \frac{\partial}{\partial t} + u\frac{\partial}{\partial x} + v\frac{\partial}{\partial y}$ is the substantial time derivative, $\hat{k}$ is the unit vector normal to the surface, $\vec{u}_i$ is the ice velocity, f is the Coriolis parameter, $m = \rho_i AD$ is the ice mass per unit area with A the fractional ice concentration or ice compactness; ρ_i the ice density and D the ice thickness. The surface stresses are: $\vec{\tau_{ai}}$, the force due to stress caused by the atmosphere on the ice and $\vec{\tau_{wi}}$, the force due to stress caused by the water on the ice. The magnitude of the stresses are weighted by the ice concentration[1]. The acceleration due to gravity is g; H is the ocean dynamic height

---

[1]This is a slightly different treatment than Hibler (1979) because Hibler chose to develop the stresses in a different manner than is done in this study.

118

and $\vec{F_i}$ are the forces due to internal ice stresses.

There are two additional conservation equations. One conserves ice mass and the other conserves ice compactness where ice compactness has been defined as the fraction of ocean covered by ice. The conservation of ice mass takes the form

$$\frac{\partial m}{\partial t} + \frac{\partial (mu_i)}{\partial x} + \frac{\partial (mv_i)}{\partial y} = S_m + \mathcal{D} \tag{3.2}$$

where S_m represents a thermodynamic source or sink and $\mathcal{D}$ is diffusion. In addition, a continuity equation can be derived to conserve ice compactness, A

$$\frac{\partial A}{\partial t} + \frac{\partial (Au_i)}{\partial x} + \frac{\partial (Av_i)}{\partial y} = S_A + \mathcal{D} \tag{3.3}$$

where S_A is an additional thermodynamic term and $0 \leq A \leq 1$. When $A = 1$ the ocean is ice covered and when $A = 0$ the ocean is ice free.

Ice is dynamically coupled with the ocean by modifying the surface stress term on the ocean, $\vec{\tau_s}$ to account for partial ice coverage (Roed and O'Brien, 1983). $\vec{\tau_s}$ becomes

$$\vec{\tau_s} = (1 - A)\vec{\tau}_{aw} - A\vec{\tau}_{wi} \tag{3.4}$$

The stresses are parameterized with a quadratic drag law:
the air-water stress

$$\vec{\tau}_{aw} = \rho_{air} C_{aw} |\vec{U}_{air} - \vec{u_w}|(\vec{U}_{air} - \vec{u_w}) \approx \rho_{air} C_{aw} |\vec{U}_{air}|\vec{U}_{air} \tag{3.5}$$

the air-ice stress

$$\vec{\tau}_{ai} = \rho_{air} C_{ai} |\vec{U}_{air} - \vec{u_i}|(\vec{U}_{air} - \vec{u_i}) \approx \rho_{air} C_{ai} |\vec{U}_{air}|\vec{U}_{air} \tag{3.6}$$

the water-ice stress

$$\vec{\tau}_{wi} = \rho_i C_{wi} |\vec{u_i} - \vec{u_w}|(\vec{u_w} - \vec{u_i}) \tag{3.7}$$

119

where C_{aw} is the air-water drag coefficient, C_{ai} the air-ice drag coefficient and C_{wi} the ice-water drag coefficient. C_{aw} is defined in chapter 2 as $1.4 \cdot 10^{-3}$. Estimates of C_{ai} and C_{wi} vary but are both considerably larger than C_{aw} because of the substantial surface roughness found on both sides of sea ice floes. In this study, C_{ai} is set at $3.2 \cdot 10^{-3}$ and C_{wi} is set at $1.0 \cdot 10^{-2}$, as was used in Hakkinen (1986)[2]. The approximations for $\vec{\tau}_{aw}$ and $\vec{\tau}_{ai}$ are used. If there is no wind, the stress between the atmosphere and ice or ocean is zero.

The sea surface tilt term is $-mg\nabla H$. The geostrophic ocean velocity is related to the sea surface tilt by

$$\vec{u_g} = \frac{g}{f}\hat{k} \times \nabla H \tag{3.8}$$

From vector algebra, it can be shown that

$$-mg\nabla H = mf\hat{k} \times \vec{u_g} \tag{3.9}$$

Equation 3.1 is then:

$$m\frac{D\vec{u_i}}{Dt} = mf\hat{k} \times (\vec{u_g} - \vec{u_i}) + A(\vec{\tau_{ai}} + \vec{\tau_{wi}}) + \vec{F_i} \tag{3.10}$$

Hibler (1979) develops expressions for the thermodynamic coupling terms, S_m and S_A, as well as a constitutive law for calculating the internal ice stresses, $\vec{F_i}$ based on the work of Maykut and Untersteiner (1971), Rothrock et al. (1975) and Maykut (1978). Other studies such as Parkinson and Washington (1979), Hibler and Bryan (1987), Semtner (1987) and Piacsek et al. (1991) have improved on his original formulations to make both components of the ice model more realistic. Overland et al. (1995) has developed a hierarchical categorization of ice dynamics. Flato and Hibler (1990 and

---

[2]Hakkinen (1986) conducted a review of the observed drag coefficients and decided these values were reasonable for the marginal ice zone region. While there has been considerable effort put into estimating these coefficients, the results of this model are robust for a wide range of the parameters. The experimental runs supporting this are not discussed, but in general, so long as $C_{aw} < C_{ai} < C_{wi}$, the ice-ocean system behavior is consistent.

1992) and Zhang and Hibler (1996) investigate different ice rheologies and Holland et al. (1993) have done a fairly comprehensive study of sensitivities of ice models. However, while these developments are important to the general GCM efforts, they represent complications that can be neglected for the marginal ice zone of the East Greenland Current. In this study the internal ice stresses are neglected.

The ocean equations (2.1-2.5) with the ice equations (3.1-3.3) form a nonlinear, dynamic system, coupled through interfacial stresses and fluxes. The surface stress on the ocean is modified to reflect a partial ice coverage and it becomes a weighted average between the air-water stress and the ice-water stress.

$$\vec{\mathcal{F}} = (1 - A)\vec{\tau_{aw}} + A\vec{\tau_{wi}}$$

In this study, a simplification to the very complex ice-ocean system is examined.

One of the simplifications this study uses is that the ocean is depth averaged over the Ekman layer and coupled to the ice through the ice-water stress. The ice-water stress is proportional to the difference in the ice velocity with the surface ocean velocity, not the depth averaged ocean velocity. To account for the difference between the surface velocity of the water and the depth averaged velocity, an ad hoc "turning angle" is typically applied to the stresses. In an effort to focus on the fundamental dynamics, the turning angle is not used in this study.

3.2.1 Scaling

Scaling analysis is performed on the ice and ocean momentum equations to determine the significant terms. Hibler (1979) points out that the internal ice stress is particularly important when there are walls or barriers, such as a coastline. In the open ocean or near the marginal ice zone, the internal ice stress has a negligible effect. Roed and O'Brien (1983) examine the role of the internal ice stress terms in the marginal ice zone and find that their primary impact is to increase the gradient of ice

concentration at the ice edge. The ice momentum equations written on an f-plane, neglecting the internal ice stresses and incorporating the tilt term into the Coriolis term, are

$$\frac{D\vec{u_i}}{Dt} = -f_0\hat{k} \times (\vec{u_i} - \vec{u_g}) + \frac{A\vec{\tau_{ai}}}{m} + \frac{A\vec{\tau_{wi}}}{m} \tag{3.11}$$

As with the ocean momentum equations, the surface stresses are weighted by the ice concentration in this treatment.

The ocean momentum equations, averaged over the Ekman layer are

$$\frac{D\vec{u_w}}{Dt} = -f_0\hat{k} \times \vec{u_w} - g\nabla H + \frac{(1-A)\vec{\tau_{aw}}}{\rho_o\delta} - \frac{A\vec{\tau_{wi}}}{\rho_o\delta} \tag{3.12}$$

where δ is the Ekman layer thickness. The ice and water velocities are expanded into geostrophic and ageostrophic components

$$\vec{u_w} = \vec{u_g} + \vec{u_{ag}} \tag{3.13}$$

$$\vec{u_i} = \vec{u_g} + \vec{u_{ai}} \tag{3.14}$$

where

$$f_0\hat{k} \times \vec{u_g} = -g\nabla H \tag{3.15}$$

In this section, linearity is assumed and the discussion focuses on the steady state of the system allowing the substantial derivative to be neglected. The scaling of the substantial derivative is discussed in section 3.2.3 after the model has been presented. The steady ice and ocean ageostrophic momentum equations, respectively, are

$$0 = -f_0\hat{k} \times \vec{u_{ai}} + \frac{A\vec{\tau_{ai}}}{m} + \frac{A}{m}C_{wi}\rho_i|\vec{u_{ag}} - \vec{u_{ai}}|(\vec{u_{ag}} - \vec{u_{ai}}) \tag{3.16}$$

$$0 = -f_0\hat{k} \times \vec{u_{ag}} + \frac{(1-A)\vec{\tau_{aw}}}{\rho_o\delta} - \frac{A}{\rho_o\delta}C_{wi}\rho_i|\vec{u_{ag}} - \vec{u_{ai}}|(\vec{u_{ag}} - \vec{u_{ai}}) \tag{3.17}$$

The variables are scaled as follows

$$
\begin{aligned}
\vec{u_{ai}} &= u^* \vec{u'_{ai}} \\
\vec{u_{ag}} &= u^* \vec{u'_{ag}}
\end{aligned}
\tag{3.18}
$$

where u^* is

$$
u^* = \sqrt{\frac{(1-A)|\vec{\tau_{aw}}| + A|\vec{\tau_{ai}}|}{\rho_o}}
$$

The ratio of the magnitudes of the air-water stress to the air-ice stress is

$$
\frac{\tau_{aw}}{\tau_{ai}} = \frac{C_{aw}}{C_{ai}}
$$

Using the ratio of the stresses and the definition of u^*, the magnitudes of the surface stresses can be written as

$$
\begin{aligned}
\tau_{aw} &= \frac{u_*^2 \rho_o}{\left[(1-A) + A\frac{C_{ai}}{C_{aw}}\right]} \\
\tau_{ai} &= \frac{u_*^2 \rho_o}{\left[(1-A)\frac{C_{aw}}{C_{ai}} + A\right]}
\end{aligned}
$$

Substituting these scales into the ice and ocean momentum equations (3.16 and 3.17, respectively) and dividing both equations by $f_0 u^*$, the coefficient of the Coriolis term, they are non-dimensionalized to

$$
0 = -\hat{k} \times \vec{u'_{ai}} + \frac{\rho_o \frac{u^*}{f_0}}{\rho_i \, D}\left[\frac{1}{\frac{C_{aw}}{C_{ai}} - A(\frac{C_{aw}}{C_{ai}} - 1)}\right] + C_{wi}\frac{\frac{u^*}{f_0}}{D}|\vec{u'_{ag}} - \vec{u'_{ai}}|(\vec{u'_{ag}} - \vec{u'_{ai}}) \tag{3.19}
$$

$$
0 = -\hat{k} \times \vec{u'_{ag}} + \frac{u^*}{f_0\delta}\left[\frac{1-A}{1 - A(1 - \frac{C_{ai}}{C_{aw}})}\right] - AC_{wi}\frac{\rho_i}{\rho_o}\frac{u^*}{f_0\delta}|\vec{u'_{ag}} - \vec{u'_{ai}}|(\vec{u'_{ag}} - \vec{u'_{ag}}) \tag{3.20}
$$

In the limit where $A \to 0$, i.e. when there is no ice, the first two terms in equation 3.20 balance. When the Coriolis term is balanced by the stress, the system is in Ekman balance. This implies that the ratio of the Coriolis force to the stress, the Ekman number, $\frac{u^*}{f_0\delta}$, is order one. This allows the Ekman depth to be defined

123

as $\delta = \frac{u^*}{f_0}$. Using this definition of the Ekman number, the scaled equations can be simplified

$$0 = -\hat{k} \times \vec{u_{ai}} + \frac{\rho_o}{\rho_i} \frac{\delta}{D} \left[\frac{1}{\frac{C_{aw}}{C_{ai}} - A(\frac{C_{aw}}{C_{ai}} - 1)} \right] + C_{wi} \frac{\delta}{D} |\vec{u_{ag}} - \vec{u_{ai}}|(\vec{u_{ag}} - \vec{u_{ai}}) \quad (3.21)$$

$$0 = -\hat{k} \times \vec{u_{ag}} + \left[\frac{1 - A}{1 - A(1 - \frac{C_{ai}}{C_{aw}})} \right] - AC_{wi} \frac{\rho_i}{\rho_o} |\vec{u_{ag}} - \vec{u_{ai}}|(\vec{u_{ag}} - \vec{u_{ai}}) \quad (3.22)$$

In the limit where $A \to 1$, i.e. when there is complete ice cover, the air-ice stress is balanced by both the Coriolis force and the ice-water stress. In the ocean, the ice-water stress is balanced by the Coriolis force because there is no water exposed to the atmosphere.

The steady ageostrophic equations are an Ekman balance with a net transport of mass perpendicular to the wind. The net transport of water and ice in the direction of the wind is 0, but the ice and ocean have equal and opposite downstream transports. By decomposing the water and ice velocity into geostrophic and ageostrophic parts, however, the balance in the along stream direction of the ice is somewhat obfuscated. In the along stream direction in the ice, there is a balance between the tilt term and the ice velocity. Thus, when the water is moving under the ice, the ice has a geostrophic velocity equal to the water's geostrophic velocity.

3.2.2 The toy model

For studying dynamic ice-ocean coupled interactions, a horizontal one dimensional model, similar to Roed and O'Brien (1983), is constructed. The model is defined along a line rotating with angular velocity $f_0/2$, where f_0 is the Coriolis parameter evaluated at 75° N. The model domain is oriented in the y direction. There is velocity in the x direction but gradients in the x direction are neglected. There are open boundaries at both extremes of the domain. This study concentrates on the ice-ocean dynamics without considering thermodynamic processes. A cartoon of the model is shown in
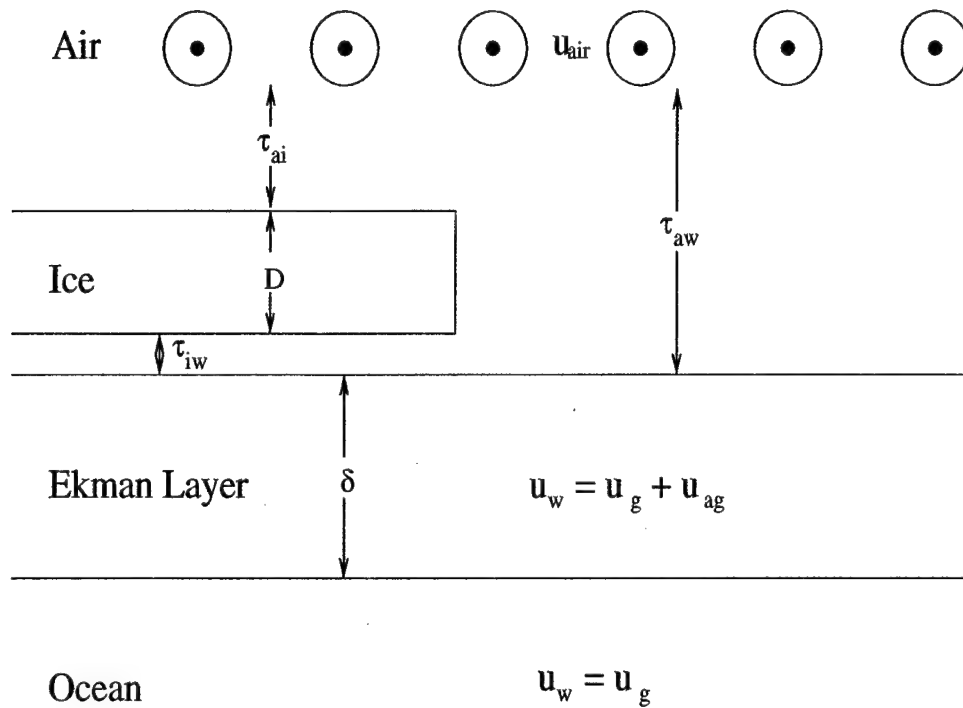
Figure 3-1: A cartoon of the toy model.

figure 3-1.

This study focuses on the ice-ocean dynamics in regions of loosely packed ice over time scales of days to weeks. Because the internal ice stress terms are neglected, it is unlikely that regions of high ice concentration ($A \approx 1$) with convergent ice advection are well represented. Without ice thermodynamics, the only way for ice thickness to increase is through ridging. Ridging happens in regions of high ice concentration with convergent advection of ice. This model does not adequately resolve that process and it is assumed the ice maintains a constant thickness of $D = 1$ m. While this would be a problematic assumption within the ice pack of the Arctic Ocean, near the marginal ice zone, in a region dominated by mostly first year ice, it is reasonable. A number of experiments with the ice thickness, D, set to a range of values, revealed that the behavior of the ice-ocean system is unaffected by small variations in the ice thickness. It is only when the ice thickness is sufficiently large that the ice mass is comparable to the water mass that the dynamics are affected by the ice thickness.

125

Unlike in the scaling, the ice velocity is not decomposed into geostrophic and ageostrophic parts. During the analysis it will occasionally be useful to distinguish between the geostrophic and ageostrophic velocities but for the model the total ice velocity is calculated because this study is interested in the response of the ice to wind and underlying currents combined. Once these simplifications have been made, the ice equations (3.10) become (Roed and O'Brien, 1983)

$$\frac{\partial u_i}{\partial t} = f_0 v_i - v_i \frac{\partial u_i}{\partial y} + \frac{(\tau_{ai}^x + \tau_{wi}^x)}{\rho_i D} \tag{3.23}$$

$$\frac{\partial v_i}{\partial t} = f_0(u_g - u_i) - v_i \frac{\partial v_i}{\partial y} + \frac{(\tau_{ai}^y + \tau_{wi}^y)}{\rho_i D} \tag{3.24}$$

with the conservation equation

$$\frac{\partial A}{\partial t} = -\frac{\partial (v_i A)}{\partial y} + K_H \frac{\partial^2 A}{\partial y^2} + K(A) \frac{\partial^2 A}{\partial y^2} \tag{3.25}$$

$K_H \frac{\partial^2 A}{\partial y^2}$ is an ad hoc diffusion term and K_H is chosen to be as small as possible for each experiment. $K(A) \frac{\partial^2 A}{\partial y^2}$ is an additional diffusion term where the diffusion coefficient, $K(A)$ is a function of the ice concentration.[3] Figure 3-2 shows a plot of its distribution. This term is negligible except when $A > 0.95$. It prevents excessive ice concentration build up that may occur when the internal ice stress terms are neglected.

The ocean velocity is decomposed into geostrophic and ageostrophic components (equation 3.13) and the geostrophic transport in the Ekman layer is calculated from thermal wind

$$\hat{k} \times \vec{u_g} = \frac{g\delta}{2\rho_o f_0} \nabla \rho$$

---

[3]In full ice models, when the numerical value of the ice concentration exceeds 1, the excess ice is redistributed in the surrounding grid cells. This accomplishes the same goal.
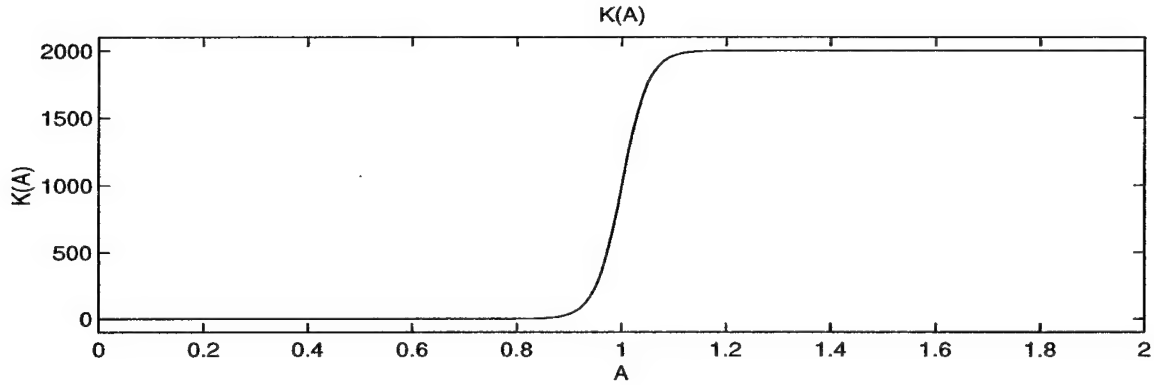
Figure 3-2: $K(A)$ vs. A

The equations for the ageostrophic velocity are

$$\frac{\partial u_w}{\partial t} = f_0 v_{ag} - v_w \frac{\partial u_w}{\partial y} + \frac{(1-A)\tau_{aw}^x - A\tau_{wi}^x}{\rho_o \delta} + A_H \frac{\partial^2 u_w}{\partial y^2} \qquad (3.26)$$

$$\frac{\partial v_{ag}}{\partial t} = -f_0 u_{ag} - v_w \frac{\partial v_w}{\partial y} + \frac{(1-A)\tau_{aw}^y - A\tau_{wi}^y}{\rho_o \delta} + A_H \frac{\partial^2 v_w}{\partial y^2} \qquad (3.27)$$

where δ is the Ekman layer thickness.[4] Its value is 17 m, as used in chapter 2. The ocean conservation of mass equation is averaged over the Ekman thickness, δ and it is written as

$$\frac{\partial \rho}{\partial t} = -v_w \frac{\partial \rho}{\partial y} + K_H \frac{\partial^2 \rho}{\partial y^2} \qquad (3.28)$$

$A_H \frac{\partial^2 \vec{u_w}}{\partial y^2}$ adds diffusion to the momentum equation and A_H is chosen to be as small as possible in each experiment. The diffusion of density is the same as it is in the ice equations. The diffusion of both the ice and the density are used to reduce the inertial oscillations in the model. The inertial oscillations are generated during the adjustment of the ice to the ocean's geostrophic velocity. They are present in all experiments and

---

[4]Immediately under sea-ice there is typically a layer of cold, fresh water that isolates the sea-ice from the warmer, saltier ocean interior water. This water is formed by thermodynamic processes as the ice melts and freezes. The thickness of this layer varies but it is typically of the same scale as the Ekman layer thickness: 10-20 meters. Many sections show this feature and in the East Greenland current, some examples include MIZEX sections Johannessen et al. (1983), Wadhams and Squire (1983), and Muench et al. (1983) and independent sections Morison et al. (1987), McPhee et al. (1987) and Foldvik et al. (1988).

127

are discussed in detail in section 3.4. Averaging the momentum equations over the Ekman layer assumes stress is applied to a slab of ocean of thickness δ. The vertical structure associated with the Ekman layer is not resolved in this model.

The ice and ocean are coupled through the interfacial stresses, defined in equations 3.5, 3.6 and 3.7. The water velocity, $\vec{u_w}$, used in the ice-ocean stress is the sum of the geostrophic velocity, $\vec{u_g}$, and the ageostrophic velocity, $\vec{u_{ag}}$. For the purpose of this study, the geostrophic velocity is always in the $+x$ direction and $v_g = 0$. u_g is prescribed and is defined as the sum of a spatially homogeneous component and a jet calculated to be in thermal wind balance with the front. The spatially constant part either represents the background "barotropic" velocity driven by the wind, or a remotely driven "barotropic" current. If it is meant to be consistent with the wind, it is calculated from equation 2.40, otherwise an arbitrary value is imposed.

The model is created in MATLAB utilizing its ODE solving routines. Typically A is initialized to include the ice edge and ρ is initialized to include a front. The geostrophic velocity is calculated from ρ and the appropriate background velocity for the experiment. All four velocity components (u_i, v_i, u_{ag} and v_{ag}) are initialized at zero throughout the domain.[5] If wind is imposed, the wind speed and the associated geostrophic background current are ramped up over several days at the start of the run. Turning the wind on gradually reduces, but does not eliminate, inertial oscillations in the system. The model is run for the duration of the experiment, ranging from a few days to several hundred days.

3.2.3 Scaling of the substantial derivative for the toy model

In section 3.2.1, scaling for the right hand side of the ice and ocean momentum equations is developed. In this section, scaling of the left hand side of the momentum

---

[5]Additional experiments were done setting the initial ice velocity equal to the initial geostrophic velocity. In this case, the interfacial stress is initially zero and the Coriolis term balances the time tendency. Quickly the ice velocity changes away from the initial condition and the interfacial stress grows. After about a day, the two different initial conditions converge to a single solution.

equations is discussed. The scaling discussed in this section assumes that the ice-ocean system is one dimensional with spatial derivatives only in the y direction and it is assumed that the geostrophic velocity is all in the x direction. The equations for the water will be worked out but they are the same for the ice.

The substantial derivative is

$$
\begin{aligned}
\frac{D\vec{u_w}}{Dt} &= \frac{D}{Dt}\left(\vec{u_g} + \vec{u_{ag}}\right) \\
&= \frac{\partial}{\partial t}\left(\vec{u_g} + \vec{u_{ag}}\right) + \left(\vec{u_g} + \vec{u_{ag}}\right) \cdot \nabla \left(\vec{u_g} + \vec{u_{ag}}\right) \\
&= \frac{\partial}{\partial t}\left(\vec{u_g} + \vec{u_{ag}}\right) + \vec{u_{ag}} \cdot \nabla\vec{u_{ag}} + \vec{u_g} \cdot \nabla\vec{u_{ag}} + \vec{u_{ag}} \cdot \nabla\vec{u_g} + \vec{u_g} \cdot \nabla\vec{u_g}
\end{aligned}
\tag{3.29}
$$

Because $v_g = 0$ in this model and $\frac{\partial}{\partial x} \to 0$, many terms in the advection portion of the substantial derivative are eliminated. Equation 3.29 reduces to

$$
\frac{D\vec{u_w}}{Dt} = \left[\frac{\partial}{\partial t}\left(u_g + u_{ag}\right) + v_{ag}\frac{\partial}{\partial y}\left(u_g + u_{ag}\right)\right]\hat{i} + \left[\frac{\partial v_{ag}}{\partial t} + v_{ag}\frac{\partial v_{ag}}{\partial y}\right]\hat{j}
\tag{3.30}
$$

The variables are non-dimensionalized as follows

$$
\begin{aligned}
\frac{\partial}{\partial t} &\approx \frac{1}{T}\frac{\partial}{\partial t'} \\
\frac{\partial}{\partial y} &\approx \frac{1}{L}\frac{\partial}{\partial y'} \\
u_g &\approx U u_g \\
\vec{u_{ag}} &\approx u^*\vec{u_{ag}'}
\end{aligned}
\tag{3.31}
$$

where U, the scale for the geostrophic velocity is taken from the thermal wind expression

$$
U = \frac{g}{f_0 L}\frac{\Delta\rho}{\rho_o}\delta
$$

and u^*, the scale for the ageostrophic velocity is

$$
u^* = \sqrt{\frac{\tau}{\rho_o}}
$$

129

The length scale, L, is chosen to be the width of the front in the model, at the initial condition. The time scale, T, is discussed as it is applied throughout the chapter. When the scales listed in 3.31 are applied to the substantial derivative, equation 3.30, it becomes

$$
\frac{D\vec{u_w}}{Dt} = \frac{U}{T} \Big[\Big[\frac{\partial}{\partial t'} \Big(u'_g + \frac{u^*}{U} u'_{ag} \Big) + \frac{u^*}{L/T} v_{ag} \frac{\partial}{\partial y} \Big(u_g + \frac{u^*}{U} u_{ag} \Big) \Big] \hat{i}
$$
$$
+ \Big[\frac{u^*}{U} \frac{\partial v_{ag}}{\partial t} + \frac{u^*}{U} \frac{u^*}{L/T} v_{ag} \frac{\partial v_{ag}}{\partial y} \Big] \hat{j} \,] \tag{3.32}
$$

The non-dimensional ratio $\frac{u^*}{L/T}$ is similar to the Rossby number if $\frac{1}{T} = f_0$. The ratio $\frac{u^*}{U}$ is the ratio of the ageostrophic velocity to the geostrophic velocity. At this point, the entire equation is still dimensional. It will be non-dimensionalized when it is used, below.

3.2.4 The momentum balance equations

Plots of the balances within the momentum and density equations illustrate the dynamic balance of the terms and will be used throughout this chapter. In this section, the balance plots are described.

The model momentum equations, 3.23, 3.24, 3.26 and 3.27, respectively, are rewritten as:

	time tendency	Coriolis force	tilt term	air stress	$i - w$ stress
ice x	$0 = -m\frac{\partial u_i}{\partial t}$	$+mf_0 v_i$		$+A\tau_{ai}^x$	$+A\tau_{wi}^x$
ice y	$0 = -m\frac{\partial v_i}{\partial t}$	$-mf_0 u_i$	$+mf_0 u_g$	$+A\tau_{ai}^y$	$+A\tau_{wi}^y$
water x	$0 = -\rho_o \delta \frac{\partial u_w}{\partial t}$	$+\rho_o \delta f_0 v_{ag}$		$+(1-A)\tau_{aw}^x$	$-A\tau_{wi}^x$
water y	$0 = -\rho_o \delta \frac{\partial v_{ag}}{\partial t}$	$-\rho_o \delta f_0 u_{ag}$		$+(1-A)\tau_{aw}^y$	$-A\tau_{wi}^y$
	dotted	solid	solid dot	dash dot	dashed

(3.33)

130

The ice momentum equations are multiplied by the mass of ice, $m = A\rho_i D$, as in Hibler (1979) and the water momentum equations have been multiplied by the mass of water in the Ekman layer, $\rho_o \delta$. Plots are made showing the value of each term in the momentum equations and the line type used for each term is shown in equations 3.33. The momentum advection and diffusion terms are not shown because they are never significant.

3.2.5 Comparison with Roed and O'Brien (1983)

Roed and O'Brien (1983) developed a coupled 1.5 layer ocean model and simple ice model to study the behavior of the ice edge forced by along ice edge winds. Specifically, they were interested in examining ice edge upwelling associated with divergent Ekman transport at the ice edge.

In their model, the ocean momentum equations are written in transport form. The water in the lower layer of their model is motionless but the surface between the two layers can be deformed by vertical motion associated with divergent transport in the upper layer. Only deformations which are small when compared to the total layer thickness were considered. This configuration is useful for studying the behavior of the ice edge away from strong horizontal gradients in density but it is unable to handle the large variations in density associated with shelfbreak fronts.

The present study focuses on the interaction of the marginal ice zone with a density front and associated jet. The front represents a first order variation in density and the Roed and O'Brien (1983) ocean model cannot be used. In this study, the ocean equations are averaged over the surface Ekman layer and the layer thickness is a constant, equal to the Ekman layer thickness. Vertical motion in the upper layer is diagnostically determined from the ocean continuity equation, as follows. Assuming variations in the downstream direction are negligible and the geostrophic velocity is non-divergent,

$$\frac{\partial v_{ag}}{\partial y} = -\frac{\partial w}{\partial z} \tag{3.34}$$

131

For mass to be balanced, there is vertical motion in the ocean. Assuming a rigid lid at $z=0$, the vertical velocity at the base of the Ekman layer is estimated as

$$w = \delta \frac{\Delta v_{ag}}{\Delta y} \tag{3.35}$$

where δ is the Ekman layer thickness. A useful way to visualize the vertical velocities is to imagine an arbitrary surface placed at the base of the mixed layer that can be deformed by vertical motion in the ocean. The vertical displacement of the surface above or below its initial state is

$$\eta(y,t) = \int_0^t w(y, t')dt' \tag{3.36}$$

In this study, vertical motion does not cause cross stream density gradients in the ocean through "doming" of underlying isopycnals. By neglecting cross stream density gradients caused by the upwelling, geostrophic ice edge jets do not exist in this model. The geostrophic current is entirely due to the density front imposed in the ocean and any barotropic flow diagnosed from the wind. In Roed and O'Brien (1983), one way the ice couples to the ocean is through the geostrophic flow developed by the doming of isopycnals caused by ice edge upwelling. The ice edge upwelling is driven by divergent Ekman transport across the ice edge. The strict definition of the geostrophic flow used in the model in this study eliminates some possible couplings.

3.2.6   Discussion of the toy model

This simple model has several advantages over a more complex system, but it also suffers from real drawbacks. The biggest drawback is that it is one dimensional and while it does allow downstream velocity, it can not be used to study downstream variations. By eliminating the ice rheology and setting the ice thickness to a constant value, the system is both much simpler and much less realistic than real ice. Real ice behaves differently when compressed and this model does not account for that.

Coupling between the vertical motion in the ocean altering the ocean density structure and the behavior of the ice edge are neglected. Because these simplifications have been made, the complex dynamic coupling seen in Hakkinen (1986) is eliminated. Working with depth averaged equations in the ocean removes the reversals in current direction associated with the Ekman spiral. The ageostrophic velocities multiplied by δ, the Ekman layer thickness, provides an estimate of the transport over the Ekman layer, but the model does not resolve the fine structure within the Ekman layer. Because the model is one dimensional and the number of grid points is small, it runs rapidly on just about any computer system.

It is not obvious what the best initial condition is for the system. In the real ocean, ice forms and advects while forced by moving water, wind and thermodynamics. In these experiments, the ice starts with a thickness of 1 m and concentrations greater than 0.5, but its initial velocity is chosen to either be zero or the geostrophic velocity in the ocean. This is equivalent to taking an ocean current and dropping fully formed ice on the surface. While this is not very realistic, considerable experimentation with the toy model revealed that the end results of the experiments are remarkably insensitive to the choice of initial condition. The results presented appear to be robust, even with the less than ideal initial conditions.

3.2.7 Organization

The remainder of the chapter is broken up into three parts. In section 3.3, the interaction of wind and ice in the absence of an underlying ocean current is investigated. These experiments are qualitatively similar to the model presented by Roed and O'Brien (1983). This is followed by a discussion of the ice-ocean dynamics over a current in the absence of wind (section 3.4). Finally, the ice, ocean and wind are brought together and their combined dynamics are discussed in section 3.5.

3.3 Wind and ice with no ocean current

The interaction of wind and ice in the absence of underlying currents are examined first. This configuration of the model is similar to the model used by Roed and O'Brien (1983).

3.3.1 Predictions from scaling

If there are no underlying currents in the ocean, the geostrophic velocity is 0 m/s. Therefore, the water and ice velocities are equal to the ageostrophic velocities or

$$\vec{u_i} = \vec{u_{ai}} = u^*\vec{u'_{ai}} \tag{3.37}$$

$$\vec{u_w} = \vec{u_{ag}} = u^*\vec{u'_{ag}} \tag{3.38}$$

The non-dimensionalized equations, 3.19 and 3.20, restated below, describe the steady response of the ice and ocean.

$$0 = -\hat{k} \times \vec{u'_{ai}} + \frac{\rho_o}{\rho_i}\frac{\delta}{D}\left[\frac{1}{\frac{C_{aw}}{C_{ai}} - A(\frac{C_{aw}}{C_{ai}} - 1)}\right] + C_{wi}\frac{\delta}{D}|\vec{u_{ag}} - \vec{u'_{ai}}|(\vec{u_{ag}} - \vec{u'_{ai}})$$

$$0 = -\hat{k} \times \vec{u'_{ag}} + \left[\frac{1-A}{1 - A(1 - \frac{C_{ai}}{C_{aw}})}\right] - AC_{wi}\frac{\rho_i}{\rho_o}|\vec{u_{ag}} - \vec{u'_{ai}}|(\vec{u_{ag}} - \vec{u'_{ai}})$$

where $\delta = \frac{u^*}{f_0}$.

As discussed in section 3.2.1, in the limit where there is complete ice coverage, the momentum balance in the ice is split between all three terms. The air-ice stress is balanced primarily by the ice-water stress and the ice is accelerated in the direction of the wind and slowed by the drag with the underlying ocean. The remainder of the air-ice stress is balanced by the Coriolis term and this drives a small cross wind transport of ice.

If the ocean is ice covered, the momentum balance in the water is between the ice-water stress and the Coriolis force. This drives a transport of water which is

134

predominantly cross wind, although it has a small up-wind component as well. In the limit where there is no ice coverage, the momentum balance in the ocean is between the air-water stress and the Coriolis force, driving a cross wind transport of water in a classical Ekman layer.

In the absence of an underlying current, the ice-water system behaves as a two level Ekman layer. The upper level (the ice) has a component of velocity downstream and a small velocity to the right of the wind, while lower level (the water) moves nearly entirely to the right of the wind. The downstream mass transport of ice is equal to the upstream mass transport of water. Because the mass of the water is much larger than the ice, there is a small up wind water velocity. The two levels of the model are an extremely poorly resolved Ekman spiral.

3.3.2 Model setup

Roed and O'Brien (1983) explored the interaction between an ice edge and the underlying ocean when wind is blown over the system. They neglected background currents in the ocean entirely. In this section, their experiment is repeated and extended using the toy model.

Because of differences in model formulation, Roed and O'Brien (1983)'s work can not be replicated exactly. The following configuration produces results which are qualitatively similar. The resolution of the toy model is 2 km and the width of the model domain is 300 km. An ice edge is placed 200 km off shore with ice covering $y = 200$ km to $y = 300$ km. The water density is constant throughout the domain. A plot of the initial condition of ice concentration is shown in figure 3-3 as a dotted line. An additional run with the relative position of the ice and water reversed is also done and the initial condition of ice concentration is shown in figure 3-3 as a dash-dot line. The reversed experiment is shown because the rest of the cases discussed in this study have this ice configuration, consistent with the relative orientation of the ice and open water in the East Greenland Current region.
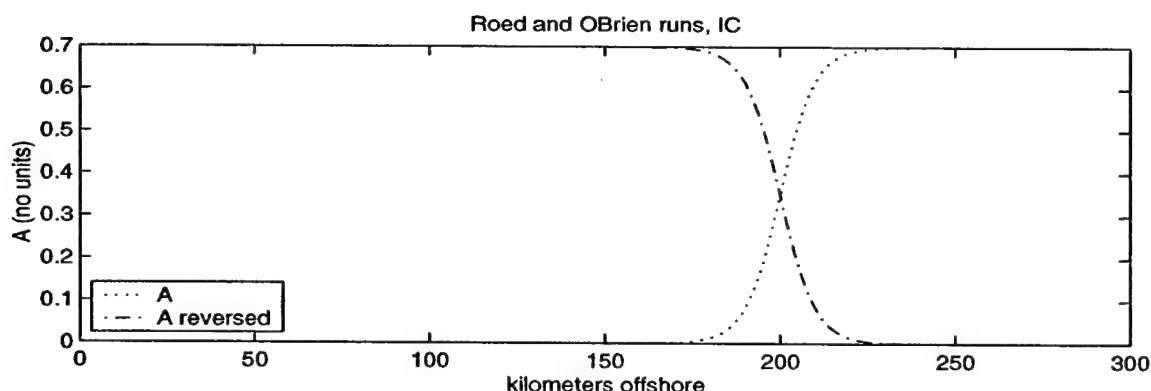
Figure 3-3: The initial condition of the Roed and O'Brien (1983) runs.

The diffusivities, A_H and K_H, are chosen to be as small as possible and still give numerical stability. They have values of 100 m^2 s^{-1} and 300 m^2 s^{-1} respectively. The large values of the diffusion coefficients are required to damp inertial oscillations. The wind stress used by Roed and O'Brien (1983) and this study is 0.1 N/m^2, corresponding to a wind speed of about 8.4 m/s and it is directed as shown in figure 3-1. To reduce the impact of inertial oscillations, the wind is linearly ramped up over three days. As in their study, the background geostrophic velocity is uniformly zero. The model is run for fifteen days.

3.3.3 Results and discussion

The results of the experiment with ice on the offshore half of the model domain are shown in figure 3-4. The ice edge is advected shoreward over the course of the experiment, consistent with Ekman transport of ice. The ice velocity is both shoreward and downstream. The water velocity is almost entirely shoreward, as is expected from an Ekman balance but there is a small upstream velocity. Under ice, the water velocity is larger than it is in ice free regions. The adjustment period, as the wind is ramped up, is visible in the position of the ice edge during the first few days of the run. The ice edge, shown in figure 3-4b, is similar to figure 6 in Roed and O'Brien (1983). (figure 3-5)
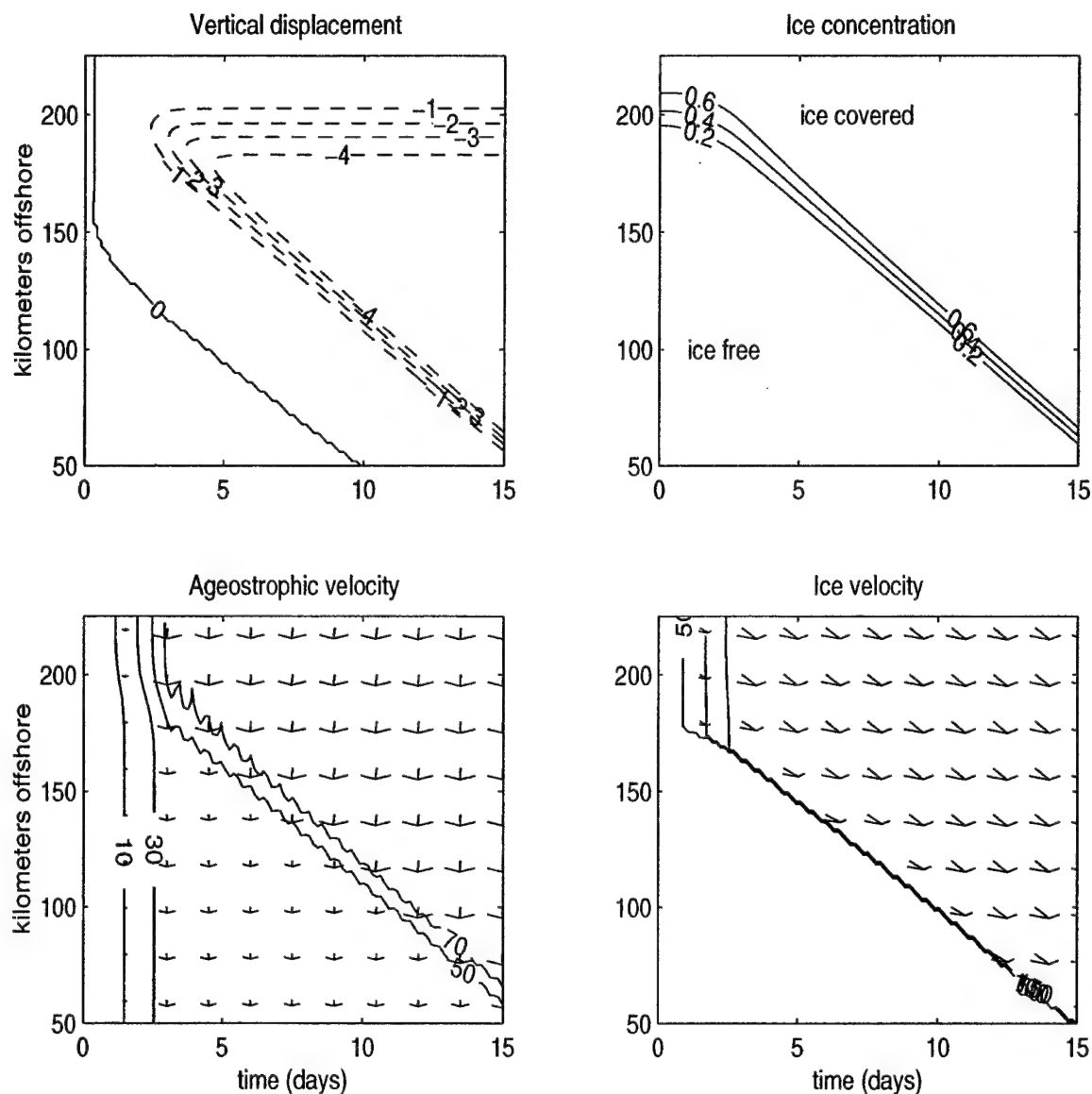
Figure 3-4: An ice edge over water with no geostrophic transport. A wind of 6 m/s is imposed on the system. The wind is ramped up over three days and then held constant. (a: upper left) The displacement of an originally flat surface at the base of the Ekman layer due to divergence of the ageostrophic ocean velocity. Dashed contours indicated negative values. (b: upper right) The position of the ice edge. (c: lower left) The ageostrophic ocean velocity (arrows) with absolute speed contoured. Arrows pointing right indicate movement in the $+x$ direction. Arrows pointing up indicated movement in the $+y$ direction. The wind stress vector (not shown) would point to the right. The arrows are exaggerated by approximately a factor of ten in the cross stream direction. Contours are labeled in mm/second. (d: lower right) The ice velocity (arrows) with absolute speed contoured. Arrows and contours as in the plot of ageostrophic velocity. The initial ice maximum is between 200 km and 300 km offshore.

137
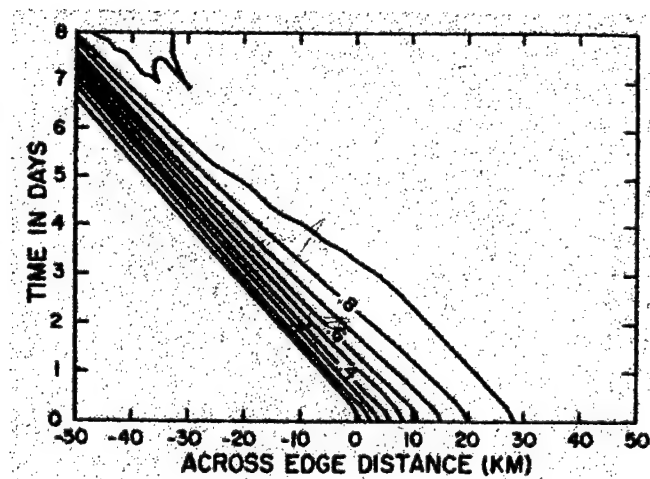
Figure 3-5: Ice concentration versus time for an experiment similar to the one presented here. Compare to figure 3-4b. Note the axes are reversed. From Roed and O'Brien (1983).

The momentum and density balances after ten days are shown in figure 3-6. In the along stream direction for the ice, the primary balance is between the air-ice stress and the ice-water stress, as predicted from the scaling, with the Coriolis term balancing their remainder. The balance between the stresses drives a substantial downstream advection of ice while the Ekman balance of the remainder generates a significantly smaller shoreward Ekman transport. (The cross stream ice speed has been exaggerated by about a factor of 10 in figure 3-4 so that it is visible at all.) In the cross stream direction there is no air-ice stress and the balance is between the ice-water stress and the Coriolis term.

The balance in the ocean momentum equations is between the Coriolis terms and the stresses. In the ice free region, it is between the air-water stress and the Coriolis force; in the ice covered region it is between the ice-water stress and the Coriolis force. Because the ice concentration is high (about 0.9), the air-water stress is insignificant in the ice covered region. Combined, this drives a shoreward transport of water across the entire domain but because the stress on the ice covered region is larger than the stress on the ice free region, there is a convergence in Ekman transport at the ice edge. The convergence drives downwelling at the ice edge (figure 3-4a). Figure 3-4a is

138
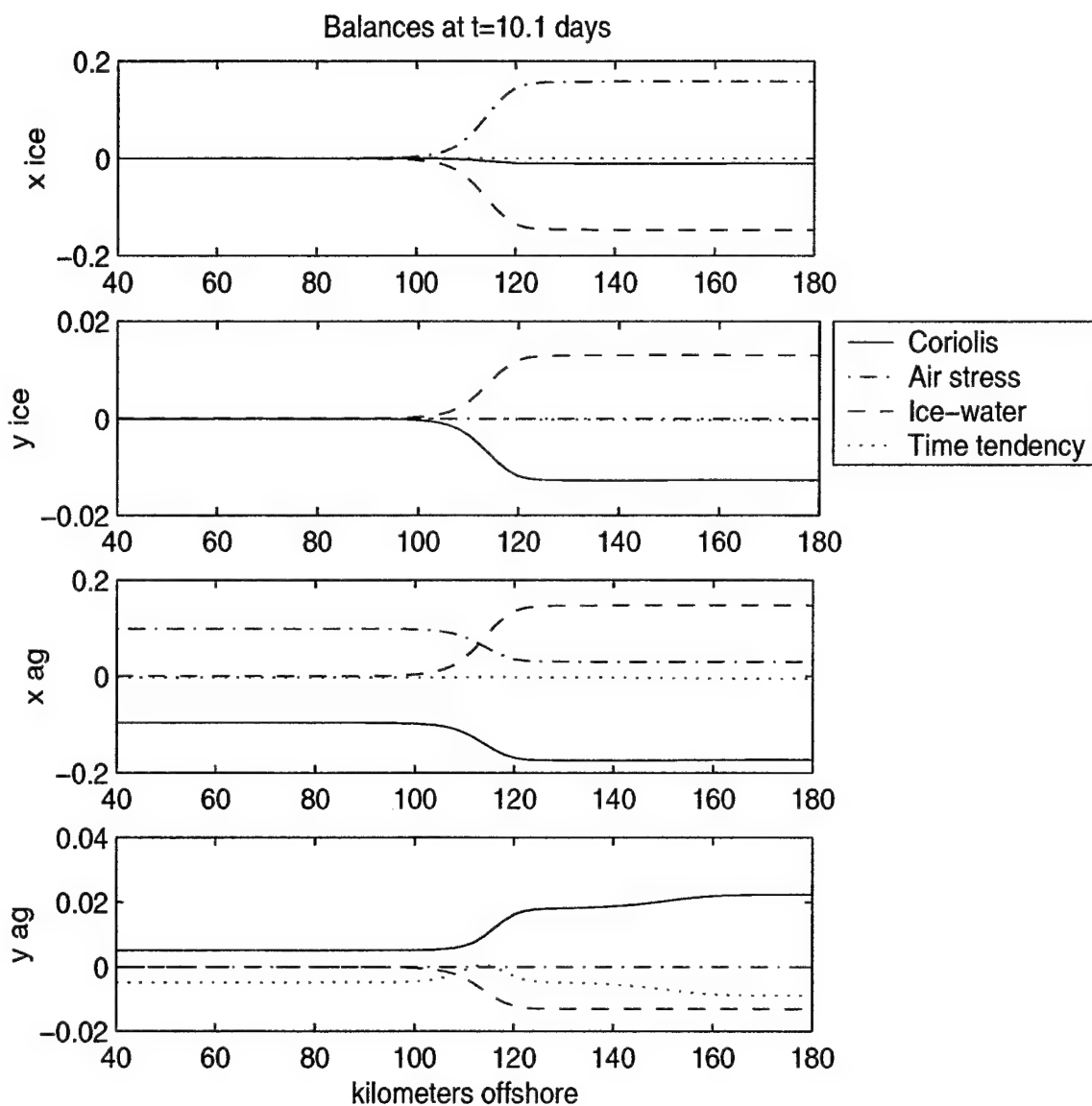
Figure 3-6: The balances for the Roed and O'Brien (1983) experiment, after ten days. Line types are defined on page 130. Units on the vertical axis are kg m s^{-2}.
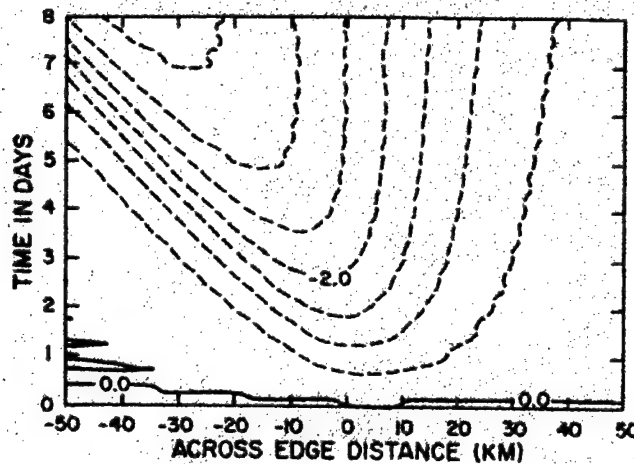
Figure 3-7: Vertical displacement versus time for an experiment similar to the one presented here. Compare to figure 3-4a. Note the axes are reversed. From Roed and O'Brien (1983)

similar to figure 7 in Roed and O'Brien (1983). (figure 3-7) The horizontal lines in (a) near y=150 km, are small inertial oscillations. The cross stream momentum balances for both the ice and the water is the Ekman balance: the ice-water stress balances the Coriolis force. This drives a downstream transport of ice and an upstream transport of water (figures 3-4 c and d).

The ice edge is advected in the $-y$ direction by the ice Ekman velocity. Because the stress is weighted by the ice concentration, more ice leads to larger stresses. The ice edge gradient increases over the course of the experiment because the Ekman transport is convergent.

In this study, the ice coverage is generally placed between the coast and some point off shore, reversed from the study presented by Roed and O'Brien (1983). The dash-dot line in figure 3-3 shows this initial condition. The experiment is repeated with the reversed initial ice concentration and the results are shown in figures 3-8 and 3-9.

The balances are the same as in the previous experiment. In the downstream direction the air-ice stress accelerates the ice until the ice-water stress balances it. The water-ice and air-water stress are in the same direction in the ocean and they are

140
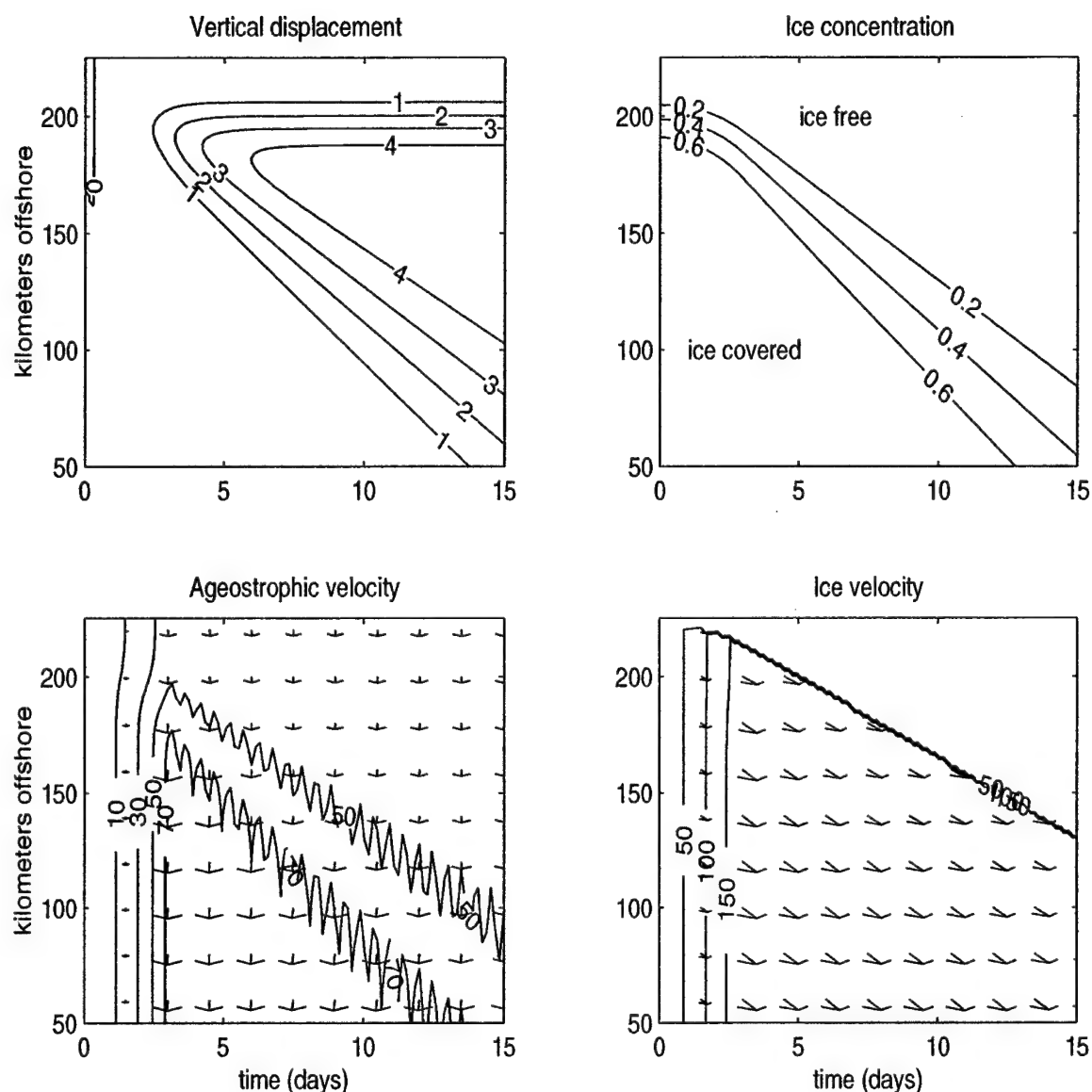
Figure 3-8: An ice edge over water with no geostrophic current. A wind of 6 m/s is imposed. The wind is ramped up over three days and then held constant. (upper left: a) The displacement of an originally flat surface at the base of the Ekman layer due to divergence of the ageostrophic ocean velocity. Dashed contours indicated negative values. (upper right: b) The position of the ice edge. (lower left: c) The ageostrophic ocean velocity (arrows) with absolute speed contoured. Arrows pointing right indicate movement in the $+x$ direction. Arrows pointing up indicated movement in the $+y$ direction. The wind stress vector (not shown) would point to the right. The arrows are exaggerated by approximately a factor of ten in the cross-stream direction. Contours are labeled in mm/second. (lower right: d) The ice velocity (arrows) with absolute speed contoured. Arrows and contours as in the plot of ageostrophic velocity. The initial ice maximum is between 0 km and 200 km offshore.

141
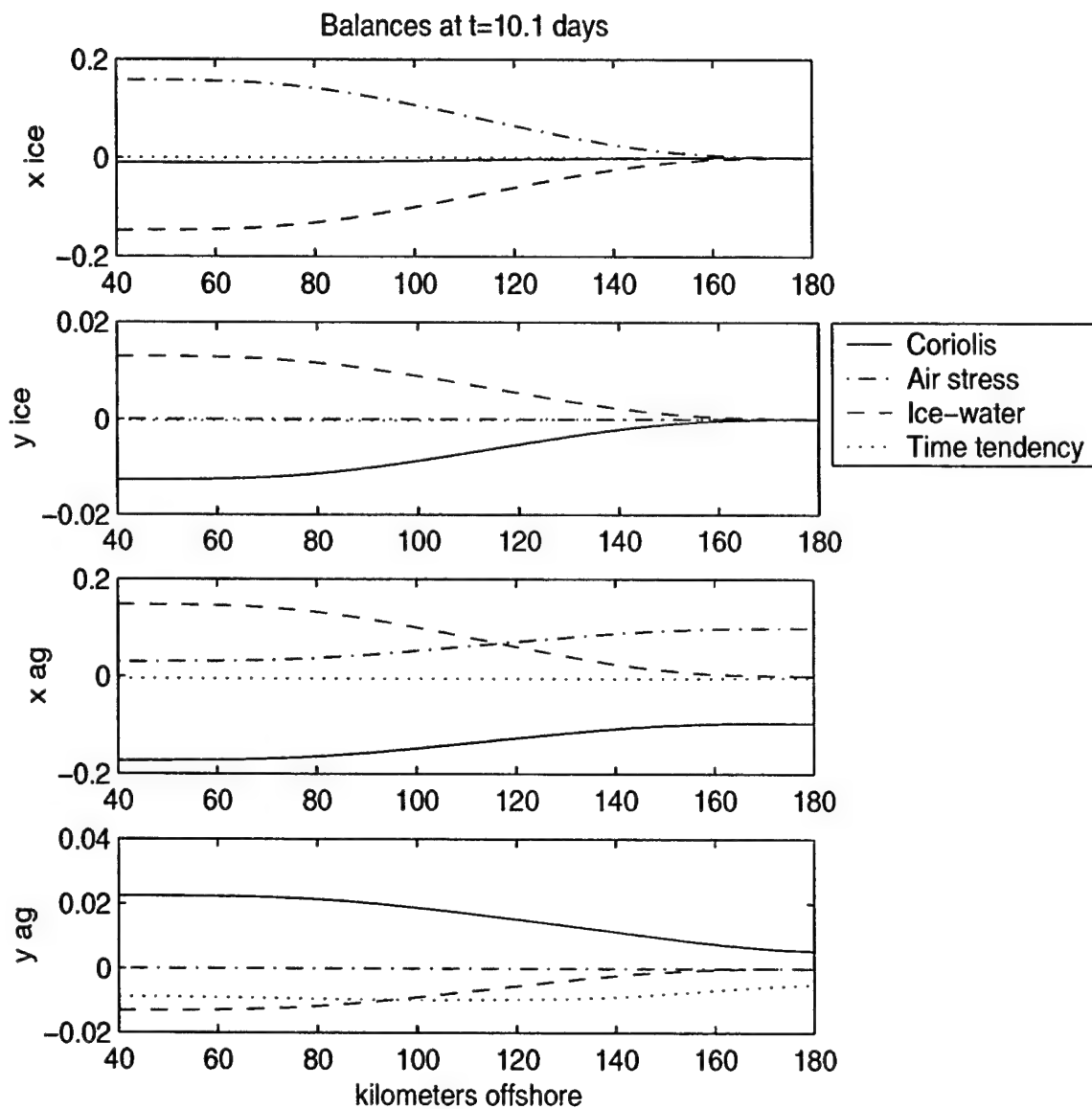
Figure 3-9: The balances for the reversed Roed and O'Brien (1983) experiment, after ten days. Line types are defined on page 130. Units on the vertical axis are kg m s^{-2}.

balanced by the Coriolis force, driving a strong shoreward Ekman transport. However, the total stress under ice is larger than the air-water stress on ice free regions and this creates a divergence in the ageostrophic velocity at the ice edge. Upwelling is diagnosed in the ocean to balance the mass.

In the cross stream direction, the strong shoreward ocean Ekman transport creates a cross stream ice-water stress which is balanced by the Coriolis force. The stress on the ice is proportional to the ice concentration and regions of higher ice concentration have larger velocity than regions of lower ice concentration. This causes the isopleths of high ice concentration to move towards shore faster than the isopleths of low ice concentration and the initially narrow ice edge spreads out. The ice diverges across the ice edge.

The x momentum balances and conservation of mass are used to estimate the vertical velocities and displacements. In the downstream direction, the dominant terms in the ice momentum balance are

$$\tau_{wi}^x + \tau_{ai}^x \approx 0 \tag{3.39}$$

In the ice free region, the dominant terms in the downstream ageostrophic ocean momentum balance are

$$f_0 v_{ag} + \frac{(1-A)\tau_{aw}^x}{\rho_o \delta} \approx 0 \tag{3.40}$$

and in the ice covered region, the dominant terms in the downstream ageostrophic ocean momentum balance are

$$f_0 v_{ag} - \frac{A\tau_{wi}^x}{\rho_o \delta} \approx 0 \tag{3.41}$$

Using equation 3.39, τ_{wi}^x is eliminated from 3.41.

$$f_0 v_{ag} + \frac{A\tau_{ai}^x}{\rho_o \delta} \approx 0 \tag{3.42}$$

143

This shows that the onshore ocean transport is basically driven by the wind stress on the ice. This is an approximation to the full Ekman balance. The full Ekman balance includes the ageostrophic transport of both water and ice but because the mass of ice is so small compared to the mass of water, it is neglected in this approximation. Equations 3.40 and 3.42 are solved for v_{ag} to estimate the divergence in transport across the ice edge. In the ice free region, $A = 0$ and

$$v_{ag} = -\frac{\tau_{aw}^x}{f_0 \rho_o \delta} \tag{3.43}$$

and in the ice covered area

$$v_{ag} = -\frac{A\tau_{ai}^x}{f_0 \rho_o \delta} \tag{3.44}$$

where A is the concentration in the ice covered area. For these estimates, the ice concentration, A is set to 0.7. The vertical velocity is estimated from 3.35.

$$
\begin{aligned}
w &= \delta \frac{\Delta v}{\Delta y} \\
&= -\frac{\tau_{aw}^x - A\tau_{ai}^x}{\rho_o f_0 \Delta y}
\end{aligned}
\tag{3.45}
$$

Equations 3.5 and 3.6 relate the stress to wind speed. Substituting them into equation 3.45, w becomes

$$w = -\frac{C_{aw} - AC_{ai}}{\rho_o f_0 \Delta y} u_{air}^2 \tag{3.46}$$

Using 3.46, the vertical displacement is estimated from equation 3.36.

$$\eta \approx w\Delta t \tag{3.47}$$

A series of experiments with different wind speeds in the reversed Roed and O'Brien configuration were done to test equations 3.46 and 3.47. Figure 3-10 shows the mean upwelling velocities and displacements as a function of wind speed with solid lines and the predictions in dashed lines. In calculating the predicted values, all of the parameters are set by the model configuration except Δy and Δt. For

144
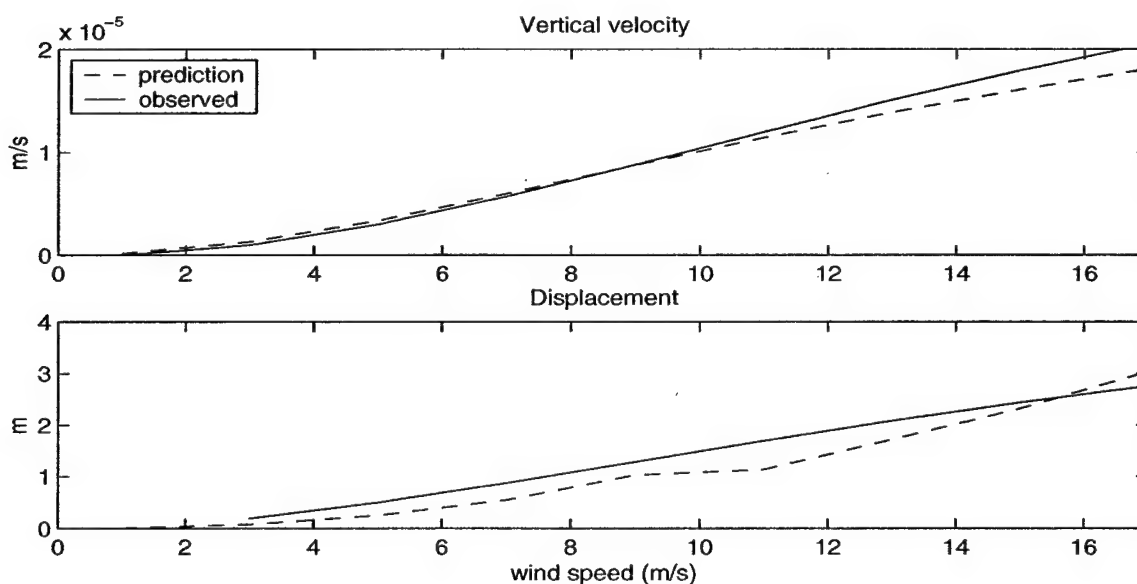
Figure 3-10: (a) Mean vertical velocity and (b) Mean displacement of the η surface as a function of wind speed.

figure 3-10, the value of Δy used in 3.46 is the mean distance from $A = 0$ to $A = .7$ and the value of Δt used in 3.47 is the mean time it takes the ice edge to pass a point in y. The uneven shapes of the predicted lines are a result of estimating Δy and Δt in this manner.

The magnitude of the upwelling and downwelling displacements produced by the model is of similar magnitude to observations. Johannessen et al. (1983) observe isopycnals doming upward near an ice edge after experiencing sustained winds of 8-10 m/s for two to three days, producing deformations of about 6 m. Observed vertical displacements are about twice as large as the implied vertical displacements in the model. The model underestimates both the deformation and the vertical velocity. Tuning the drag coefficients or other model parameters might bring the model into closer agreement with observations.

3.4 An ocean current under ice in the absence of wind

The interaction of ice and an underlying geostrophic current is now examined. In this section, the wind speed is assumed to be 0 m/s.

3.4.1 Predictions from scaling

When there is a current under the ice, the fundamental balance is between the Coriolis force and the tilt term. This balance drives the ice at the same speed as the water. After that, there may be small perturbations around this basic state but no other steady balance exists because there are no other forces acting on the ice-ocean system. In this section, the perturbation is described. In the discussion section, the source of the perturbation is discussed.

If there is no wind stress, the air-water and air-ice stresses are removed from equations 3.19 and 3.20. The non-dimensionalized equations without wind are

$$\frac{U}{T}\frac{D\vec{u_i'}}{Dt'} = -f_0 u^* \hat{k} \times \vec{u_{ai}} + C_{wi}\frac{(u^*)^2}{D}|\vec{u_{ag}} - \vec{u_{ai}'}|(\vec{u_{ag}} - \vec{u_{ai}'}) \qquad (3.48)$$

$$\frac{U}{T}\frac{D\vec{u_w'}}{Dt'} = -f_0 u^* \hat{k} \times \vec{u_{ag}} - AC_{wi}\frac{\rho_i}{\rho_o}\frac{(u^*)^2}{\delta}|\vec{u_{ag}} - \vec{u_{ai}'}|(\vec{u_{ag}} - \vec{u_{ai}'}) \qquad (3.49)$$

where the primes indicate dimensionless variables and the substantial derivative for the water equation is expanded as (equation 3.32):

$$\frac{U}{T}\frac{D\vec{u_w'}}{Dt'} = \frac{U}{T}[\left[\frac{\partial}{\partial t'}\left(u_g' + \frac{u^*}{U}u_{ag}'\right) + \frac{u^*}{L/T}v_{ag}\frac{\partial}{\partial y}\left(u_g + \frac{u^*}{U}u_{ag}\right)\right]\hat{i}$$
$$+ \left[\frac{u^*}{U}\frac{\partial v_{ag}}{\partial t} + \frac{u^*}{U}\frac{u^*}{L/T}v_{ag}\frac{\partial v_{ag}}{\partial y}\right]\hat{j}]$$

In this case, u^* is simply a scale for the ageostrophic velocity and it is not tied to the wind as it was originally defined. The substantial derivative for the ice equa-

146

tion is identical but the water ageostrophic terms (u_{ag}, v_{ag}) are replaced by the ice ageostrophic terms (u_{ai}, v_{ai}).

The time scale is chosen to be the inertial time scale, $\frac{1}{f_0}$. Both sides of equations 3.48 and 3.49 are divided by $U f_0$. The non-dimensionalized equations become

$$\frac{D\vec{u_i}}{Dt'} = -\frac{u^*}{U}\hat{k} \times \vec{u_{ai}} + C_{wi}\frac{u^*}{Df_0}\frac{u^*}{U}|\vec{u_{ag}} - \vec{u_{ai}}|(\vec{u_{ag}} - \vec{u_{ai}}) \tag{3.50}$$

$$\frac{D\vec{u_w}}{Dt'} = -\frac{u^*}{U}\hat{k} \times \vec{u_{ag}} - AC_{wi}\frac{\rho_i}{\rho_o}\frac{u^*}{\delta f_0}\frac{u^*}{U}|\vec{u_{ag}} - \vec{u_{ai}}|(\vec{u_{ag}} - \vec{u_{ai}}) \tag{3.51}$$

The standard values in this chapter of f_0=1.4·10^{-4} s^{-1}, δ=17 m, D=1 m, and C_{wi}=10^{-2} are used to evaluate the coefficients of equations 3.50 and 3.51. The ice concentration is chosen to be 1 and the length scale is chosen to be 10 kilometers, or the width of the density front initially. U, the scale for the geostrophic velocity, is 5 cm/s, or the initial value derived from the density front by thermal wind[6]. The ageostrophic velocity, u^*, is arbitrarily chosen to be small in comparison to the geostrophic velocity, or one tenth of the geostrophic velocity.[7] This ratio is confirmed later to be reasonable for the system. The dimensionless ratios have the following values

$$\begin{aligned} \frac{u^*}{U} &\approx 0.1 \\ \frac{u^*}{f_0 L} &\approx 0.004 \\ \frac{u^*}{f_0 \delta} &\approx 2 \\ \frac{u^*}{f_0 D} &\approx 35 \\ \frac{\rho_i}{\rho_o} &\approx 1 \end{aligned}$$

The order 1 terms of 3.48 and 3.49 are

$$\frac{\partial u_g}{\partial t} = 0 \tag{3.52}$$

---

[6]This value is smaller than the geostrophic velocity found in the previous section because in this calculation it is assumed that the ocean layer under the Ekman layer is motionless.

[7]Alternately, one can argue that if the ice-water stress is generating the ageostrophic velocity, then $\frac{u^*}{U} \sim \sqrt{C_{wi}} = 0.1$.

which is not surprising since there are no dynamics in this model that allow the geostrophic velocity to change. The terms with magnitude of order 0.1 (re-dimensionalized) are

$$\frac{\partial \vec{u_{ag}}}{\partial t} = -f_0 \hat{k} \times \vec{u_{ag}} \qquad \frac{\partial \vec{u_{ai}}}{\partial t} = -f_0 \hat{k} \times \vec{u_{ai}} \tag{3.53}$$

Equations 3.53 are the coupled equations for free inertial waves. The waves are not forced or damped. Once there is a perturbation to the system so that the ageostrophic velocity is not equal to zero, the waves are excited. If the model included ice rheology, the waves would be damped by the ice-ice interactions.

The inertial waves are excited when the ice's geostrophic velocity is not equal to the ocean's geostrophic velocity. Typically this occurs either at the initial condition if the ice is started from rest while the ocean has a geostrophic velocity or if diffusion or advection modifies the density field. When the ice and water geostrophic velocities are not equal, the difference in velocity can be broken up into an equivalent barotropic velocity and equivalent baroclinic velocity (figure 3.4.1). Over time, friction between the ice and water causes the equivalent baroclinic velocity to decay away and the equivalent barotropic velocity remains: the inertial waves in the ice and the ocean, locked together.

3.4.2 Model setup

The model is configured as a line, 300 kilometers long with a resolution of $\Delta y = 2$ km. Open boundaries are implemented at $y=0$ km and $y=300$ km. A front is placed near the middle of the domain, 150 km from the shoreward wall. The density diffusivity, K_H, is 300 m^2 s^{-1} and the momentum diffusivity, A_H, is 100 m^2 s^{-1}. The model is run for 15 days. Because there is no wind, the air-water and air-ice stresses are zero.

In this section it is assumed that the current has an initially uniform ice concentration, for simplicity. This configuration is consistent with the conditions of the East Greenland Current in winter, when the ice edge extends well beyond the current and
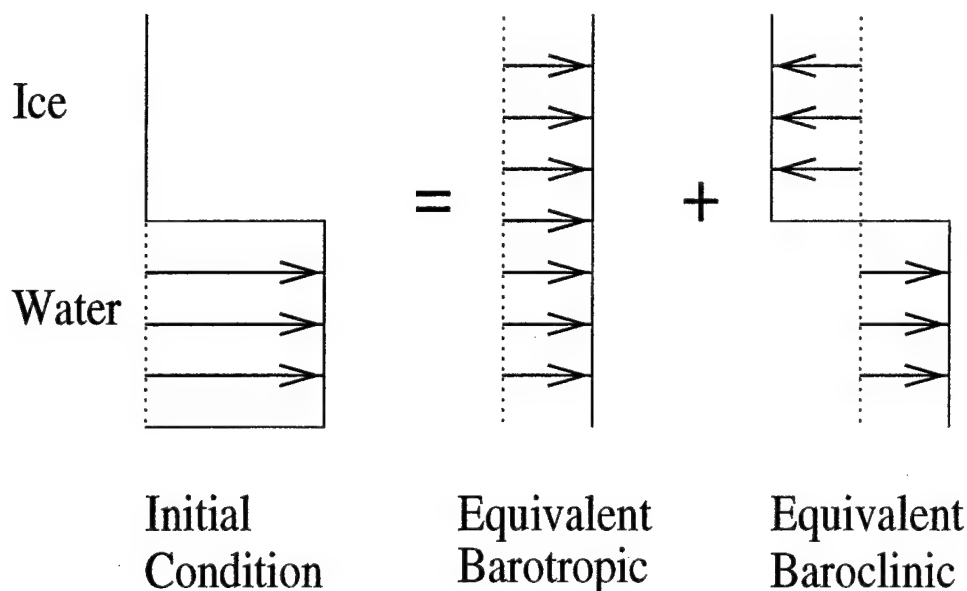
Figure 3-11: A sketch of the initial condition (with the ice stationary and the ocean moving) broken up into it equivalent barotropic and baroclinic components. Over time, the ice-water friction causes the baroclinic component to disappear and the barotropic inertial waves are left.

into the Norwegian basin itself. In the summer, the ice edge retracts to be coincident with the front, or shoreward of it. In the absence of wind, the placement of the ice edge does not have a large impact on the behavior of the ice-ocean system.

The initial distributions for ρ and A are shown in figure 3-12a and the initial velocity distribution for both experiments is shown in figure 3-12b. The geostrophic velocity is calculated from the density field using thermal wind, vertically averaged over the Ekman layer.

$$u_g = \frac{g\delta}{2\rho_o f_0} \frac{\partial \rho}{\partial y} \tag{3.54}$$

3.4.3   Results

The results are shown in figure 3-13. Without wind, there is no large cross stream motion of the front. The density field diffuses over the course of the experiment but otherwise does not not show large changes. Likewise, while the ice concentration shows some structure, the ice concentration varies less than 0.5% away from the initial

149
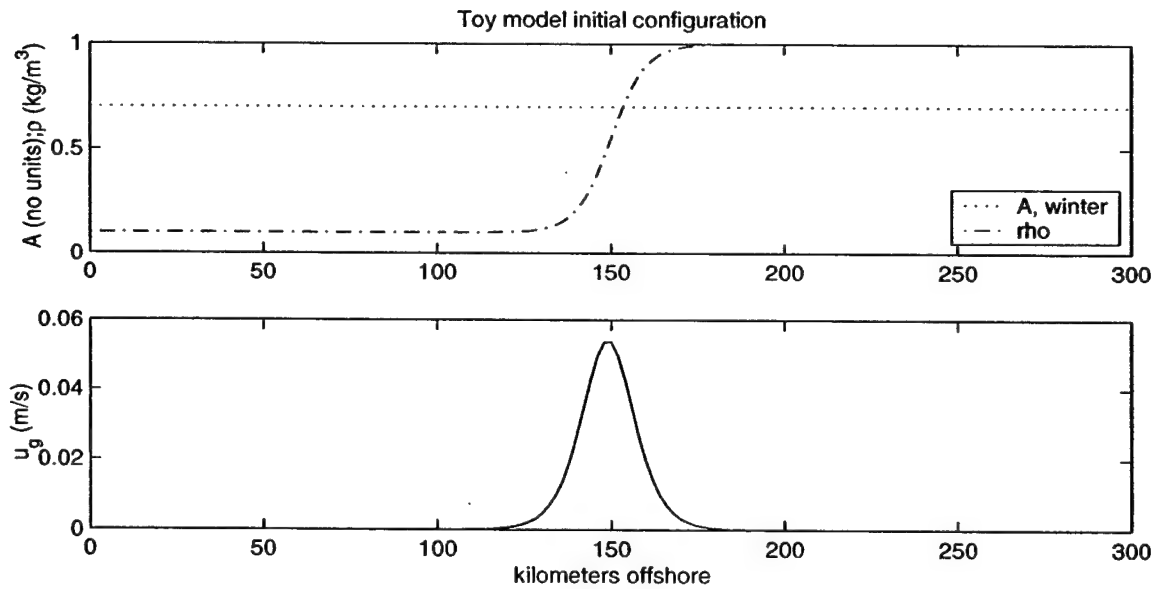
Figure 3-12: The initial conditions in the toy model when there is a current and ice, but no wind. In the top panel, the initial ice concentrations and density are shown. In the bottom panel, the initial geostrophic velocity is shown.

ice concentration. The ice has a substantial downstream velocity, roughly equal to the geostrophic velocity of the ocean, while the ageostrophic ocean velocity and cross stream ice velocity are very small and show little structure. These small velocities are due to inertial oscillations. This suggests that in the absence of wind, to first order, the ice is carried along with the geostrophic current.

The momentum balances after ten days are shown in figure 3-14. As predicted from the scaling, in the cross stream direction of the ice equation, the dominant balance is between the sea surface tilt and the Coriolis force. All other momentum equations have a balance between the Coriolis term and the time tendency, indicating there is nothing more significant than inertial oscillations occurring. The cross stream structure of ice velocity is created by the inertial oscillations. The cross stream ice velocity is very small, as is the divergence. The divergence in v_i causes the changes in ice concentration over the jet but because the divergence is small, the variation in ice concentrations are minimal.

The density balance (not shown) is between the diffusion of density and the time

150
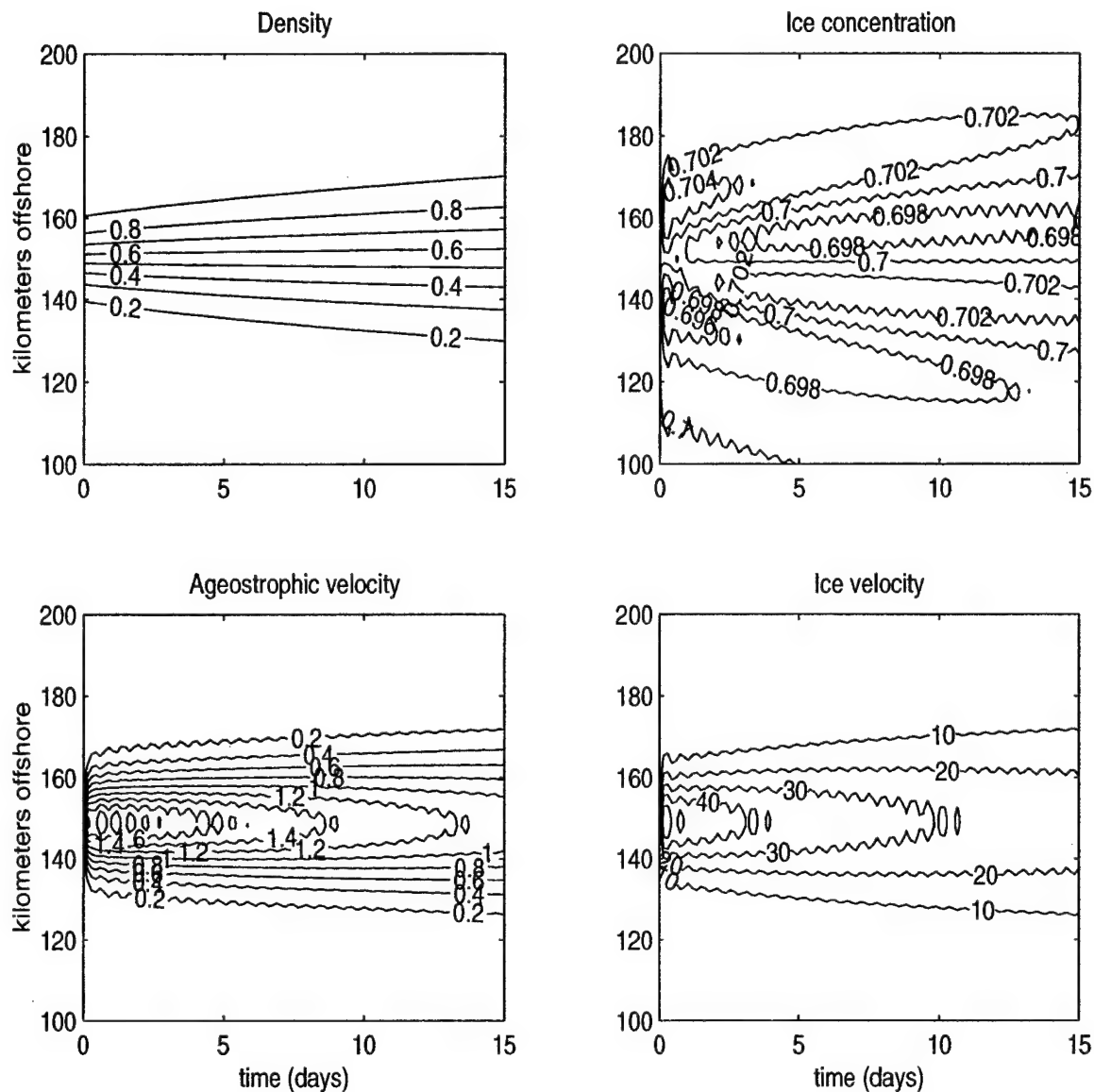
Figure 3-13: The results from the jet only, no wind experiment. (upper left: a) the density anomaly, versus time. (upper right: b) the ice concentration, versus time. (lower left: c) the water speed, versus time. Contours are labeled in mm/second. (lower right: d) the downstream ice speed. Contours as in the ageostrophic velocity. The small wiggles in the contours are due to inertial oscillations. Velocity vectors are not shown because the ageostrophic velocity fields are dominated by inertial oscillations. If the geostrophic velocity was shown, it would be a vector pointing to the right.

151
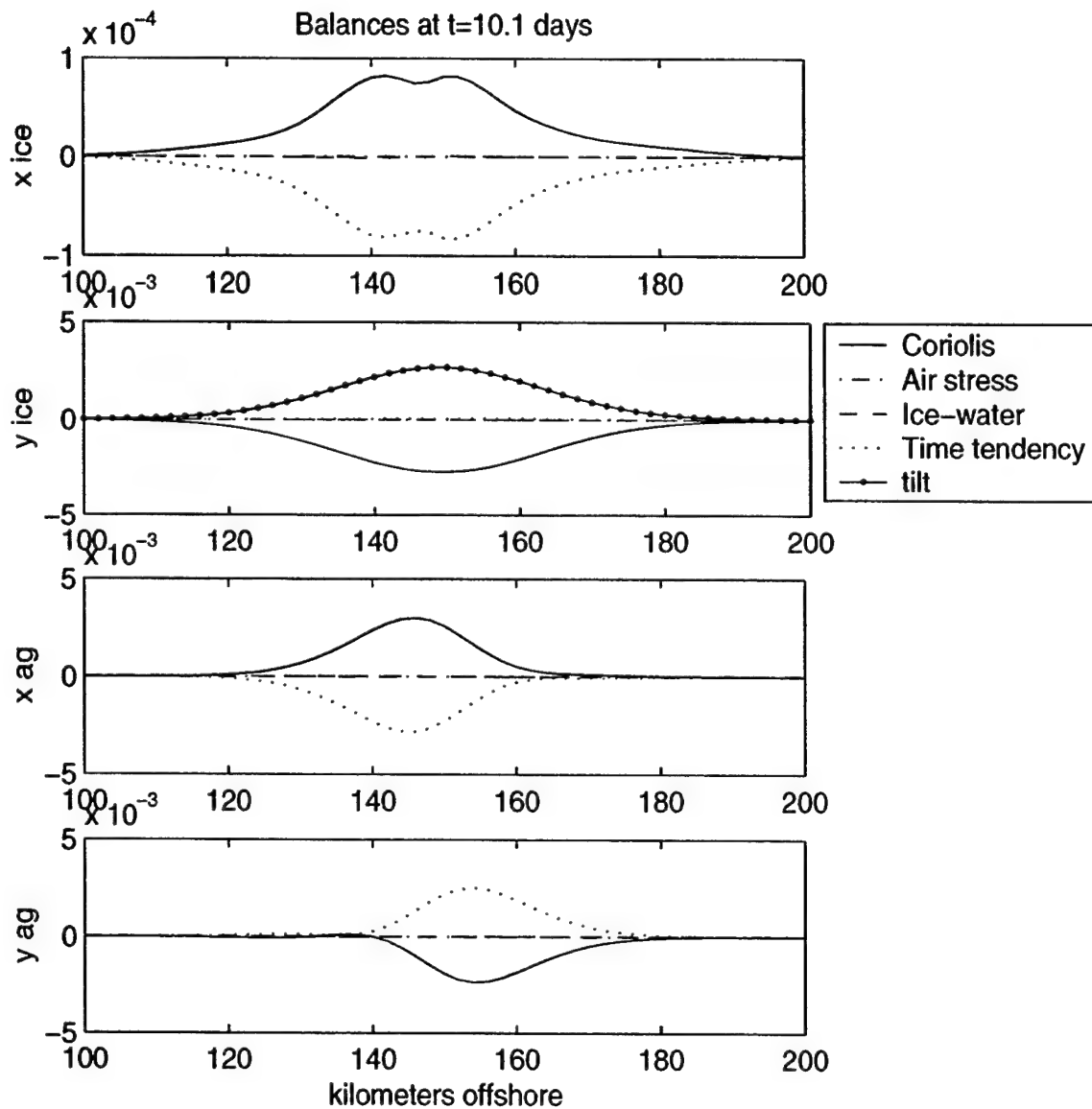
Figure 3-14: The momentum balance after ten days when there is a jet under ice. Line types are explained in equations 3.33 on page 130. The balances add up to the time tendency. The units of the vertical axis are kg m s^{-2}.

tendency. This balance causes the front to spread out, as seen in figure 3-13a. Because the front spreads out as time passes and the geostrophic transport is constant, the geostrophic velocity decreases as the front grows wider. The decrease in downstream ice speed over time (figure 3-13d) is due to the decrease in geostrophic velocity.

The mechanism that excites the waves is now presented. The momentum balances over the first twenty-four hours of the experiment are shown in figure 3-15. As the experiment begins, the ice is initially at rest while the water has the geostrophic jet. Over the jet, in the downstream direction

$$u_w - u_i \approx u_g$$

Because ice-water stress is proportional to the difference between the ice velocity and the ocean velocity, squared, there is initially a strong ice-water stress. This is balanced by the time tendency. Therefore, in the downstream direction, the initial momentum balances are

$$\frac{\partial u_i}{\partial t} = \frac{\rho_i C_{wi}}{D} u_g^2 \tag{3.55}$$

$$\frac{\partial u_{ag}}{\partial t} = -\frac{A \rho_i C_{wi}}{\rho_o \delta} u_g^2 \tag{3.56}$$

The ice is initially accelerated to the geostrophic velocity by the ice-water drag. Because the ice-water drag also affects the ocean (in the opposite direction), it decelerates the ageostrophic velocity in the ocean. The system reaches a steady state when the total ice velocity is equal to the total ocean velocity. In the cross stream direction, the initial balance is between the time tendency and the tilt term.

$$\frac{\partial v_i}{\partial t} = f_0 u_g \tag{3.57}$$

Because there is an initial geostrophic velocity, the surface of the ocean is tilted. The ice "slides down" the slope, driving an ageostrophic ice velocity in the cross-stream
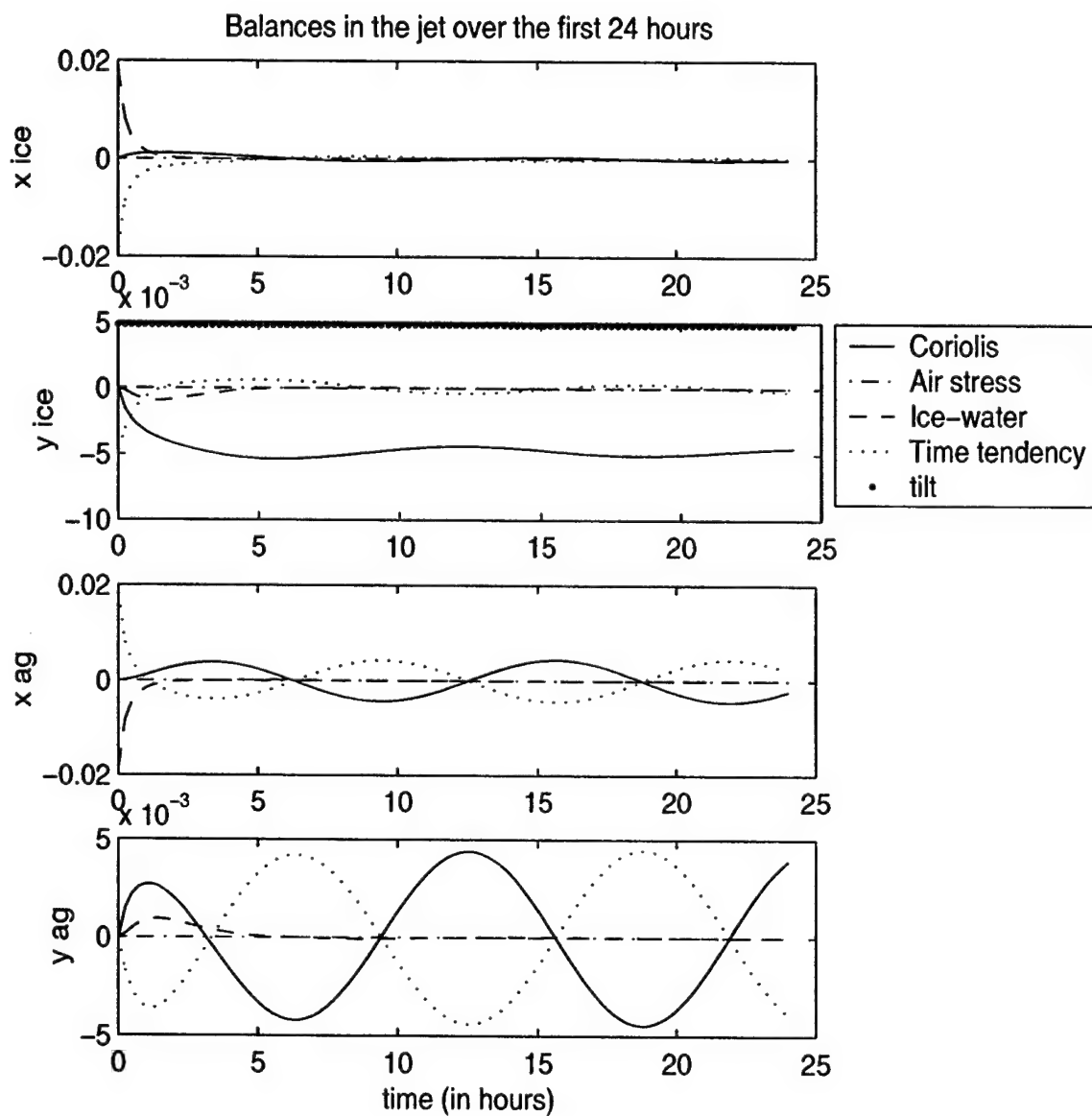
Figure 3-15: The momentum balance during the first 24 hours of the experiment with the jet under the ice and no wind. Line types are explained in equations 3.33 on page 130. The balances add up to the time tendency. The units of the vertical axis are kg m s^{-2}.

direction. In the ocean, the cross stream balance is initially all 0 because u_g does not enter the equation directly and none of the other velocities are non-zero.

The ageostrophic motion in both directions is accelerated by the initially large difference in velocities. The ice-water stress is significant until the ice and water have approximately the same velocity in both the geostrophic and ageostrophic components. As time elapses, the Coriolis force ramps up and a balance between the Coriolis force and the time tendency develops. This is, of course, inertial waves. While the ice-water stress diminishes greatly as the experiment progresses, it does not disappear because the ice and water speeds are not identically equal. This suggests that in the third (or higher) order, there is a balance between the remainder of the ice-water stress and possibly the Coriolis force, resulting in a very small cross stream Ekman transport with the ice and water being transported in opposite directions. In figure 3-16, the balance between the ice-water stress and the residual Coriolis force is shown.

The inertial waves observed are not the result of a numerical instability in the model. Instead, they are generated by a mismatch between the ice speed and the geostrophic current speed. If the model is initiated with the ice speed equal to the geostrophic velocity in the ocean and the diffusion of density and momentum is set to $0 \text{ m}^2\text{s}^{-1}$, the inertial waves disappear from the model. When the ice velocity exactly matches the ocean velocity there is no ice-water stress and the system continues in this state indefinitely. If the initial ice velocity does not equal the geostrophic velocity, inertial waves will be generated, as discussed above. If any diffusion is allowed in the model, the geostrophic velocity changes over time and inertial waves are generated as the ice responds to the changes in the geostrophic velocity.

The ice-water stress only plays a significant role in the first few hours, as the ice velocity accelerates to match the geostrophic velocity. After that point, the ice and water velocities are nearly equal and the ice-water stress is negligible. This has important repercussions on ice transport. When an underlying geostrophic current

155
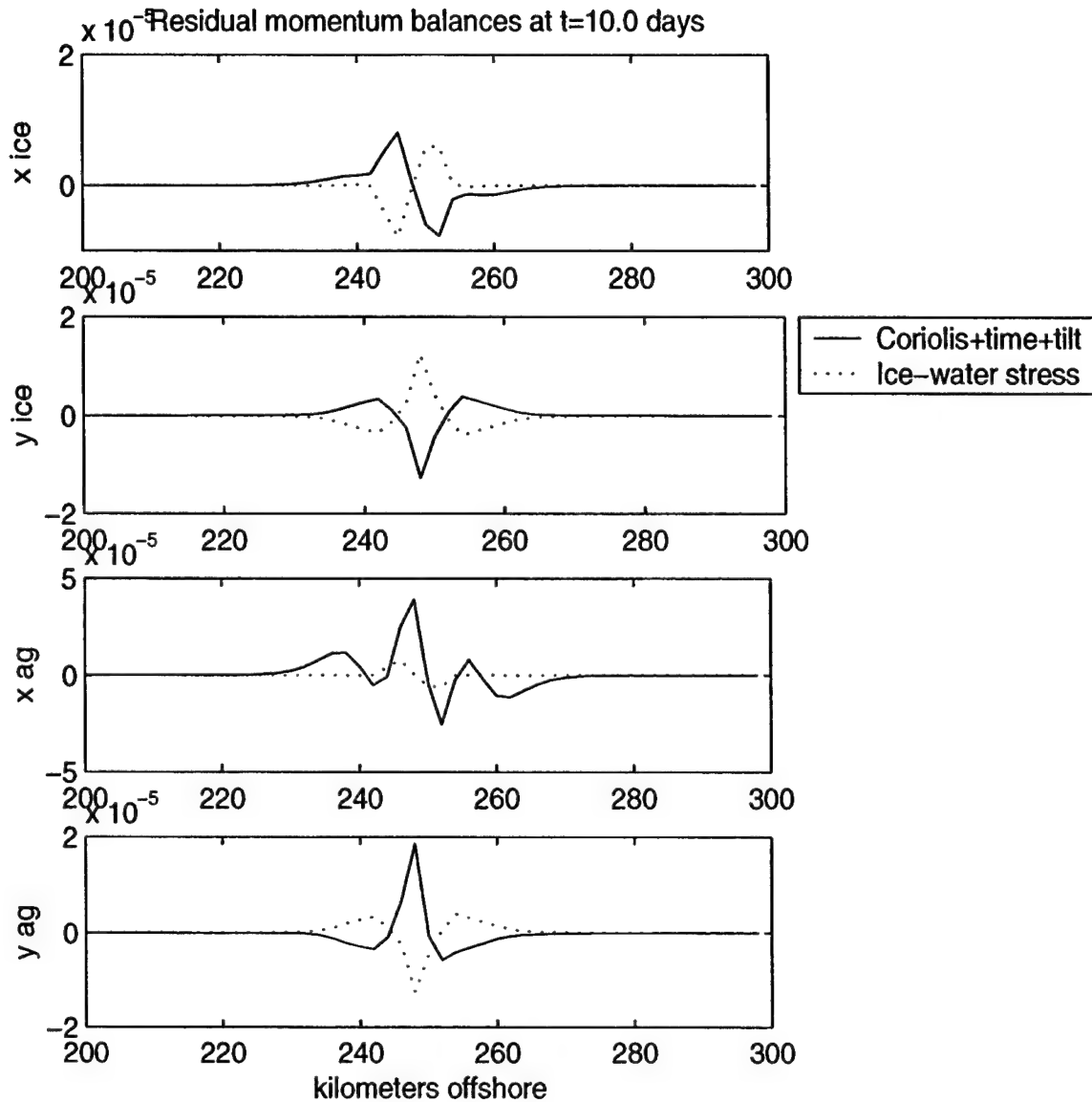
Figure 3-16: The residual momentum balance after ten days. The ice water stress is compared to the sum of the Coriolis force, the time tendency and the tilt and the small remainder is nearly balanced. The units of the vertical axis are kg m s^{-2}. The Ekman transport, $T = \frac{\tau}{\rho_o f_0}$, associated with a stress of 10^{-5} kg m^{-1} s^{-2} is about $7 \cdot 10^{-5}$ m^2 s^{-1}. The transport, T, is divided by the Ekman layer thickness, δ, and the average water speeds is estimated as $4 \cdot 10^{-6}$ m s^{-1}. The average ice speed is estimated by dividing the transport by the ice thickness and an ice speed of about $7 \cdot 10^{-5}$ m s^{-1} is found. These speeds are very small and little different than 0 m s^{-1}.

causes the sea surface to be tilted, the cross stream advection of ice is very small and the ice concentration over the jet is not significantly different than it is over motionless water. The ice is carried along with the ocean jet at comparable speeds to the underlying water.

The magnitude of the cross stream ageostrophic velocity is small and dominated by inertial oscillations, with frequent reversals in direction. As a result, the cross stream divergence in water transport is small, driving a small vertical velocity (equation 3.35). When the vertical velocity is integrated forward in time to determine the displacement of an originally flat surface, the reversals in direction tend to integrate to zero, resulting in very small vertical displacements (equation 3.36).

3.5   Ice, wind and ocean currents

In section 3.3, the interaction of wind and ice in the absence of underlying currents is examined. The ice-ocean system has a net transport to the right of the wind but individually the layers are a two layer Ekman spiral. The ice, which contains about 5% of the mass of the system, has velocity which is mostly downwind and slightly shoreward, while the water has a velocity that is mostly shoreward and slightly up wind. If there is an ice edge, divergence in the ocean Ekman transport at the ice edge drives vertical motion in the ocean. The interesting dynamics occurs at the ice edge or in regions of gradients in ice concentration in the absence of an underlying geostrophic current.

In section 3.4, the interaction of ice and an underlying current in the absence of wind is examined. In this limit, the ice is carried along with the geostrophic current and aside from ubiquitous inertial oscillations generated when the ice is accelerated (either initially or as the result of changing geostrophic velocity), there is little motion.

In this section, ice, wind and ocean currents are brought together and the competing influences of the Ekman balance with the tilt term are examined. Through

Ekman dynamics, the wind drives a cross wind transport while the tilt term drives downstream transport; the two effects are orthogonal. Unless the wind is allowed to affect the geostrophic background current, the two responses are independent.

Several different configurations are modeled. Jet-like density driven ocean currents are first examined, both with a homogeneous ice covering and partial ice covering. Afterwards, a brief examination of barotropic background currents driven by the wind is conducted.

3.5.1 Scaling comments

When the underlying current is combined with the wind, two different balances in the ice momentum equations come into competition. In the no wind limit, the balance is between the tilt term and the Coriolis term. In the no current limit, the balance is between the air-ice stress and the Coriolis term. In many ways, these two transports are orthogonal and do not really interact unless there is a way for the wind to directly affect the geostrophic velocity[8]. The relative magnitude of the geostrophic transport to the Ekman transport determines which balance dominates the dynamics of a system.

If the steady state of the system is considered, the general scaling discussed in section 3.2.1 is appropriate for this problem. The ratio of the wind driven Ekman transport to the geostrophic transport in the ocean is represented by

$$\frac{A\tau_{ai}}{\rho_o \delta f_0 U} \tag{3.58}$$

When this fraction is greater than one, the Ekman balance dominates the momentum equations and the majority of the water transport is perpendicular to the wind and

---

[8]If the equations are not depth averaged, the horizontal divergence of the ageostrophic transports alter the vertical structure of the cross-stream density gradients. By depth averaging, this interaction is eliminated. That is, if a multi-layered ocean model were used, the ocean density field would be free to adjust to vertical velocities.

current[9]. When this fraction is less than one, the tilt term balances the Coriolis force, the Ekman transport is negligible, and the majority of the ice and water transport is downstream. If u_g is 0.05 m/s and the rest of the variables have the standard values discussed in section 3.2.1, this ratio is less than 1 for all wind speeds less than about 6 m/s. However, it is argued in chapter 2 that there is a relationship between the wind stress and the barotropic current

$$ U \approx \frac{\tau_{aw}^x}{\rho_o f_0} \frac{2}{\delta} \frac{1}{\alpha_r - \alpha_i} $$

where the constants α_r and α_i are defined in chapter 2. If that relationship is used to determine U, the barotropic current increases with the wind speed and the ratio 3.58 is asymptotic and approaches $\frac{C_{ai}}{C_{aw}} \frac{\alpha_r - \alpha_i}{2}$ which is about 0.8 for the parameters used in this study. This suggests that the Ekman transport and the geostrophic transports are approximately equally significant. The ice transport will be mostly downstream because both mechanisms drive down stream transport of ice while the ageostrophic water transport will be shoreward due to Ekman dynamics.

3.5.2 Model setup

The model is configured as a line, 300 kilometers long with a resolution of $\Delta y = 2$ km. Open boundaries are implemented at $y=0$ km and $y=300$ km. A front is placed near the offshore side of the domain, 250 km from the shoreward wall. The density diffusivity, K_H, is 300 m^2 s^{-1} and the momentum diffusivity, A_H, is 100 m^2 s^{-1}. In the standard cases discussed in this section, a wind of 6 m/s is imposed, making the ratio in equation 3.58 equal to about 1. The Ekman balance and the tilt-Coriolis balance are equally significant. At the start of the run, the wind speed is zero and

---

[9]Note that in the previous chapter when a wind stress of 0.1 N m^{-2} was used, that referred to the air-water stress on an entirely ice-free ocean. This ratio uses the air-ice stress, defined in equation 3.6, which is about three times larger than the air-water stress. The difference in stress is because the drag coefficient between ice and water is larger than the drag coefficient between air and water.

it is ramped up to its maximum value over three days. The background geostrophic velocity is calculated from thermal wind using the density field and the appropriate wind driven "barotropic" ocean velocity, calculated from 2.40. The two velocities are added to get the total geostrophic velocity.

$$u_g(y, t) = u_{tw}(y, t) + u_{bt}(t) \tag{3.59}$$

$$= \frac{g\delta}{2\rho_o f_0} \frac{\partial \rho(y, t)}{\partial y} + \frac{\tau_{aw}^x}{\rho_o f_0} \frac{2}{\delta} \frac{1}{\alpha_r - \alpha_i} \tag{3.60}$$

where the constants α_r and α_i are defined in chapter 2.

Two different initial ice concentrations are used. In the winter experiments, the initial ice concentration is constant at 0.7 across the domain. In the summer experiments, an ice edge is placed over the front, 250 km from the shoreward wall. The initial distributions for ρ and A are shown in figure 3-17a and the geostrophic velocity distribution for both sets of experiments is shown in figure 3-17b.

3.5.3 Results

In this section the results of the ice, wind and ocean current experiments are discussed. The results are broken up into three subsections. In the first two sections, the wind speed is held constant at 6 m/s. First, the case of 6 m/s winds over an initially uniform concentration ice field is discussed. Because this configuration is consistent with the East Greenland Current system in the winter (although with much lighter winds), this experiment is labeled the winter configuration. After that, there is a brief discussion of 6 m/s winds over an ice edge, similar to the configuration used in section 3.3, and this is labeled the summer configuration. Finally, a family of experiments is presented which vary the wind stress, the underlying geostrophic current, the surface ice concentration and the relative masses of ice and water. These results are presented in the variation of parameters section.

160
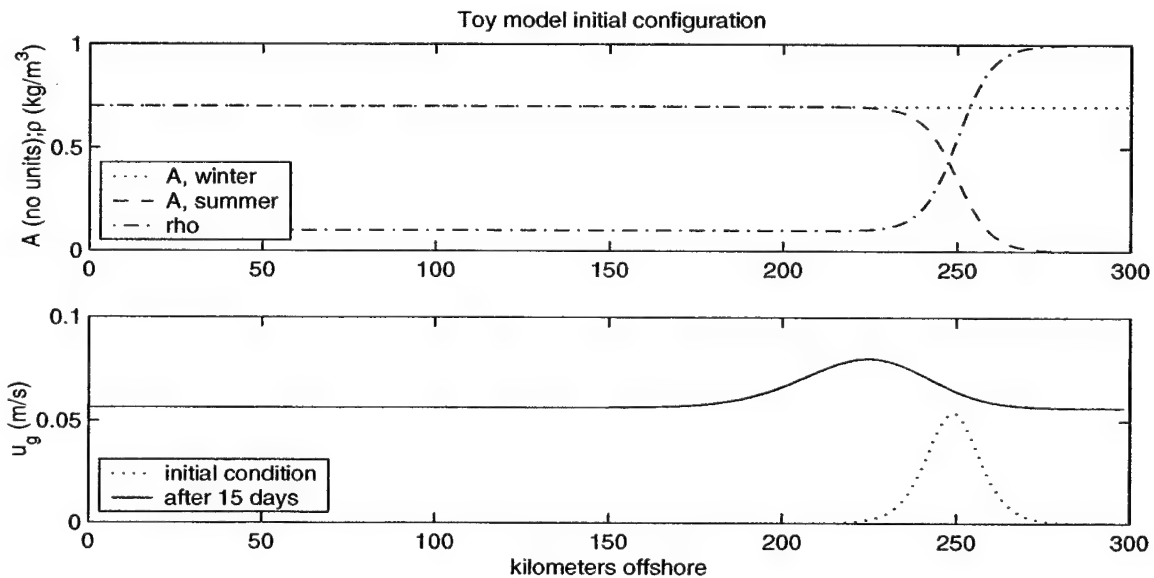
Figure 3-17: The initial conditions in the toy model, for both winter and summer experiments with wind. In the top panel, the initial ice concentrations and density are shown. In the bottom panel, the initial geostrophic velocity is shown, as is the geostrophic velocity after fifteen days of integration. After three days, the wind speed has ramped up to its maximum value and the geostrophic velocity consists of a jet, calculated from the current density field, and a background velocity, calculated from the wind speed.

Winter The results for the winter experiment, with complete ice coverage, with 6 m/s, wind are shown in figure 3-18 and the momentum balances are shown in figure 3-19. A directional plot of the momentum balances is shown in figure 3-20.

The results are similar to the experiments with the wind only and no current. In the downstream direction for the ice, the air-ice stress is balanced by the ice-water stress. The ice is accelerated by the wind until its speed is large enough that the ice-water stress is equal and opposite to the air-ice stress. In the ocean, the ice-water stress is balanced by the Coriolis force. Because the downstream ocean momentum balance is the Ekman balance, a strong shoreward transport of water develops. In the ice equation, a small remainder of the air-ice stress is balanced by the Coriolis stress, driving a cross stream transport of ice. The sea surface tilt term is comparable to the stresses and it is nonzero across the domain because the geostrophic velocity (calculated from equation 3.59) is always greater than zero.

The momentum balances lead to simple relations between the variables. The ice-water stress is significant in the momentum balance and it is simplified to make it more tractable for developing analytical relationships. The ice water stress is

$$
\begin{aligned}
\vec{\tau_{wi}} &= C_{wi}\rho_i \left| \vec{u_i} - \vec{u_w} \right| \left(\vec{u_w} - \vec{u_i} \right) \\
&= C_{wi}\rho_i \sqrt{(u_w - u_i)^2 + (v_w - v_i)^2} \left(\vec{u_w} - \vec{u_i} \right)
\end{aligned}
$$

However, because $(u_w - u_i) \gg (v_w - v_i)$ (see figures 3-18 and 3-21), the ice water stress can be approximated as

$$
\vec{\tau_{wi}} \approx C_{wi}\rho_i \left| u_w - u_i \right| \left(\vec{u_w} - \vec{u_i} \right)
$$

The x and y components of the ice-water stress, respectively, are

$$
\tau_{wi}^x \approx C_{wi}\rho_i \left| u_w - u_i \right| (u_w - u_i) \tag{3.61}
$$

$$
\tau_{wi}^y \approx C_{wi}\rho_i \left| u_w - u_i \right| (v_w - v_i) \tag{3.62}
$$

162
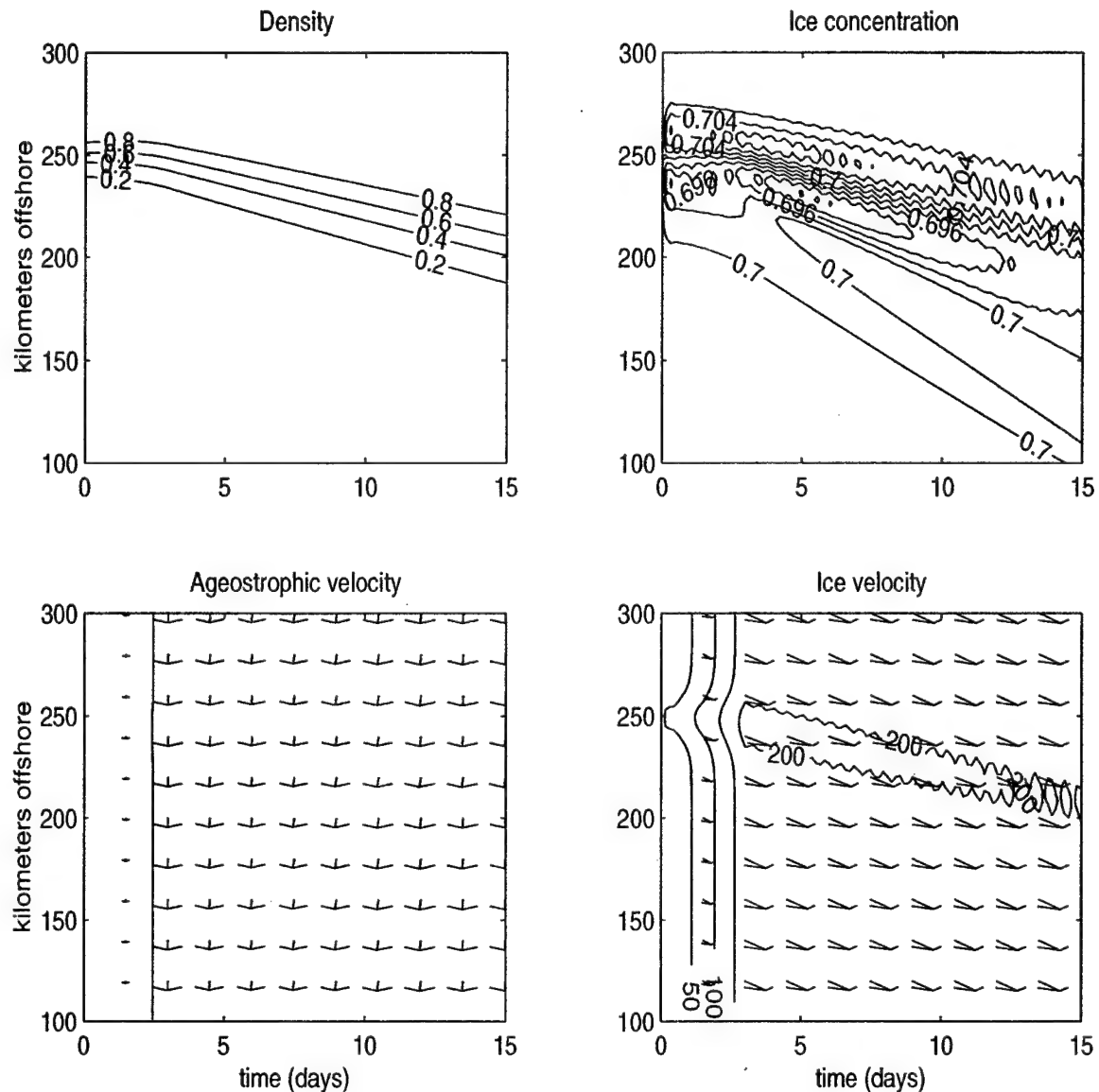
Figure 3-18: The results from the winter experiment with 6 m/s wind and an underlying current. (upper left: a) the density anomaly, versus time. (upper right: b) the ice concentration, versus time. (lower left: c) the water velocity (arrows) with the absolute speed contoured, versus time. Arrows pointing right indicate movement in the $+x$ direction. Arrows pointing up indicated movement in the $+y$ direction. The arrows are exaggerated by approximately a factor of 10 in the cross stream direction. Contours are labeled in mm/second. (lower right: d) the ice velocity (arrows) with the absolute speed contoured. Arrows and contours as in the plot of the ageostrophic velocity.

163
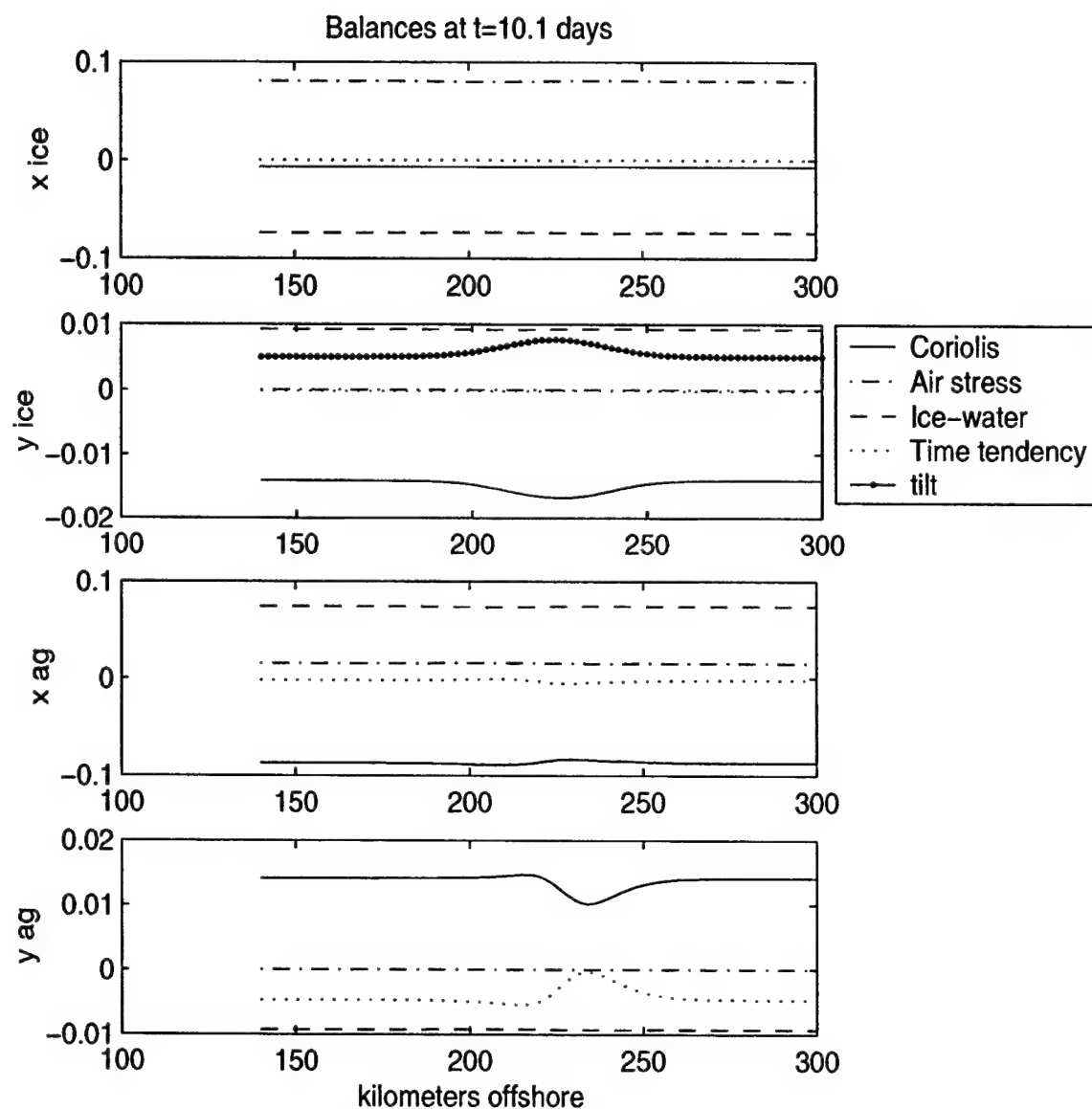
Figure 3-19: The winter momentum and density balances after ten days for the winter experiment with 6 m/s wind and an underlying current. Line types as in figure 3-14. Units on the vertical axis are kg m s^{-2}.
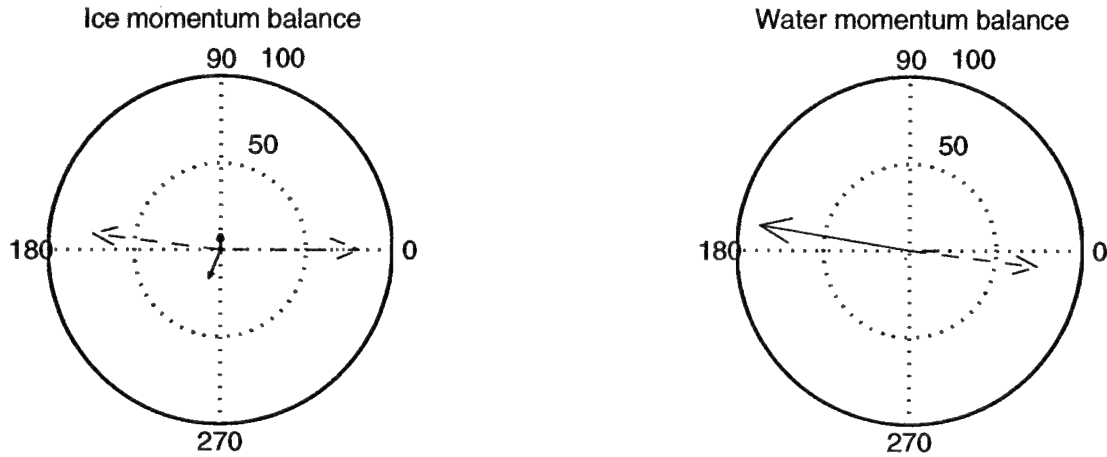
Figure 3-20: The directional winter momentum balances at the same time as figure 3-19. Line types as in figure 3-14. The magnitude of the arrows is scaled by 1000.

In the downstream direction, the ice and water balances[10], respectively, are[11]

$$0 = \quad A\tau_{ai}^x \quad +A\tau_{wi}^x \tag{3.63}$$

$$0 = \quad \rho_o \delta f_0 v_{ag} \quad -A\tau_{wi}^x \tag{3.64}$$

By substituting the simplified expression for the ice-water stress (equation 3.61) into equation 3.63, an expression for the difference between the ageostrophic velocity in the ocean and the water as a function of τ_{ai}^x and the background geostrophic velocity is found.

$$u_{ai} - u_{ag} = \sqrt{\frac{\tau_{ai}^x}{\rho_i C_{wi}}} \tag{3.65}$$

---

[10]This analysis solves for the velocities of the water and ice. The Coriolis force in the ice momentum equation (3.63) is neglected because the primary balance is between the air-ice and the ice-water stresses. Similarly, because the ocean is mostly covered with ice, the air-water stress is small and it is neglected in the ocean momentum equation under the ice (3.64). These approximations do not represent the entire picture, but the simplifications allow for some simple predictions about the ice and water velocities.

[11]Summing 3.63 and 3.64 the basic dynamics are clear: the stress from the wind is balanced by the Coriolis force, driving a cross-stream transport of water.

Adding 3.63 to 3.64, an expression for v_{ag} as a function of τ_{ai}^x is found.

$$v_{ag} = -\frac{\tau_{ai}^x}{f_0 \rho_o \delta} A \tag{3.66}$$

In the cross stream direction, the balances are[12]

$$0 = \quad -m f_0 u_i + m f_0 u_g \quad +A\tau_{wi}^y \tag{3.67}$$

$$0 = \qquad -\rho_o \delta f_0 u_{ag} \qquad -A\tau_{wi}^y \tag{3.68}$$

Combining the first two terms in 3.67, it becomes

$$0 = -m f_0 u_{ai} + A\tau_{wi}^y \tag{3.69}$$

Adding 3.68 and 3.69, the relationship between the downstream ice and water velocities is found

$$u_{ai} = -\frac{\rho_o \delta}{m} u_{ag} \tag{3.70}$$

This indicates that the magnitude of the ageostrophic mass transports in the downstream direction are equal while the directions are opposite. In general, the ice mass is much less than the water mass so the magnitude of the ice velocity is much larger. In the limit where the masses are equal, the velocities are equal and opposite. Because the velocities are always opposite, the ice-water stress in the downstream direction is always nonzero. Equation 3.70 can be substituted into 3.65 and the following expressions for u_{ai} and u_{ag} are found.

$$u_{ag} \quad = \quad -\frac{m}{m + \rho_o \delta} \sqrt{\frac{\tau_{ai}^x}{C_{wi}\rho_i}} \tag{3.71}$$

$$u_{ai} \quad = \quad \frac{\rho_o \delta}{m + \rho_o \delta} \sqrt{\frac{\tau_{ai}^x}{C_{wi}\rho_i}} \tag{3.72}$$

---

[12]Summing equations 3.67 and 3.68 the basic dynamics are clear. The tilt term balances the Coriolis force, driving the along stream transport of water and ice.

In the limit where the mass of ice and water are equal, i.e. when $\rho_o \delta = m$, the ageostrophic velocities reduce to $u_{ai} = -u_{ag} = \frac{1}{2}\sqrt{\frac{\tau_{ai}^x}{C_{wi}\rho_i}}$. Not surprisingly, the ageostrophic ice and ocean velocity are of a similar form to the scale selected for it, u^*. It is interesting to note that the difference between the velocities in the down-wind direction is independent of the relative masses of the two layers and is only dependent on the air-ice stress.

$$u_{ag} - u_{ai} = \sqrt{\frac{\tau_{ai}^x}{C_{wi}\rho_i}}$$

This implies that τ_{wi}^x is independent of the relative masses in the two layers, as well.

Equation 3.69 is solved for v_{ai} by expanding the ice-water stress term with 3.62.

$$v_{ai} = v_{ag} - \frac{Df_0}{C_{wi}} \frac{u_{ai}}{|u_{ai} - u_{ag}|} \tag{3.73}$$

The cross-wind ageostrophic velocity in the ice is in the same direction as in the ocean. The difference between the velocities in the cross wind direction is

$$v_{ag} - v_{ai} = -\frac{Df_0}{C_{wi}} \frac{u_{ai}}{|u_{ai} - u_{ag}|}$$

and because u_{ai} depends on the relative masses in the two levels, τ_{wi}^y depends both on the relative masses and the air-ice stress.

Figure 3-21 shows the predicted velocity components versus the model results. In general, there is reasonable agreement. The model data were low pass filtered to remove inertial oscillations. The fit for u_{ag} is not as good as the other variables because the speeds are small and the momentum balance used in this approximation is a poorer approximation. The predicted values for v_i are consistently smaller than the model results, suggesting that the Coriolis term in equation 3.63, even though it is small, may be significant to the dynamics.

Cross stream variations in ice concentration are created by divergence in cross
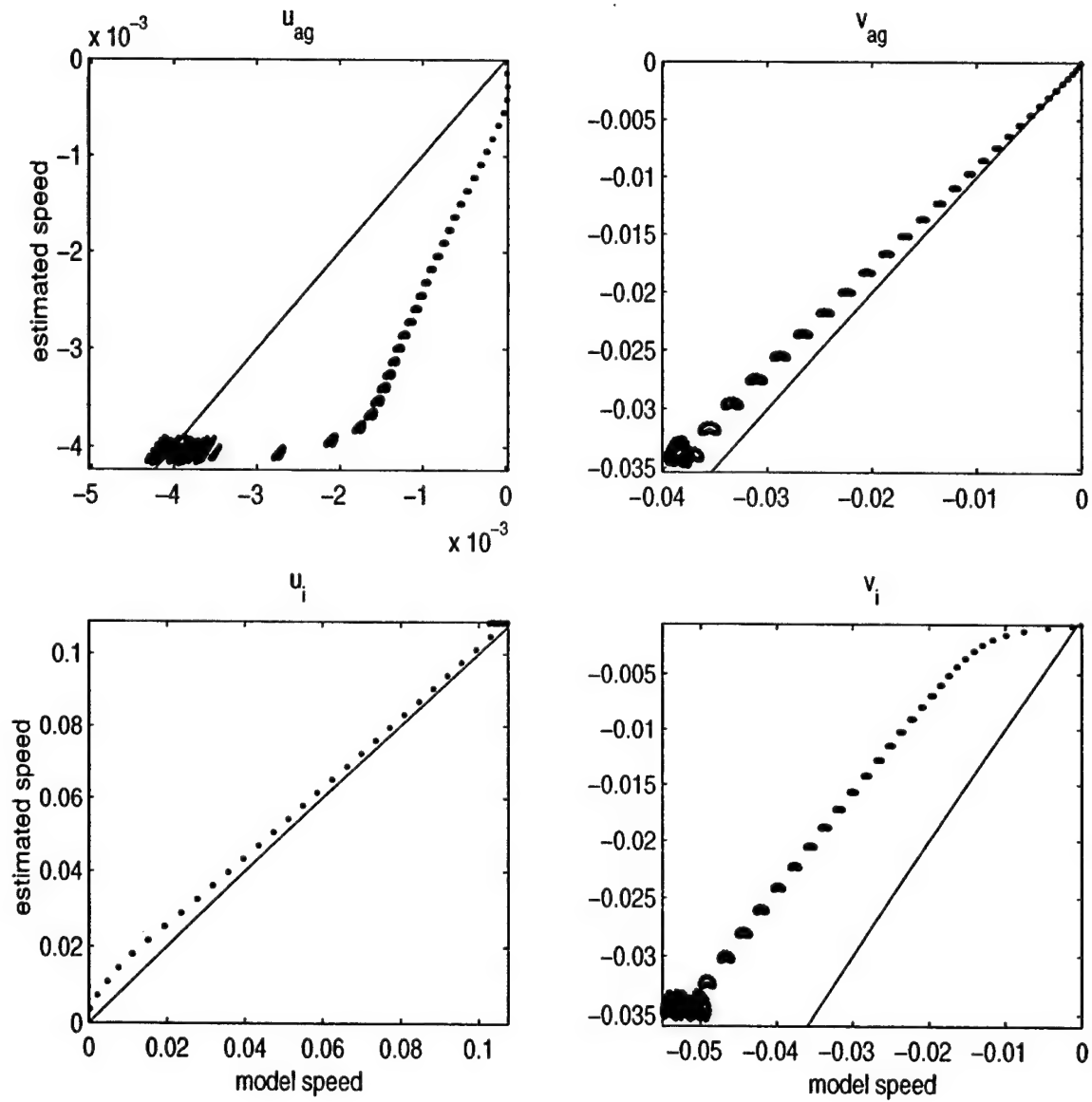
Figure 3-21: The ageostrophic velocities estimated from the momentum balance verses the ageostrophic velocities from the model results. The model velocities were low pass filtered to remove inertial oscillations. Model data are shown as individual points. A line with a slope of 1 is shown in solid. (a) u_{ag} (b) v_{ag} (c) u_i (d) v_i

stream ice transport, or

$$\frac{\partial A}{\partial y} \propto \frac{A}{v_i}\frac{\partial v_i}{\partial y}$$

The cross-stream ice speed, v_i, is the sum of v_{ag} and a term which is a function of the wind speed. The cross stream ageostrophic velocity (3.66) is a function of wind speed and ice concentration. Because A is initially constant across the domain, v_{ag} and v_i are constant as well. Only perturbations introduced by inertial oscillations create a divergence in v_i. Because the inertial oscillations are small, the divergence in cross stream ice transport is small and A does not significantly change from its initial value.

The tilt term reduces the cross stream divergence in ocean transport. v_{ag} is a quadratic function of wind speed and a linear function of ice concentration. So long as there is ocean tilt, the ice concentration variance throughout the domain is small. If there are only small variations in ice concentration, there are only small variations in v_{ag}, reducing the divergence in the cross stream transport of water. For a smaller cross stream transport divergence, the implied vertical velocity is decreased. This is reflected in figure 3-22a where the vertical displacement of an initially flat surface is shown.

Summer   The results from a summer experiment, with a partially ice covered domain, are shown in figure 3-23 and the balances are shown in figure 3-24. Both the front and the ice edge move shoreward over the course of the experiment but the ice edge moves faster because the air-ice drag coefficient is larger than the air-water drag coefficient and the ice mass is smaller than the water mass, resulting in a greater Ekman transport. In the ocean, there is shoreward Ekman transport everywhere, but it is stronger under the ice.

The balances under the ice are the same as in the winter case. In the downstream direction on the ice, the air-ice stress is balanced by the ice-water stress. In the ocean, the ice-water stress is balanced by the Coriolis force, driving a shoreward

169
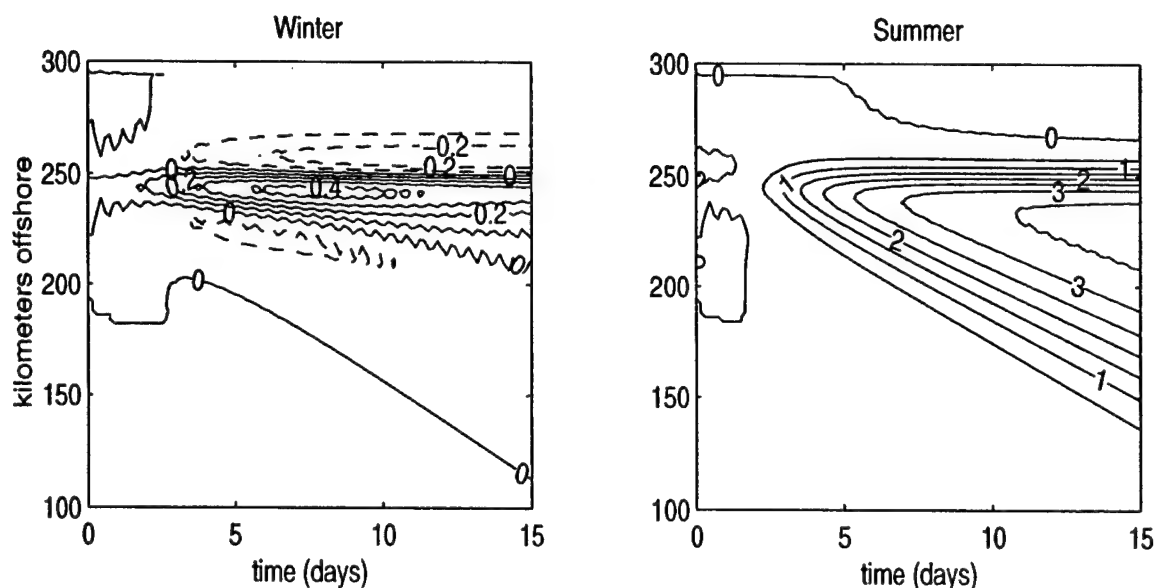
Figure 3-22: The vertical displacement of an originally flat surface at the base of the Ekman layer, calculated from 3.36. Contours labeled in meters.

Ekman transport. In the cross stream momentum equation, the large downstream ice velocity u_i, set by the wind speed, creates a large Coriolis force in the ice. This is balanced by both a cross stream ice-water stress and the sea surface tilt term. The cross stream ice-water stress is balanced by the Coriolis force in the ocean.

Under open water where there is no ice, the downstream balance in the ocean is between the air-water stress and the Coriolis force. Because the air-water drag coefficient is smaller than the water-ice and air-ice drag coefficients, the shoreward transport of water where there is no ice is smaller than where there is ice. This creates a divergence of water transport in the ocean at the ice edge, which drives strong ice-edge upwelling. The deformation of an originally flat surface due to this vertical motion is shown in figure 3-22b. The vertical deformation is similar to the reversed Roed and O'Brien experiment (figure 3-8a).

Parameter variations   In this section, several variations of the parameters are investigated. First, the wind speed is varied and the background geostrophic velocity is calculated from the wind speed. Second, the wind speed is varied while the back-

170
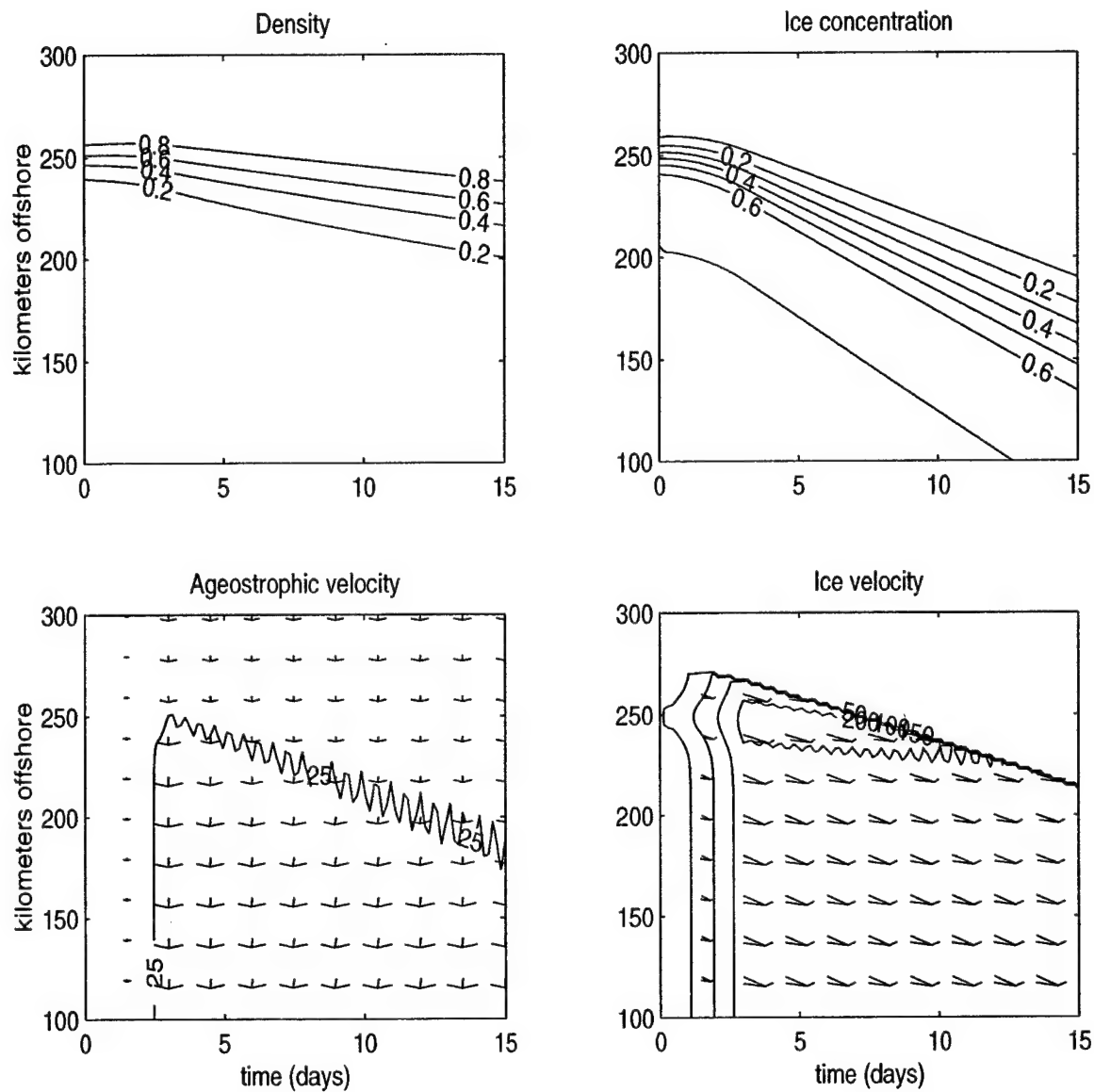
Figure 3-23: The results of the summer experiment with wind. (upper left: a) the density anomaly, versus time. (upper right: b) the ice concentration, versus time. (lower left: c) the water velocity (arrows) with the absolute speed contoured, versus time. (lower right: d) the ice velocity (arrows) with the absolute speed contoured. Arrows and contours as in figure 3-18.

171
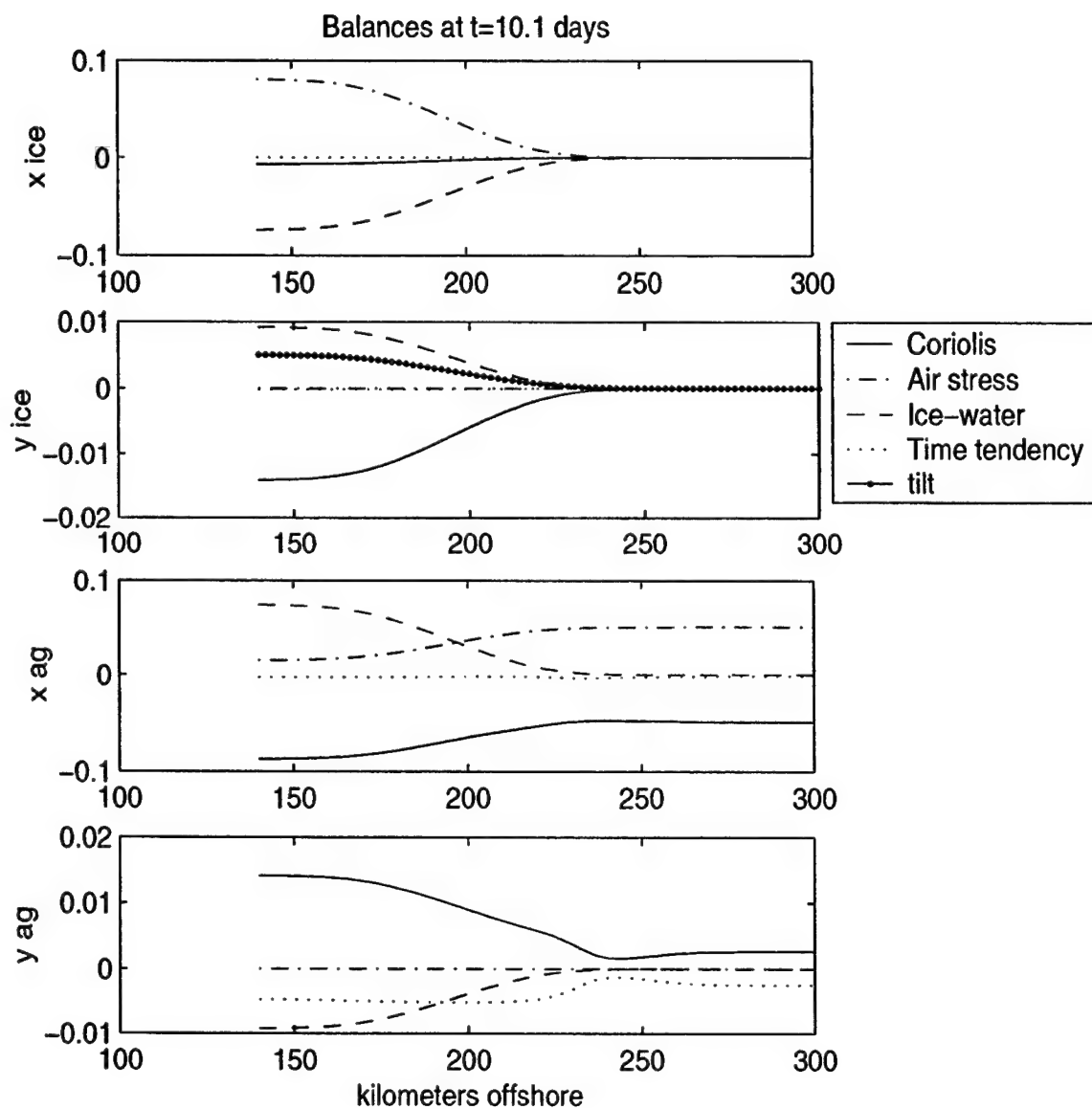
Figure 3-24: The summer momentum and density balances after ten days. Line types as in figure 3-14.

ground geostrophic velocity is held constant, equal to the maximum velocity of the underlying jet. Next, the surface ice concentration is varied while the winds and background geostrophic velocity are held constant. Finally, the importance of the relative ice and water masses is discussed. In all experiments, the model is in a "winter" like configuration with uniform ice coverage.

The momentum balances as a function of wind speed, when u_g is varied with the wind, are shown in figure 3-25. The behavior of the system with 6 m/s winds is typical of both larger and smaller wind speeds. In the downstream direction, the ice has a balance between the air-ice stress and the ice-water stress. In the cross stream direction, the balance is between the Coriolis term, the tilt term and the ice-water stress. In the ocean, the balance is between the ice-water stress and the Coriolis force.

For very light winds, the background geostrophic velocity is approximately equal to the jet velocity and the magnitude of wind driven background is insignificant. In this limit, the air-ice stress is smaller than the difference between the tilt term and the Coriolis term and the balance between the tilt and the Coriolis term dominates the momentum balance. Figure 3-26 shows a directional plot of the momentum balances in the jet, under 1 m/s winds. Compared to the experiments with no wind and with no current (figure 3-20 which has 6 m/s winds), elements of both experiments are present. In the ice, the dominant balance is in the cross stream direction between the sea surface tilt and the Coriolis term, as was true in the no wind experiment. The air-ice stress introduces a downstream component to the momentum balance, which is balanced by the ice-water stress and Coriolis force as is typical for larger winds. In the ocean, the balance between the time tendency and Coriolis force creates a strong inertial oscillation field like the no wind experiment. The ice-water stress is present, creating a small Ekman transport as is seen under stronger winds.

An additional set of experiments is done varying only the wind speed and not the underlying current. The geostrophic background current is defined to be equal to the thermal wind velocity from the underlying current. The momentum balances
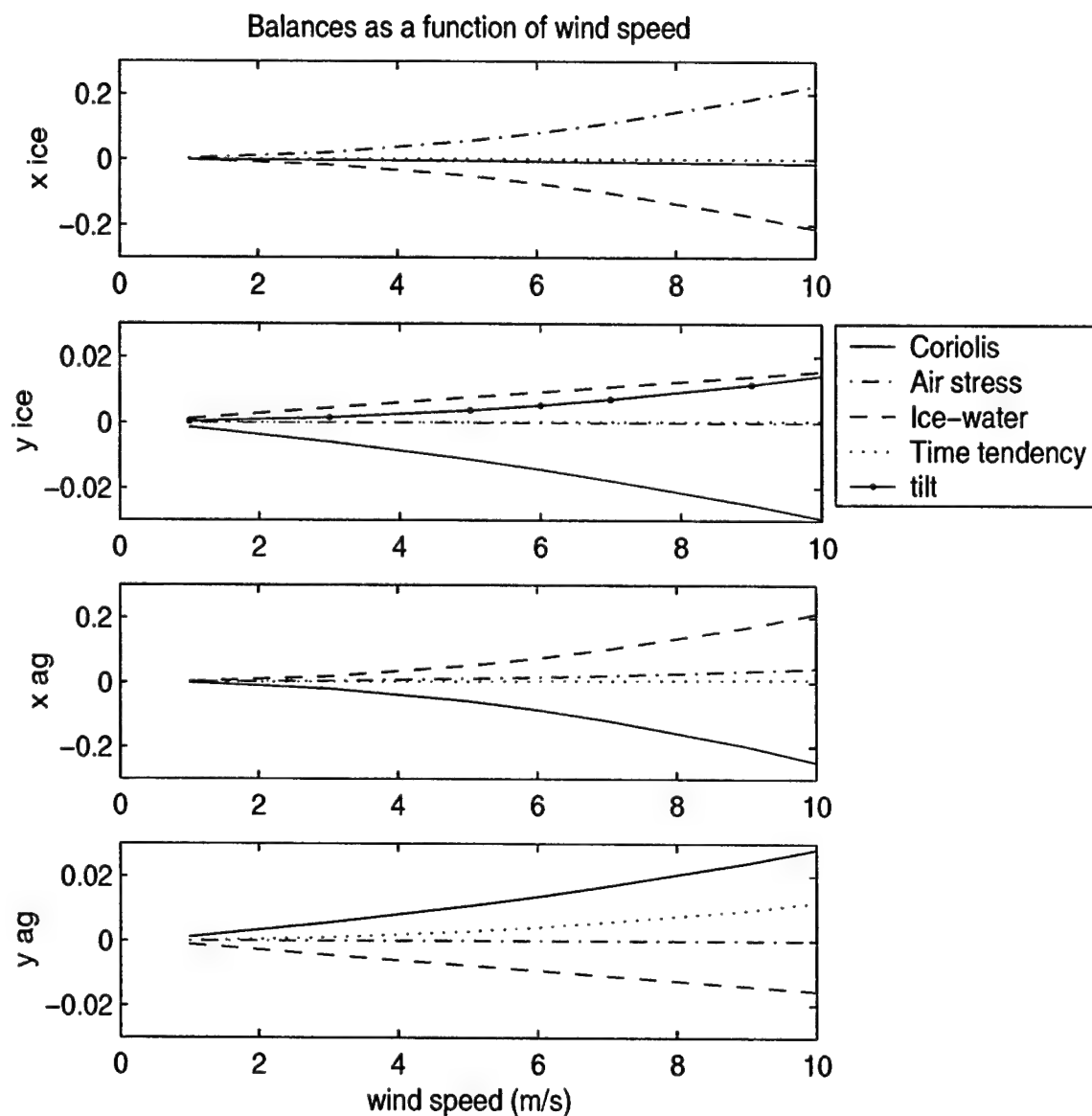
Figure 3-25: The balances as function of wind speed and changing u_g with an initial ice concentration of 0.7. In these experiments, the background geostrophic velocity is a function of the wind speed. The ice momentum balances (a) and (b), the water momentum balances (c) and (d). Momentum balances are averaged across the domain.
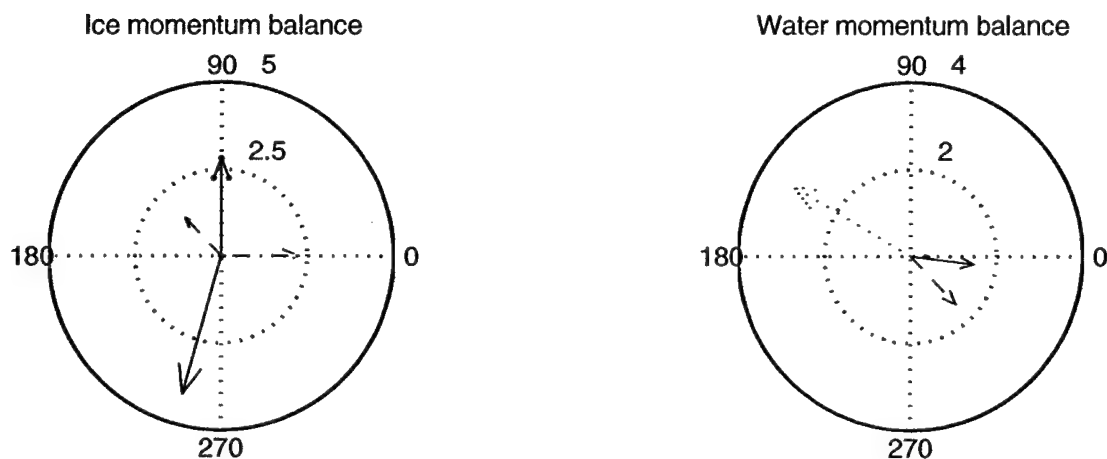
Figure 3-26: The directional winter momentum balances under 1 m/s winds with an underlying geostrophic current. Line types as in figure 3-14. The magnitude of the arrows is scaled by 1000. In the ice the fundamental balance is between the tilt term and the Coriolis force, with the wind stress playing a secondary role.

for these experiments are shown in figure 3-27. In these experiments, the geostrophic background velocity is a constant, set by the density distribution and therefore the tilt term is not effected by varying the wind speed. This reduces the significance of the tilt term and forces the Coriolis term to balance all of the stress. Because the Coriolis force is larger in the absence of a tilt term, the cross stream Ekman transport of both water and ice is enhanced. When the tilt term is negligible, the ice-ocean balance reduces to the wind and ice with no current experiments discussed in section 3.3.

The balances as a function of ice concentration are shown in figure 3-28. The only significant dependence on ice concentration is in the x ageostrophic momentum equation. The stress on the ocean is an average between the air-water stress and the ice-water stress. The average is weighted by the ice concentration, or the percentage of water area exposed to the atmosphere. For low ice concentration, only a small fraction of the grid cell is covered in ice and most of the water is in contact with the atmosphere; the stress is dominated by the air-water stress. At high ice concentrations, the water is almost entirely shielded from the wind and the ice-

175
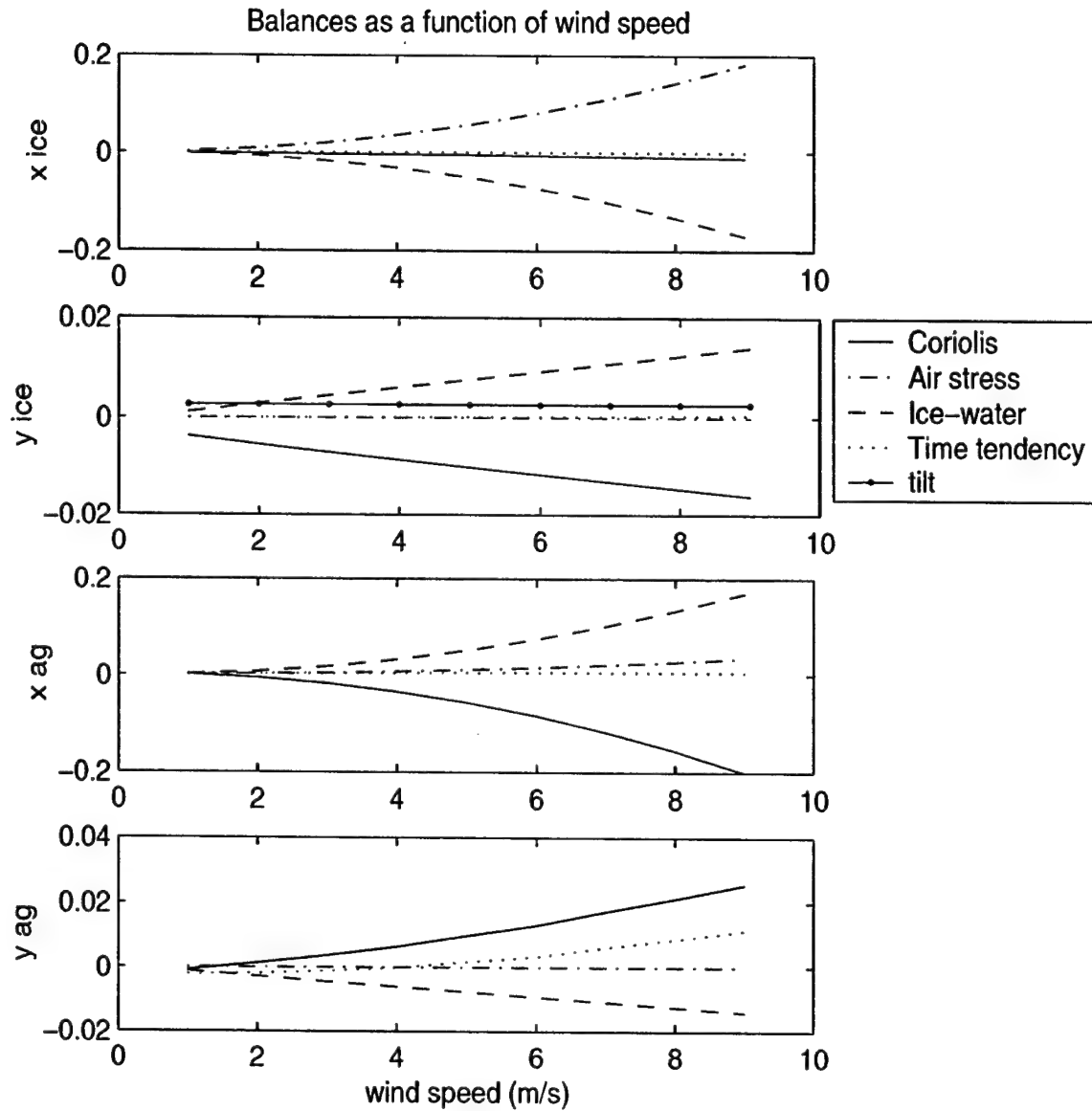
Figure 3-27: The balances as function of wind speed with an initial ice concentration of 0.7 and no variation in the geostrophic current as the wind speed increases. The background geostrophic velocity is independent of wind speed. The ice momentum balances (a) and (b), the water momentum balances (c) and (d). Momentum balances are shown for the $\rho = 0.5$ kg m^{-3} isopycnal which is at the center of the geostrophic jet.
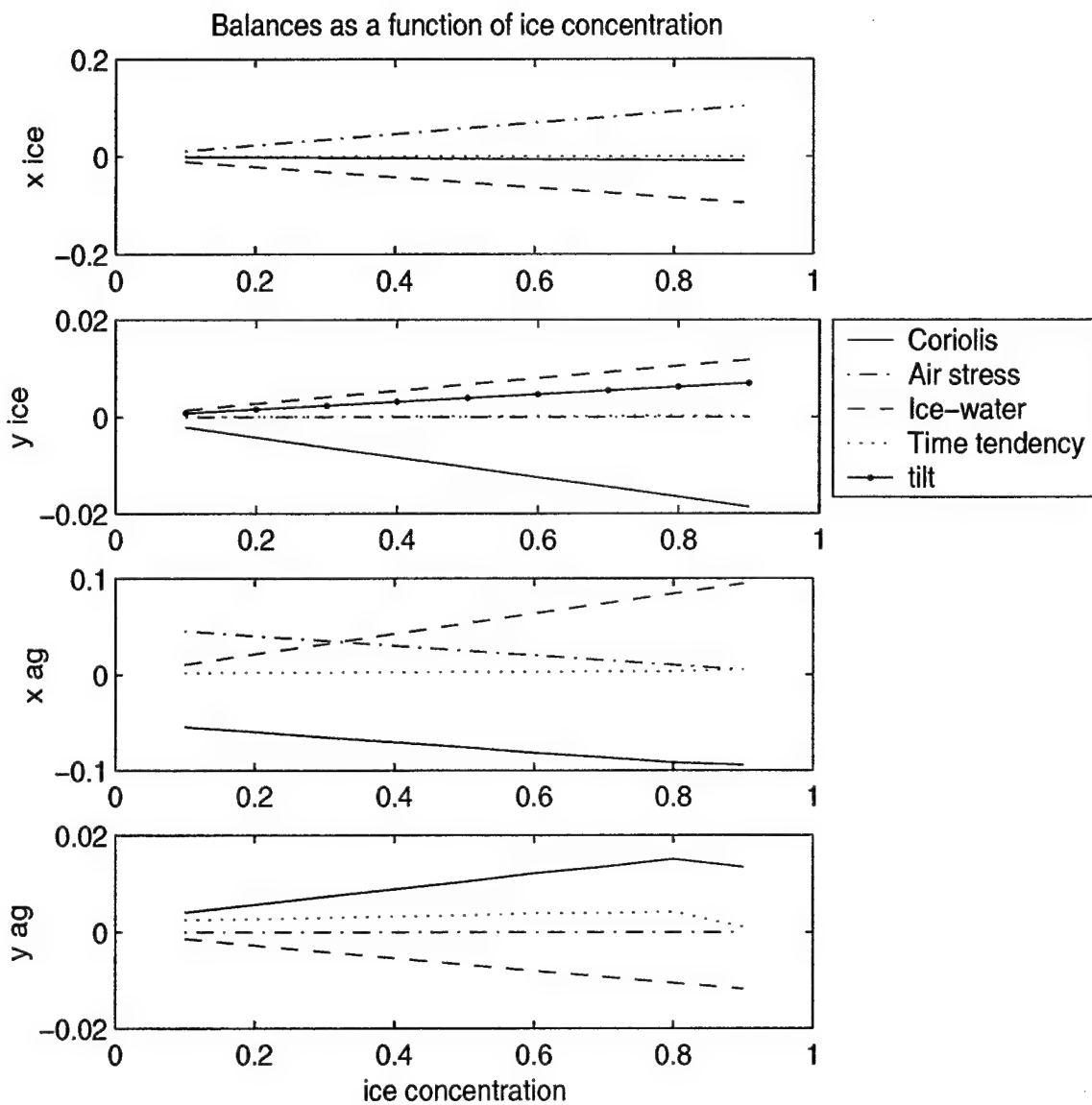
Figure 3-28: The balances as function of ice concentration under 6 m/s winds. The ice momentum balances (a) and (b), the water momentum balances (c) and (d), the ice balance (e) and the density balance (f). Momentum balances are averaged across the domain.

water stress dominates. Because the air-ice and ice-water drag coefficients are larger than the air-water drag coefficient, the balancing Coriolis force is larger for higher ice concentrations.

Finally, a brief discussion of the significance of the relative mass of the ice and water is given. Throughout this chapter, it is assumed that the mass of the ice is much less than the mass of the water. In general, this is a reasonable approximation, but what if it is the other way? What if the mass of the ice is much greater than the mass of the water? Looking at the left hand side of the non-dimensional ice momentum equation (3.21), the ratio $\frac{\delta}{D}$ appears in both stress terms. If the mass of the ice is changed by making it very thick, this ratio becomes very small. The stress terms are scaled by the ratio $\frac{\delta}{D}$ and as that ratio gets small, the stress terms become small. The only term left to balance the Coriolis term is the time tendency, creating inertial waves. Therefore, even with significant winds, the first order response of the ice is inertial waves.

In the discussion of the no-wind results where inertial waves dominate the ageostrophic response, the ice momentum balance early in the experiment is between the time tendency, the Coriolis force, the tilt term and the ice-water stress (figure 3-15) or

$$\frac{\partial u_i}{\partial t} = f_0 v_i - \frac{C_{wi}}{D} |u_i - u_w| (u_i - u_w) \tag{3.74}$$

$$\frac{\partial v_i}{\partial t} = -f_0(u_i - u_g) - \frac{C_{wi}}{D} |u_i - u_w| (v_i - v_w) \tag{3.75}$$

At the very start of the experiment,

$$\begin{aligned}
(u_i - u_w) &\approx u_i - u_g \\
(v_i - v_w) &\approx 0
\end{aligned} \tag{3.76}$$

If 3.76 is used to simplify the momentum equations and the time derivative 3.74 is used to eliminate $\frac{\partial v_i}{\partial t}$, the momentum equations can be consolidated into one equation for u_i. In addition, it is assumed that $\frac{\partial u_g}{\partial t} \approx 0$. Then momentum equations can be

178

written as

$$\frac{\partial^2 U}{\partial t^2} + \frac{C_{wi}}{D}\frac{\partial}{\partial t}\left(|U|\,U\right) + f_0^2 U = 0$$

where

$$U = u_i - u_g$$

This is the equation for a nonlinear damped oscillator and the adjustment time is inversely related to the ice thickness, D.[13] The larger the ice thickness, the longer it takes for the ice to adjust to the forcing that is causing the inertial oscillations.

Once the ice has adjusted to a steady state, if the majority of the mass is in the ice layer instead of in the water layer, the two layer Ekman spiral has a different structure. The downstream velocity of the ice is reduced and the shoreward velocity is increased. In the limit where all of the mass is in the ice, the ice transport is shoreward with no along-stream component at all. At the other extreme, in the limit where all of mass is in the ocean layer and the ice has no mass, the ice velocity is completely down wind and the water transport is completely shoreward. The ice, through the ice-water stress, relays the wind stress to the ocean.

3.6 Conclusions

In this chapter, the interactions between ice, water and an underlying geostrophic ocean current are examined. In the limit where the geostrophic current is negligible, the tilt term in the ice momentum equation disappears. The momentum balance in the ice is between the air-ice stress, the ice-water stress and the Coriolis force. Ice is carried both in the direction of the wind and to the right of the wind, through Ekman transport. In the ocean, the momentum balance is between the ice-water stress and the Coriolis force, driving an Ekman transport to the right of the wind.

When there is just a geostrophic current and ice, with no wind, the balance in the

---

[13] With this form of a nonlinear oscillator, it is not obvious what the damping coefficient is, but it probably scales as $\frac{U}{D}$.

179

ice is between the tilt term and the Coriolis force, causing the ice to be advected in the same direction as the current. Because the ice is carried along with the current, there is no stress between the ice and the water and there is nothing driving an ageostrophic response in the ocean. All that is observed in the ocean are small inertial oscillations, forced by an imbalance between the tilt term and the Coriolis force.

When all three components of the system are allowed to interact, the behavior of the system is determined by the relative strengths of the air-ice stress and the tilt term. If there is only a small underlying current and strong winds, the tilt term is insignificant and the system behaves as if there is no current. If the underlying current is significant, such as the strong barotropic western boundary current observed in the Greenland gyre, the tilt term remains significant even for substantial winds and there is a three way momentum balance. When there is a strong tilt term, the Coriolis force is smaller, causing a smaller Ekman transport in the ocean and ice.

When the mass of the ice is much less than the mass of the water (the usual case in the polar oceans), both the wind and the underlying currents drive downstream transport in the ice. To first order the ice is simply carried along by the ambient currents and winds. This study did not examine the response of the ice if the wind stress and currents are not in the same direction, but based on the scaling, it is expected that the ratio of the wind stress to the tilt term will determine if the ice follows the wind, the current, or some intermediate path.

The results can be understood by examining the momentum balance of the entire ice-ocean system. Equation 3.11 is the total ice momentum equation. It is multiplied by m, the ice mass, to give the ice mass flux equation

$$m\frac{D\vec{u_i}}{Dt} = -f_0 m \hat{k} \times (\vec{u_i} - \vec{u_g}) + A\vec{\tau_{ai}} + A\vec{\tau_{wi}} \tag{3.77}$$

The ageostrophic ocean momentum equation is multiplied by the mass of water in

the Ekman layer, $\rho_o\delta$, to give the ageostrophic water mass flux equation

$$\rho_o\delta\frac{D\vec{u_w}}{Dt} = -f_0\rho_o\delta\hat{k} \times \vec{u_{ag}} + (1-A)\vec{\tau_{aw}} - A\vec{\tau_{wi}} \tag{3.78}$$

Adding equations 3.77 and 3.78 together, the momentum equation for the entire ice-water system is found:

$$\frac{D}{Dt}\left(\vec{U_I} + \vec{U_w}\right) = -f_0\hat{k} \times \left(\vec{U_I} + \vec{U_W} - \vec{U_G}\right) + \vec{\tau_S} \tag{3.79}$$

where the total transport of ice is defined as $\vec{U_I} = m\vec{u_i}$, the total transport of water is defined as $\vec{U_W} = \rho_o\delta\vec{u_w}$ and the total geostrophic transport of ice and water is $U_G = (m + \rho_o\delta)\vec{u_g}$. The total surface stress is $\vec{\tau_S} = A\vec{\tau_{ai}} + (1-A)\vec{\tau_{aw}}$.

If the system is in steady state, equation 3.79 is

$$0 = -f_0\hat{k} \times \left(\vec{U_I} + \vec{U_W} - \vec{U_G}\right) + \vec{\tau_S} \tag{3.80}$$

When there is no surface stress and there is an underlying current, the transports of water and ice must be balanced by the tilt of the sea surface created by the underlying current and the ageostrophic transport is negligible.

$$\vec{U_I} + \vec{U_W} - \vec{U_G} = 0$$

When there is a surface stress and no underlying current, there is Ekman balance in the ice-water system

$$0 = -f_0\hat{k} \times \left(\vec{U_I} + \vec{U_W}\right) + \vec{\tau_S} \tag{3.81}$$

and the water transport only consists of ageostrophic transport. When there is both a current and surface stress, the relative magnitude of the tilt term and the surface

stress term determines the response of the system. In other words when the ratio

$$\frac{\vec{\tau_S}}{f_0 U_G} = \frac{A\vec{\tau_{ai}} + (1 - A)\vec{\tau_{aw}}}{f_0(m + \rho_o\delta)\vec{u_g}}$$

is greater than one, the surface stress dominates and the majority of the transport is ageostrophic and perpendicular to the wind. When the ratio is less than one the tilt term dominates the equation and the majority of the transport is geostrophic and parallel to the current. If the geostrophic velocity is scaled with the wind speed, this ratio is asymptotic to a value is a little less than one in the region of the East Greenland Current.

For these experiments, only cases where the wind was parallel to the current were examined and these two effects are perpendicular. If the wind was at a right angle to the current, however, the direction of the ageostrophic and geostrophic currents would be either parallel or anti-parallel but with the simplified dynamics of this model, the general behavior of the ice-ocean system is expected to be similar.

Chapter 4

Summary and discussion

This thesis explores the impact of surface stress and background currents on the shelf circulation using numerical models. In chapter 2, the impacts of wind and barotropic inflows on a shelf current are examined using a full primitive equation model. In chapter 3 the interactions between sea ice, underlying currents and winds are examined using a simplified one dimensional model. In all cases, the winds and barotropic inflows modeled in this thesis are so-called "downwelling-favorable", or have transports in the same direction as the density driven current. In this chapter, an overall summary and discussion of the major results are given and a variety of proposals for future work are suggested.

A wind blowing parallel to the shore over an infinite channel with homogeneous density water causes a shoreward Ekman transport in the surface Ekman layer. Mass in the cross shelf direction is balanced by an offshore transport in the bottom Ekman layer. The cross shelf Ekman transport creates a pressure gradient such that a barotropic current develops through geostrophy, in the same direction as the wind. The channel model used in this study is finite and any barotropic response to the wind must be imposed as a boundary condition. An expression relating the wind speed to the barotropic speed in an infinitely long channel is derived and tested in a periodic channel model. The periodic channel results agree well with the infinite

channel predictions. While the barotropic current predicted by the prescribed wind stress is not usually used in the experiments discussed, this relation is used to choose the values of the bottom drag coefficient and the maximum allowable vertical mixing in such a way that if a wind stress appropriate for the East Greenland Current region is applied, a barotropic current is generated similar to the observed one.

A numerical model, similar to the one used by Chapman (2000), is used to investigate the response of a buoyant shelf current to so-called "downwelling favorable" winds and to barotropic inflows. Downwelling favorable winds and barotropic inflows have transports in the same direction as the buoyant inflow and downwelling along the shoreward wall. In the case of the wind, the downwelling is driven by surface shoreward Ekman transport hitting the coast. In the case of the barotropic inflow, the downwelling is driven by bottom Ekman transport away from the coast. For a barotropic inflow, the cross shelf bottom Ekman mass transport is primarily balanced by a transport in the interior; for wind, the cross shelf surface Ekman mass transport is balanced by transport in the bottom Ekman layer, driven by an along shelf barotropic transport. While the model tries to spin up a barotropic current in the direction of the wind, it is not able to do so since the inflow boundary is prescribed. To conserve mass in the along shelf direction, a narrow jet with up-wind transport develops at the offshore wall. Unfortunately this artificial jet has a distinct influence on the front.

The impact of the wind and barotropic inflow on the shelf front is broken into two sets of responses: i) the development of mixed layers due to enhanced Ekman transport; ii) changes in the position of the front due either to interior return flow from the bottom Ekman layer.

The wind creates a homogeneous surface stress on the channel, directed downstream. At the surface of the ocean, this stress produces a shoreward Ekman transport. In the coastal jet with an associated density front, the shoreward Ekman transport carries heavy interior water over lighter shelf water. Convective adjust-

184

ment removes the static instability and creates a surface mixed layer. The barotropic inflow generates a bottom stress directed upstream. The bottom stress produces an offshore, bottom Ekman transport. This moves light coastal water under heavier interior water and convective adjustment corrects the instability, thickening the bottom mixed layer. In steady state, the thickness of both mixed layers is set by the balance between density carried across the front by Ekman transport and the advection of density downstream by the along shelf currents. A scaling argument to predict the thicknesses of both mixed layers is developed and the analytical prediction agrees well with the model results.

Yankovsky and Chapman (1997) predict the trapping depth of a front based on the density difference across the front and the transport of the front. They define the transport of the front as its transport at the inflow boundary. Here it is observed that a barotropic current shifts the front shoreward and wind stress shifts the front slightly offshore. It is hypothesized that the movement of the front when there is a barotropic inflow is due to the cross shelf interior return flow from the bottom Ekman transport. When there is a bottom Ekman transport driven by a barotropic current, there is a shoreward interior return flow pushing the front into shallower water. When there is a wind driven surface Ekman transport, the model attempts to generated an along shelf barotropic current but because the inflow boundary is prescribed, a jet with up-wind transport develops at the offshore wall. This jet is formed by the convergence of water at the offshore wall and as it draws water in, the front is drawn into deeper water.

This study measures the location of the front as the wind stress and barotropic inflow parameter space is explored. In general, the magnitude of the barotropic inflow controls the location of the front with the wind stress playing a more subtle role. It is possible that this occurs because the wind stress is a spatially homogeneous forcing while the barotropic inflow, because of its adjustment to a sloping bottom, is stronger in deeper water than it is in shallower water, intensifying its impact near the front.

185

Woodgate et al. (1999) observe a strong barotropic transport along the East Greenland Current in the winter, which they attribute to the strong winter winds. They also observe that the core of the East Greenland Current shifts shoreward in the winter. These observations are consistent with this study: in the winter the increased wind stress generates a large barotropic current and the barotropic current shifts the front shoreward. Their observations do not contain sufficient resolution to compare them in detail with the results discussed here.

The interactions between sea ice, wind, and underlying geostrophic currents are examined using a one dimensional ice-ocean coupled model. Again, the wind and currents are directed in the "downwelling favorable" direction. It is found that the forcing inputs produce orthogonal responses in the system. If there is a geostrophic current and no wind, the ice is transported downstream, along the current. If there is wind and and no geostrophic current, the ice/water system is transported shoreward by Ekman transport. In addition, the ice has a downstream transport and the water has an upstream transport.

In the absence of wind, the momentum balance in the ice is between the Coriolis force and the sea surface tilt which results in ice advected along with the current, at nearly the same speed. In addition, there are ubiquitous inertial oscillations which are generated as the ice adjusts to changes in the geostrophic velocity of the underlying current.

When there is wind, the total ice and water mass transport is perpendicular to the wind stress, as expected from Ekman layer theory. However, there is a down-wind transport of ice which is balanced by an equal up-wind transport of water. Since the ice mass is much less than the water mass, the oceanic up-wind velocities are small while the down-wind ice velocities are large.

The wind drives a shoreward Ekman transport in both the ice and water. If there is an ice edge, the Ekman transport of water is divergent at the ice edge. Divergence at the ice edge creates upwelling and ice edge upwelling has been observed in at least

186

one field program.

A brief exploration of parameter space is conducted for an ice-covered ocean under moderate winds. The impacts of wind stress, background inflow velocity, ice concentration and the ratio of ice mass to water mass are examined. The background ocean velocity is important if the tilt term is large in comparison to the surface stress. Then, the majority of the transport is with the current instead of perpendicular to it. For low ice concentrations, the stress on the ice is insignificant and the wind acts directly on the ocean; for high ice concentrations, the wind drives the ice and the ice-water stress transfers the stress to the ocean.

As pointed out in chapter 2, there is a relation between the wind stress and the expected barotropic current in an infinite channel. When there is an ice covered region with steady winds blowing over it, a barotropic current in the direction of the wind will form. The ice in this system is driven downstream by two mechanisms: the sea surface tilt from the current and the stress from the wind. The net transport of ice in the direction of the wind stress will be substantial, hence supporting the observation that ice motion generally follows the wind.

As it can be seen in the scaling section, if the ice-ocean drag coefficient is varied drastically, the ice-ocean system will be strongly coupled (high coefficient) or decoupled (low coefficient). The physics remain unchanged if the ice-ocean drag coefficient is varied moderately from the values used in this study. Since these moderate changes span the range of the drag coefficients estimated from observations, the results presented here are robust and applicable to the real ocean.

The limitations of this work lie in the prescribed boundary conditions and in the lack of a satisfactory ice-ocean coupled model. Papers published during the writing of this thesis have presented ideas and models which may be able to extend this work into more realistic regimes.

Middleton and Cirano (1999) present a solution to the problem of imposing the barotropic current in the wind only experiment. They use a large domain including

a shelf, slope and abyssal ocean. The resolution is enhanced over the shelf and slope region. Wind stress is imposed over a small part of the domain along the shelf and the response of the ocean over the shelf is studied. The barotropic component generated by the wind can be calculated explicitly and the large, low resolution ocean interior returns the circulation, balancing mass.

A similar approach to Middleton and Cirano (1999) could be used to study the Greenland-Iceland-Norwegian Seas. If a transport of light Arctic outflow water is introduced at the northern boundary of the model and an open boundary is permitted at the southern boundary, the system is very similar to the Greenland, Iceland and Norwegian seas. By using such a model, it may be possible to investigate the response of transient forcing, such as storms, as well as the steady response studied here.

Another shortcoming of this work is the limitations of the toy model used to study the ice dynamics. The toy model was developed specifically to study the dynamics of the marginal ice zone and so the model has no ice rheology or thermodynamics and very limited ocean physics. The role of upwelling, for example, would be better studied with a fully coupled model as would problems with high ice concentrations and regions away from the marginal ice zone.

It would be interesting to see if the interactions between the wind, ice and ocean observed persist with a full ice model and a three dimensional ocean model and also if any new dynamic couplings arise. At the start of this work, no such ocean-ice model existed. Recently, Beckman et al. (1999) and Timmerman et al (2000) have presented a fully coupled ice-ocean model where SPEM is coupled to Hibler's (1979) ice model. Their work focused on the Weddell sea gyre, but the coupled model could conceivably be reconfigured for idealized channel problems.

188

Bibliography

[1] K. Aagaard and E.C. Carmack. The role of sea ice and other fresh water in arctic circulation. *Journal of Geophysical Research*, 94:14,485–14,498, October 1989.

[2] K. Aagaard and L.K. Coachman. The east greenland current north of denmark strait. *Arctic*, 21:181–200, 1968.

[3] K. Aagaard and P. Greisman. Toward new mass and heat budgets for the arctic ocean. *Journal of Geophysical Research*, 80:3821–3827, 1975.

[4] J.S. Allen and P.A. Newberger. Downwelling circulation on the oregon continental shelf. part i: Response to idealized forcing. *Journal of Physical Oceanography*, 26:2011–2035, 1996.

[5] J.S Allen, P.A. Newberger, and J. Federiuk. Upwelling circulation on the oregon continental shelf. part i: Response to idealized forcing. *Journal of Physical Oceanography*, 25:1843–1866, 1995.

[6] J.A. Barth, D. Bogucki, S.D. Pierce, and P.M. Korso. Secondary circulation associated with a shelf break front. *Geophysical Research Letters*, 25:2761–2764, 1998.

[7] A. Beckman, H.H. Hellmer, and R. Timmerman. A numerical model of the weddell sea: Large scale circulation and water mass distribution. *Journal of Geophysical Research*, 104:23375–23391, 1999.

[8] J. Blindheim, V. Borovkov, B. Hansen, S-Aa. Malmberg, W.R. Turrell, and S. Osterhus. Upper layer cooling and freshening in the norwegian sea in relation to atmospheric forcing. *Deep Sea Research*, 47:655–680, 2000.

[9] R.H. Bourke, J.L. Newton, R.G. Paqette, and M.D. Tunnicliffe. Circulation and water masses of the east greenland shelf. *Journal of Geophysical Research*, 92:6729–6740, 1987.

[10] B. Boville and P. Gent. The ncar climate systems model, version 1. *Journal of Climate*, 11:1115–1130, June 1998.

[11] R.A. Brown and W.T. Liu. An operational large scale marine planetary boundary layer model. *Journal of Applied Meterology*, 21:261–269, 1982.

[12] F. Bryan. Climate drift in a multi-century integration of the ncar climate systems model. *Journal of Climate*, 11:1455–1471, June 1998.

[13] A. Capotondi and W. Holland. Thermohaline circulation variability in the csm coupled integration and its influence on the north atlantic model climate. *Journal of Climate*, 1997. (Unpublished manuscript).

[14] D. Chapman. Shelf dynamics, class notes. April 1997.

[15] D.C. Chapman. Boundary layer control of buoyant coastal currents and the establishment of a shelfbreak front. *Journal of Physical Oceanography*, 30:2941–2955, 2000.

[16] D.C. Chapman. Sensitivity of a model shelfbreak front to the parameterization of vertical mixing. *Journal of Physical Oceanography*, 2002. accepted.

[17] D.C. Chapman and S.J. Lentz. Trapping of a coastal density front by the bottom boundary layer. *Journal of Physical Oceanography*, 24:1464–1479, July 1994.

[18] G.T. Csanady. The arrested topographic wave. *Journal of Physical Oceanography*, 8:47–62, 1978.

[19] A. da Silva, A. C. Young, and S. Levitus. *Atlas of Surface Marine Data*. NOAA Atlas, 1994.

[20] E.P. Dever. Wind forced cross-shelf circulation on the northern california shelf. *Journal of Physical Oceanography*, 27:1566–1580, 1997.

[21] G. Flato and W. Hibler. On a simple sea-ice dynamics model for climate studies. *Annals of Glaciology*, 14:72–77, 1990.

[22] G. Flato and W. Hibler. Modeling pack ice as a cavitating fluid. *Journal of Physical Oceanography*, 22:626–651, June 1992.

[23] A. Foldvik, K. Aagaard, and T. Torrensen. On the velocity field of the east greenland current. *Deep Sea Research*, 35:1335–1354, October 1988.

[24] D. Fong and W.R. Geyer. The alongshore transport of freshewater in a surface-trapped river plume. *Journal of Physical Oceanography*, 32:957–972, 2002.

[25] G. Gawarkiewicz and D.C. Chapman. A numerical study of dense water formation and transport on a shallow, sloping continental shelf. *Journal of Geophysical Research*, 100:4489–4507, 1995.

[26] G. Gawarkiewicz and A. J. Plueddeman. Topographic control of thermohaline frontal structure in the barents sea polar front on the south flank of spitsbergen bank. *Journal of Geophysical Research*, 100:4509–4524, March 1995.

[27] D.B. Haidvogel, L. Wilkenson, and R. Young. A semi-spectral primitive equation ocean circulation model using vertical sigma and orthogonal curvilinear horizontal coordinates. *Journal of Computational Physics*, 94:151–185, 1991.

[28] S. Hakkinen. Coupled ice-ocean dynamics in the marginal ice zones: Upwelling/downwelling and eddy generation. *Journal of Geophysical Research*, 91:819–832, January 1986.

[29] C.L. Harris, A.J. Plueddemann, and G.G. Gawarkiewicz. Water mass distribution and polar front structure in the western barents sea. *Journal of Geophysical Research*, 103:2905–2917, February 1998.

[30] K. Hedstrom. *User's Manual for an S-Coordinate Primitive Equation Ocean Circulation Model (SCRUM) Version 3.0.* Rutgers University, November 1997.

[31] W. D. Hibler and K. Bryan. A diangnostic ice-ocean model. *Journal of Physical Oceanography*, 17:987–1015, July 1987.

[32] D. M. Holland and et al. Sensitivity study of a dynamic thermodynamic sea ice model. *Journal of Geophysical Research*, 98:2561–2586, February 1993.

[33] R.W. Houghton and M. Visbeck. Upwelling and convergence in the middle atlantic bight shelfbreak front. *Geophysical Research Letters*, 25:2765–2768, 1998.

[34] Sea ice flux in the East Greenland Current. T. martin and p. wadhams. *Deep Sea Research*, 46:1063–1082, 1999.

[35] W. D. Hibler III. A dynamic thermodynamic sea ice model. *Journal of Physical Oceanography*, 9:815–846, July 1979.

[36] M. Ikeda. A three-dimensional coupled ice-ocean model of coastal circulation. *Journal of Geophysical Research*, 93:10731–10748, September 1988.

[37] M. Ikeda. Numerical modeling of ocean circulation and ice cover over the continental shelf. *Journal of Physical Oceanography*, 21:97–117, January 1991.

[38] M. Ikeda, T. Yao, and Q. Yao. Seasonal evolution of sea ice cover and shelf water off labrador simulated in a coupled ice-ocean model. *Journal of Geophysical Research*, 101:16465–16489, July 1996.

[39] A. Jakhelln. Oceanographic investitgations in the east greenland waters in the summers of 1930-1932. *Skr. Svalbard Ishavet*, 6:79 pp., 1936.

[40] J.A. Johannessen and et al. Oceanographic conditions in the marginal ice zone north of svalbard in the early 1979 with an emphasis on mesoscale processes. *Journal of Geophysical Research*, 88:2755–2769, 1983.

[41] J.A. Johannessen, O.M. Johannessen, and et al. Mesoscale eddies in the fram strait marginal ice zone during the 1983 and 1984 marginal ice zone experiments. *Journal of Geophysical Research*, 92:6754–6772, June 1987.

[42] G. Kellner, C. Wamser, and R.A. Brown. An observation of the planetary boundary layer in the marginal ice zone. *Journal of Geophysical Research*, 92:6955–6965, June 1987.

[43] S. Legutke. A numerical investigation of the circulation in the greenland and norwegian seas. *Journal of Physical Oceanography*, 21:118–148, January 1991.

[44] T.O. Manley, L. Hunkins K, and R.D. Muench. Current regimes across the east greenland polar front at 78° 40' north latitude during summer 1984. *Journal of Geophysical Research*, 92:6741–6753, June 1987.

[45] C. Mauritzen. Production of desnse overflow waters feeding the north atlantic across the greenland-scotland ridge. part 1: Evidence for a revised circulation scheme. *Deep Sea Research*, 43:769–806, 1996a.

[46] C. Mauritzen. Production of desnse overflow waters feeding the north atlantic across the greenland-scotland ridge. part 2: An inverse model. *Deep Sea Research*, 43:807–835, 1996b.

[47] G.A. Maykut. Energy exchange over young sea ice in the central arctic. *Journal of Geophysical Research*, 83:3646–3658, 1978.

[48] G.A. Maykut and N. Untersteiner. Some results from a tine dependent, thermodynamic model of sea ice. *Journal of Geophysical Research*, 76:1550–1575, 1971.

[49] M.G. McPhee, G.A. Maykut, and J.H. Morison. Dynamics and thermodynamics of the ice/upper ocean system in the marginal ice zone of the greenland sea. *Journal of Geophysical Research*, 92:7017–7031, June 1987.

[50] G.L. Mellor and T. Yamada. Development of a turbulence closure model for geophysical fluid problems. *Rev. Geophys. Space Phys.*, 20:851–875, 1992.

[51] John F. Middleton and Mauro Cirano. Wind-forced downwelling slope currents: A numerical study. *Journal of Physical Oceanography*, 29:1723–1743, 1999.

[52] J.H. Morison, M.G. McPhee, and G.A. Maykut. Boundary layer, upper ocean, and ice observations in the greenland sea marginal ice zone. *Journal of Geophysical Research*, 92:6987–7011, June 1987.

[53] H. Mossby. Water, salt and heat balance of the north polar sea and of the norwegian sea. *Geophys. Norv.*, 24:289–313, 1962.

[54] R.D. Muench, P.H. LeBlond, and L.E. Hachmeister. On some possible interactions between internal waves and sea ice in the marginal ice zone. *Journal of Geophysical Research*, 88:2819–2826, 1983.

[55] NOAA. Iri/ldeo climate data library. http://ingrid.ldeo.columbia.edu/, May 2000.

[56] J. M. Oberhuber. Simulation of the atlantic circulation with a couple sea ice-mixed layer-isopycnal general circulation model. part i: Model description. *Journal of Physical Oceanography*, 23:808–829, May 1993.

[57] J. M. Oberhuber. Simulation of the atlantic circulation with a couple sea ice-mixed layer-isopycnal general circulation model. part ii: Model experiment. *Journal of Physical Oceanography*, 23:830–845, May 1993.

[58] K.A. Orvik, O.S. Skagseth, and M. Mork. Atlantic inflow to the nordic seas: current structure and volume fluxes from moored current meters, vm-adcp and seasoar-ctd observations, 1995-1999. *Deep Sea Research*, 48:937–957, 2001.

[59] J.E. Overland, B.A. Walter, T.B. Curtin, and P. Turet. Hierarchy and sea ice mechanics: A case study from the beaufort sea. *Journal of Geophysical Research*, 100:4559–4571, 1995.

[60] C.L. Parkinson and W.M. Washington. A large scale numerical model of sea ice. *Journal of Geophysical Research*, 84:311–337, 1979.

[61] R. Pawlowicz. A note on seasonal cycles if temperature and salinity in the upper waters of the greenland sea gyre from historical data. *Journal of Geophysical Research*, 100:4715–4726, March 1995.

[62] R. Pawlowicz and et al. Thermal evolution of the greenland sea gyre in 1988-1989. *Journal of Geophysical Research*, 100:4727–4750, March 1995.

[63] S. Piacsek, R. Allard, and A. Warn-Varnas. Studies of arctic ice cover and upper ocean with a coupled ice-ocean model. *Journal of Geophysical Research*, 96:4631–4650, March 1991.

[64] R.S. Pickart. Bottom boundary layer structure and detatchment in the shelfbreak jet of the middle atlantic bight. *Journal of Physical Oceanography*, 30:2668–2686, 2000.

[65] P.M. Poulain, A. Warn-Varnas, and P.P. Niiler. Near surface circulation of the nordic seas as measured by lagrangian drifters. *Journal of Geophysical Research*, 101:18237–18258, August 1996.

[66] L.P. Roed and J.J. O'Brien. A couple ice-ocean model of upwelling in the marginal ice zones. *Journal of Geophysical Research*, 88:2863–2872, 1983.

[67] P. Schlichtholz and M.N. Houssais. An inverse modeling study in fram strait. part 1: dynamics and circulation. *Deep Sea Research*, 46:1083–1135, 1999.

[68] A. J. Semtner. A numerical study of sea ice and ocean circulation in the arctic. *Journal of Physical Oceanography*, 17:1077–1099, August 1987.

[69] A. S. Thorndike, D. A. Rothrock, G.A. Maykut, and R. Colony. The thickness distribution of sea ice. *Journal of Geophysical Research*, 80:4501–4513, 1975.

[70] R. Timmerman, A. Beckman, and H.H. Hellmer. Sea ice in a coupled ice-ocean model focussed on the weddell sea. http://www.awi-bremerhaven.de/Modelling/BRIOS/seaice.html, July 2000. web site and poster, no peer reviewed papers.

[71] V.T. Timofeyev. Interaction of the arctic ocean waters with the atlantic and pacific waters. *Oceanology*, 3:569–578, 1963. english transl.

[72] P. Wadhams and V.A. Squire. An ice-water vortex at the edge of the east greenland current. *Journal of Geophysical Research*, 88:2770–2780, March 1983.

[73] R. A. Woodgate, E. Fahrbach, and G. Rohardt. Structure and transport of the east greenland current at 75 n from moored current meters. *Journal of Geophysical Research*, 104:18,059–18,072, 1999.

[74] A.E. Yankovsky and D.C. Chapman. A simple theory for the fate of bouyant coastal discharges. *Journal of Physical Oceanography*, 27:1386–1401, July 1997.

[75] J. Zhang and W.D. Hibler. On an efficient numerical method for modelling sea ice dynamics. 1996. (Unpublished manuscript).

Document Library

Distribution List for Technical Report Exchange—August 2002

University of California, San Diego
SIO Library 0175C
9500 Gilman Drive
La Jolla, CA 92093-0175

Hancock Library of Biology & Oceanography
Alan Hancock Laboratory
University of Southern California
University Park
Los Angeles, CA 90089-0371

Gifts & Exchanges
Library
Bedford Institute of Oceanography
P.O. Box 1006
Dartmouth, NS B2Y 4 A2
CANADA

NOAA/EDIS Miami Library Center
4301 Rickenbacker Causeway
Miami, FL 33149

Research Library
U.S. Army Corps of Engineers
Waterways Experiment Station
3909 Halls Ferry Road
Vicksburg, MS 39180-6199

Institute of Geophysics
University of Hawaii
Library Room 252
2525 Correa Road
Honolulu, HI 96822

Marine Resources Information Center
Building E38-320
MIT
Cambridge, MA 02139

Library
Lamont-Doherty Geological Observatory
Columbia University
Palisades, NY 10964

Library
Serials Department
Oregon State University
Corvallis, OR 97331

Pell Marine Science Library
University of Rhode Island
Narragansett Bay Campus
Narragansett, RI 02882

Working Collection
Texas A&M University
Dept. of Oceanography
College Station, TX 77843

Fisheries-Oceanography Library
151 Oceanography Teaching Bldg.
University of Washington
Seattle, WA 98195

Library
R.S.M.A.S.
University of Miami
4600 Rickenbacker Causeway
Miami, FL 33149

Maury Oceanographic Library
Naval Oceanographic Office
Building 1003 South
1002 Balch Blvd.
Stennis Space Center, MS 39522-5001

Library
Institute of Ocean Sciences
P.O. Box 6000
Sidney, B.C. V8L 4B2
CANADA

National Oceanographic Library
Southampton Oceanography Centre
European Way
Southampton SO14 3ZH
UK

The Librarian
CSIRO Marine Laboratories
G.P.O. Box 1538
Hobart, Tasmania
AUSTRALIA 7001

Library
Proudman Oceanographic Laboratory
Bidston Observatory
Birkenhead
Merseyside L43 7 RA
UK

IFREMER
Centre de Brest
Service Documentation—Publications
BP 70 29280 PLOUZANE
FRANCE

50272-101

REPORT DOCUMENTATION PAGE	1. REPORT NO. MIT/WHOI 2003-07	2.	3. Recipient's Accession No.

4. Title and Subtitle

Shelf Currents, Ice and Wind: A Numerical Modeling Study

5. Report Date
February 2003

6.

7. Author(s)   Sarah L. Russell

8. Performing Organization Rept. No.

9. Performing Organization Name and Address

MIT/WHOI Joint Program in Oceanography/Applied Ocean Science & Engineering

10. Project/Task/Work Unit No.
MIT/WHOI 2003-07

11. Contract(C) or Grant(G) No.

(C)

(G)

12. Sponsoring Organization Name and Address

National Science Foundation Graduate Fellowship
Massachusetts Institute of Technology

13. Type of Report & Period Covered
Ph.D. Thesis

14.

15. Supplementary Notes

This thesis should be cited as: Sarah L. Russell, 2003. Shelf Currents, Ice and Wind: A Numerical Modeling Study. Ph.D. Thesis. MIT/WHOI, 2003-07.

16. Abstract (Limit: 200 words)

The effects of sea ice, downwelling favorable winds and barotropic background currents on shelf fronts are examined using numerical models.

The first part of the thesis uses a three dimensional, primitive equation model to examine the behavior of a shelf front under steady, along shelf winds and barotropic currents. The wind stress generates shoreward surface Ekman transport and the barotropic current generates an offshore bottom Ekman transport. In both cases, the Ekman transport causes the creation of mixed layers and a relationship describing the mixed layer thickness is derived relating the cross shelf flux of density to the along shelf flux of density.

The second part of the thesis focuses on the ice-ocean interaction using a simple, two layer, one dimensional toy model. In the presence of a current and the absence of wind, the ice is transported downstream with the current. In the presence of wind and the absence of a current, the net ice-ocean transport is perpendicular to the wind, as is expected for Ekman layer theory. The two layer system acts like a poorly resolved Ekman spiral: the ice has down wind and shoreward transport while the ocean has up wind and shoreward transport.

17. Document Analysis   a. Descriptors

shelf-break
sea-ice
East Greenland current

b. Identifiers/Open-Ended Terms

c. COSATI Field/Group

18. Availability Statement

Approved for publication; distribution unlimited.

19. Security Class (This Report)
UNCLASSIFIED

20. Security Class (This Page)

21. No. of Pages
196

22. Price

(See ANSI-Z39.18)   *See Instructions on Reverse*   OPTIONAL FORM 272 (4-77)
(Formerly NTIS-35)
Department of Commerce